Influence of the ventilation on the transport properties in the healthy and inflamed lung

Frédérique Noël

To cite this version:

Frédérique Noël. Influence of the ventilation on the transport properties in the healthy and inflamed lung. Mathematics [math]. Université Côte d'Azur, 2021. English. NNT : . tel-03156080v1

HAL Id: tel-03156080

https://hal.science/tel-03156080v1

Submitted on 2 Mar 2021 (v1), last revised 11 May 2021 (v2)

UNIVERSITÉ
CÔTE D'AZUR

ÉCOLE DOCTORALE
SCIENCES
FONDAMENTALES
ET APPLIQUÉES

THÈSE DE DOCTORAT

Influence de la ventilation sur les propriétés de transport dans un poumon sain et enflammé

Frédérique NOËL
Laboratoire Jean Alexandre Dieudonné (LJAD)

Présentée en vue de l'obtention
du grade de docteur en Mathématiques
d'Université Côte d'Azur

Dirigée par : Benjamin Mauroy
Soutenue le : 18 Février 2021

Devant le jury, composé de :
Luis Almeida, DR, Sorbonne Université
Valérie Bougault, MC, Université Côte d'Azur
Astrid Decoene, MC, Université Paris Sud
André Galligo, Pr ém., Université Côte d'Azur
Thomas Giletti, MC, Université de Lorraine
Sébastien Martin, Pr, Université de Paris
Benjamin Mauroy, CR, Université Côte d'Azur
Yannick Privat, Pr, Université de Strasbourg

Université Côte d'Azur
École Doctorale de Sciences Fondamentales et Appliquées

Thèse
pour obtenir le titre de docteur de l'Université Côte d'Azur

Discipline : Mathématiques

présentée par
Frédérique Noël

Influence of the ventilation on the transport properties in the healthy and inflamed lung.

Thèse dirigée par Benjamin Mauroy
soutenue le 18 Février 2021

devant le jury composé de

Président du jury :
André Galligo, Professeur émérite, Université Côte d'Azur

Rapporteurs :
Astrid Decoene, Maîtresse de conférence, Université Paris Sud
Thomas Giletti, Maître de conférence, Université de Lorraine

Examinateurs :
Luis Almeida, Directeur de recherche, Sorbonne Université
Valérie Bougault, Maîtresse de conférence, Université Côte d'Azur
Sébastien Martin, Professeur des universités, Université de Paris
Benjamin Mauroy, Chargé de recherche, Université Côte d'Azur
Yannick Privat, Professeur des universités, Université de Strasbourg

Influence de la ventilation sur les propriétés de transport dans un poumon sain et enflammé.

Résumé : La fonction principale du poumon est d'alimenter le sang en oxygène et d'enlever le dioxyde de carbone du sang. Le poumon s'empare de l'oxygène présent dans l'air ambiant dans lequel il rejette le dioxyde de carbone prélevé dans le sang. Cet échange est rendu possible par le processus de ventilation pulmonaire qui fait entrer et sortir périodiquement un volume d'air ambiant. D'un point de vue idéalisé, la ventilation peut être caractérisée par deux paramètres : la vitesse maximale de l'air dans la trachée (l'amplitude) et la fréquence respiratoire (la période). Le but de cette thèse est d'étudier et de modéliser le processus de transport et d'échanges d'oxygène et de dioxyde de carbone dans le poumon. Le transport de gaz est modélisé par des équations de convection-diffusion-réaction dans un poumon idéalisé. Une analyse mathématique du modèle a été réalisée afin de prouver l'existence d'une solution unique ainsi que la périodicité asymptotique en temps. Des simulations numériques ont été réalisées pour étudier un large éventail de configurations physiologiques. Dans le cas d'un poumon humain en bonne santé, les quantités de gaz échangées prédites par notre modèle sont proches de la physiologie. Les énergies visqueuse et élastique dépensées lors de l'inspiration ont ensuite été minimisées en supposant que nos besoins en oxygène peuvent être représentés dans notre modèle par une contrainte du flux d'oxygène échangé avec le sang. Des simulations ont été réalisées pour l'homme, mais aussi pour tous les mammifères en utilisant les lois allométriques. Les prédictions de notre modèle montrent que les paramètres de ventilation chez les mammifères pourraient être optimisés pour dépenser le moins d'énergie possible. Ensuite, nous nous sommes concentrés sur la ventilation pulmonaire d'un humain souffrant d'une infection pulmonaire. La propagation d'une infection bronchique a été modélisée de manière idéalisée et nous avons étudié comment la ventilation est affectée par la réponse du système immunitaire à travers l'inflammation de la paroi bronchique. Nos résultats montrent que la localisation de la zone de transition entre convection et diffusion influence principalement la quantité d'oxygène échangée avec le sang. L'emplacement de cette transition peut être affecté par l'infection et donc altérer l'efficacité de la ventilation et modifier la configuration optimale. Enfin, pour mieux comprendre l'efficacité d'un traitement médicamenteux délivré sous forme d'aérosol, nous avons modélisé le dépôt de particules d'aérosol dans la première bifurcation des bronches du poumon humain. Notre modèle prend en compte l'évolution du rayon des particules due à l'échange de vapeur d'eau et l'évolution de la température des particules due au changement du milieu environnant. Nos résultats montrent que la modélisation de ces paramètres est importante pour représenter plus précisément le dépôt des particules sur les parois des bronches. Ces travaux permettent de mieux comprendre comment le processus de ventilation pulmonaire est ajusté et comment il est affecté par les pathologies pulmonaires. De plus, il souligne comment la ventilation peut être utilisée efficacement pour administrer des médicaments dans le corps humain.

Mots clés : ventilation pulmonaire, transport de gaz, infections pulmonaires, aérosol, modélisation mathématiques, modélisation computationnelle.

Influence of the ventilation on the transport properties in the healthy and inflamed lung.

Abstract: The main function of the lung is to supply the blood with oxygen and to drain the carbon dioxide from it. The lung captures the oxygen present in the ambient air where it rejects the carbon dioxide taken from the blood. This exchange results from the process of the lung's ventilation that repeatedly makes a volume of ambient air enter and leave the lung. In an idealized view, the ventilation can be characterized by two parameters: the maximum air velocity in the trachea (the amplitude) and the breathing frequency (the period). The goal of this thesis is to study and model the process of oxygen and carbon dioxide transport and exchanges in the lung. Gas transport is modeled by convection-diffusion-reaction equations in an idealized lung. A mathematical analysis of the model has been performed to prove the existence of a unique solution along with an asymptotic periodicity in time. Numerical simulations were performed to study a wide range of physiological configurations. In the healthy human case, the amounts of gas exchanged predicted by our model are close to physiology. The viscous and elastic energies spent during inspiration were then minimized assuming that our body needs in oxygen can be represented in our model by a constraint on the oxygen flow exchanged with the blood. Simulations were carried out for humans but also for any mammals using allometric scaling laws. The predictions of our model show that the ventilation parameters in mammals might be optimized to cost as little energy as possible. Then, we focused on the lung's ventilation of a human subject suffering from a pulmonary infection. The spread of a bronchial infection has been modeled in an idealized way and we studied how the ventilation is affected by the response of the immune system through bronchi wall inflammation. Our results show that the location of the transition zone between convection and diffusion mainly influence the quantity of oxygen exchanged with the blood. The location of this transition can be affected by the infection and hence alter the efficiency of the ventilation and modify its optimal configuration. Finally, to better understand the efficiency of a drug treatment delivered by aerosol, we modeled the deposit of aerosol particles in the first bifurcation of the bronchi of the human lung. Our model takes into account the evolution of the radius of the particles due to the exchange of water vapor and the evolution of the temperature of the particles due to the change of the surrounding environment. Our results show that the modeling of these parameters is important to represent more accurately the deposit of the particles on the walls of the bronchi. This work allows to better understand how the process of lung's ventilation is adjusted and how it is affected by lung's pathologies. Moreover, it highlights how ventilation can be used efficiently as a way to deliver drugs in the body.

Keywords: lung's ventilation, gas transport, pulmonary infections, aerosol therapy, mathematical modeling, computational modeling.

Remerciements

Je souhaite tout d'abord remercier mon directeur de thèse, Benjamin. Merci de m'avoir accordé ta confiance en me proposant ce sujet de thèse et de m'avoir si bien accompagné durant ces trois ans. Merci pour ta bienveillance, pour ta gentillesse et pour ta disponibilité. J'ai beaucoup appris à tes côtés et cela a été un vrai plaisir de travailler avec toi durant toute cette période.

Je tiens également à remercier André, pour avoir été disponible, pour nos discussions intéressantes sur les poumons ainsi que pour toutes tes questions pertinentes qui m'ont permis de progresser.

J'aimerais remercier Astrid Decoene et Thomas Giletti pour avoir accepté de rapporter ma thèse. Merci aussi à Luis Almeida, Valérie Bougault, André Galligo, Sébastien Martin et Yannick Privat d'avoir accepté de faire partie de mon jury.

Au cours de ma thèse, j'ai pu participer à un projet proposé lors du CEMRACS 2018. Je tiens donc à remercier Laurent Boudin, Céline Grandmont, Bérénice Grec et Sébastien Martin pour nous avoir si bien guidé. Un grand merci à ma binôme de projet, Amina, d'avoir rendu le travail ainsi que le séjour au CIRM si agréable. Je garderais un très bon souvenir de cet été passé à travailler, mais aussi à rigoler. Cela serait un grand plaisir de pouvoir travailler à nouveau ensemble.

Je tiens aussi à remercier toute l'équipe "poumon" : Cyril, Thomas, Michaël, Jonathan, Riccardo et Valentin. Cela a été un réel plaisir de travailler avec vous. Je garderais un très bon souvenir de nos nombreuses discussions pendant nos pauses café ainsi que pendant nos longues pauses déjeuner. Un merci particulier à Cyril et Thomas, mes compagnons de bureau, pour votre constante bonne humeur.

Pour finir, je voudrais bien sûr remercier toute ma famille qui a toujours été là pour moi. Plus spécialement, merci à ma soeur, Emmanuelle, mon beau-frère, Grégoire et à ma nièce Mathilde de m'avoir accueillie et supportée pendant le premier confinement. Merci à ma grand-mère, "mémé", d'avoir toujours cru en moi. Enfin, un immense merci à mes parents pour m'avoir toujours soutenue et pour avoir toujours cru en moi.

Contents

Chapter 1

Introduction

Nowadays, there is an urge to better understand pulmonary infections as their prevalence is increasing. Recently the coronavirus SARS-CoV-2 (COVID-19) has appeared in China and has spread to become a global pandemic [110]. This virus has affected over 70 millions of people and has killed over 1.6 millions of people, with these numbers still rising [92]. Two of its major symptoms are acute lung injury and acute respiratory distress [61]. Once the distress is too important, patients can be put on mechanical ventilators in order to maintain adequate levels of oxygen and carbon dioxide in the blood and to decrease the work of breathing [14, 87]. It is then essential to better understand how the ventilation is affected by an infection and how to minimize the work of breathing. This is the goal of the work of this thesis.

The lung is a complex system that serves as an exchange interface between the ambient air and the blood. It transports the oxygen present in the ambient air through its tree-like structure to the blood and removes carbon dioxide from it. However, because of its direct interface with the external environment, the lung is prone to develop infections. Once a pathogen starts infecting the lung, the immune system responds. This response is both mechanical and biological and can be supported by drug treatments to fight the infection quicker. The goal of the chapter 2 is to describe the physiology and biology of these complex systems in order to better understand their structures and their functions.

The study of the mechanisms of gas transport and of the exchanges of oxygen and carbon dioxide with the blood is a first step in order to understand how the system behaves. Hence, chapter 3 describes and analyzes a model of gas transport into an idealized human's lung. First, we assume that the transport mechanisms are independant on the time (stationnary equations) and an explicit solution can be computed. Then, in the non stationary case, the existence of an unique solution can be proved while assuming that the concentration of the oxygen and of the carbon dioxide is constant in the blood. Finally, when the gases are in the alveoli, they are exchanged with the blood, where they are transported under different forms, modeled in the last part of chapter 3.

The ventilation is characterized by the volume of air that is inspired (tidal volume) and by the frequency at which it is renewed (breathing frequency). These two values are stereotypic in humans and in mammals [117]. This raises the question: How has the ventilation been adjusted by evolution ? We search in chapter 4 for the optimal ventilation that minimizes the energy spent for breathing while fulfiling the body needs in oxygen. The optimal ventilation found is in full agreement with the physiological values for humans and for all mammals. Allometric scaling laws link the morphological and functional properties of mammals to their mass with a power law, and our model is able to predict accurately the allometric laws observed for breathing rates and inhaled air volumes.

However, during a lifetime, the lung may be confronted to several pulmonary infections that can affect the ventilation [78]. Hence, we propose in chapter 5 a model of a lung's infection to get an insight on how the dynamics of an infection can affect the ventilation and how its control could adapt to the morphological changes induced by the resulting inflammation. We model in chapter 5 the response of the innate biological immune system to a pathogen. We start by studying how the ventilation as well as the gaseous exchanges are affected in a simple case where the infection does not spread and remains in one bronchus only. Then, we model the propagation of the infection to its neighbouring bronchi. The model predicts that, depending on the localization of the infection in the lung and its stage, the lung's ventilation might become very costly in term of energy, up to a point where it is not able to sustain anymore the body needs in oxygen.

A medication treatment such as aerosol therapy can be supplied to help the immune system to fight an infection. In order to better understand the efficacy of this type of treatment, the deposit of aerosol particles in the first bifurcation of the human's lung is modeled in chapter 6. We track the behaviour of the droplets in the lung. We assume that they exchange water vapour with the air in the lung and that their temperature is affected by the temperature of their environment. We conclude that these hypotheses are important to model correctly the displacement and the potential deposit of the particles.

The biophysical problems encountered in this work have been studied using mathematical tools. We study the equations properties in chapters 3 and 6 thanks to functionnal analysis, we use optimization theory to minimize the energy in chapter 4 and numerical schemes are used to determine the numerical approximations of the solutions of the model equations.

All this work allows to better understand the lung's ventilation in humans and more generally, in all mammals, whether healthy or with a pulmonary infection.

Chapter 2

Elements of the physiology

In this chapter, we present some elements of the physiology about the respiratory system, the immune system and the aerosol therapy. A review of the literature concerning each modeling approaches will be detailed in the introductions of the corresponding chapters.

2.1 The respiratory system

Oxygen is essential for mammals. It takes part in the cellular respiration that happens in the cell's mitochondria. This process transforms glucose with the help of oxygen into carbon dioxide, water and adenosine trisphophate (ATP). This molecule stores energy and is used by all our body's cells. They are the sources of energy of the muscles and organs. Two structures allow the oxygen to be brought from the ambient air to the cells and the carbon dioxide from the cells to the ambient air: the lung that is the interface between the ambient air and the blood, and the blood network that transports the respiratory gases (oxygen and carbon dioxide) in the whole body.

2.1.1 The human's lung

The lung is an organ protected by the rib cage and supported by the diaphragm, a muscle that separates the thorax from the abdomen. It has a bifurcating tree-like geometry, almost dichotomic, as shown on Figure 2.1. This is why we can consider it as a succession of generations (Figure 2.2), where a generation corresponds to branches with the same number of bifurcations up to the root of the tree. The trachea is the first generation bronchus. It is the biggest branch and has a radius of around 0.9 cm [115]. The lung can be divided into two parts, the bronchial tree, a conductive zone because no exchange with the blood occurs and the acini, the exchange surface with the blood.

In an idealized view [115], the bronchial tree is composed of the seventeen first generations of the lung. Its goal is to bring the ambient air with a high concentration in oxygen and low concentration in carbon dioxide to the exchange surface. Since no exchange with the blood is made in this part of the lung, it is also called the

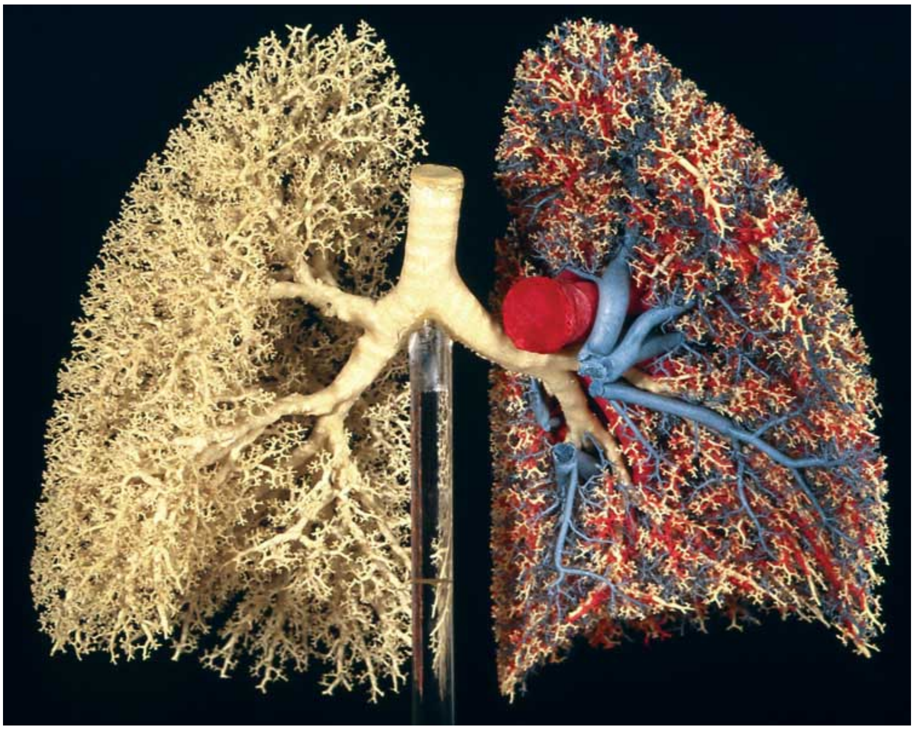

Figure 2.1: Cast of a human lung made by E.R. Weibel [113]. Bronchi are yellow, arteries are red and veins are blue.

conductive zone or the anatomic dead space. Its volume varies between individuals but it is around 150 mL [119].

The bifurcations are subject to some asymmetry. A mother bronchus divides into two daughters bronchi that are not identical, they may have differences in length and in diameter. As a matter of fact, the ratio between two sisters bronchi's diameter is around 0.8 for humans [105, 36]. This asymmetry can be explained by the development of the organ and its adaptation to the spacial configuration [21], by the increase of robustness against the variability of lung's sizes [37, 73] and by the adaptation of the lung to the anatomy [68]. The first bronchi have to bypass the heart, and divide the lung into three right lobes and two left lobes.

The acini are composed of roughly the six, seven last generations and occupy a volume of around 2.5 - 3 L which represents the majority of the volume of the lung [119]. On the contrary to the bronchial tree, the size of the alveolar ducts remains more or less constant throughout the acinus with a diameter of around 0.5 mm [115]. The exchange with the blood occurs in the alveoli that cover the walls of the ducts. They are more and more present as we go along the generations until they cover the totality of the walls of the ducts in the last generations. All these alveoli form an exchange surface of around 70-150 square meters [33, 102].

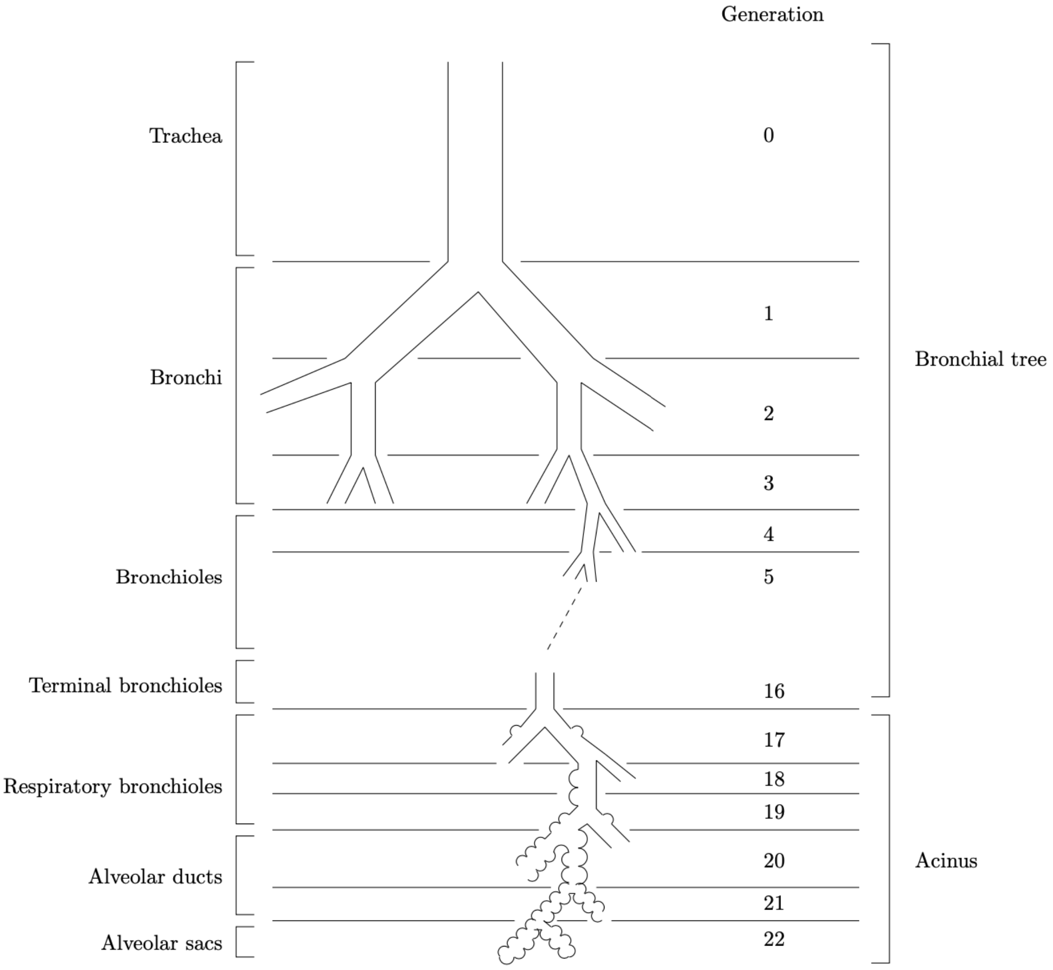

Figure 2.2: Structure of the human's lung. Reproduced from [115]. The bronchial tree is a conductive zone and the exchange with the blood is made in the acini.

2.1.2 Respiratory gas transport

Respiratory gases are transported through the lung by different mechanisms. In the first generations of the lung, the transport of gases is mainly made by convection thanks to the high velocity of the air flow which is around $1\,\mathrm{m}\cdot\mathrm{s}^{-1}$ in humans, in the trachea at rest [113]. Convection is the transport of a quantity by the movement of its surrounding environment. However, the more we advance in the generations, the smaller the velocity because of the increase of the total cross sectionals area of the bronchi. The ambient air is rich in oxygen and poor in carbon dioxide, and once it reaches the acinus, the velocity is small enough so that the diffusion becomes dominant. This mechanism is based on the Brownian motion of the molecules and induces a natural motion of these molecules from high concentration regions to low concentration regions. Gases are exchanged with the blood by diffusion through a thin membrane that separates the alveolar air from the blood (the alveolar capillary membrane). The deoxygenated blood present in the capillaries stocks up on oxygen and releases the carbon dioxide in the alveoli. In the blood capillaries, oxygen and carbon dioxide are transported under different forms [33, 68]. Oxygen is mostly combined to hemoglobin present in the red blood cells ($97\,\%$) which can fixed up to four molecules of oxygen. It can also be found under a dissolved form ($3\,\%$) in the plasma. Carbon dioxide is mainly carried though a combined form as bicarbonate ions (HCO_3^-) in the plasma after a chemical reaction ($60-65\,\%$). It is also combined to the hemoglobin present in the red blood cells ($30\,\%$) and, finally, under a dissolved form in the plasma ($5-10\,\%$).

2.1.3 Ventilation

Gas transport is performed thanks to the ventilation. During inspiration, the diaphragm and intercostal muscles contract and allows an expansion of the thorax that increases the volume of the lung. An airflow is created thanks to the difference in pressure between the ambient air and the acini. The volume of the air inhaled, known as the tidal volume, is approximately 500 mL at rest [119, 113]. Inspiration is an active mechanism because of the energy spent to contract the muscles. It lasts around 2 seconds at rest in humans. During expiration, the mechanism is different. There is a relaxation of the muscles that induces an elastic recoil to the initial volume of the lung and an ejection of the air previously inhaled. Expiration is considered to be a passive process because there is no energetic cost. It lasts around 3 seconds at rest in humans.

Since inspiration is an active process, it can be controlled and optimized to minimize the energy expenditure of ventilation. Indeed, it is based on the regulation of the volume of air that is inhaled (tidal volume) and on the frequency at which this volume of air is renewed (ventilation frequency) with the aim to satisfy the body's needs in oxygen. This analysis of the energy cost of ventilation can be extended to all mammals thanks to their common morphological and functional properties that are known to depend on their mass M with non trivial power laws, called allometric scaling laws [117, 113]. In all mammals, the lung is comprised of two regions: the bronchial tree which is a conductive zone and the acini where the exchange with the blood is made [83]. However, some differences in the geometry and the branching pattern can occur in the different species [105]. There exists three types of idealized branching patterns [83]. The first type is the monopodial branching pattern (rat, mouse...). At a bifurcation, a small bronchus branches from the main bronchus. The second one is the dichotomus branching pattern (human, monkey...). At a bifurcation, a mother bronchus divide into two daughters bronchi. Finally, the last one is the polychotomous branching pattern where a bronchus may divide into more than two bronchi.

2.2 Fighting pulmonary infections

The lung is prone to the development of infections. Because of the humidity of the air, the high concentration of oxygen and the lung being a direct interface with the external environment, viruses and bacteria can easily proliferate. However, there exists different types of defenses to fight these infections.

2.2.1 Immune response

The immune response is a complex process designed to defend the body against infection. This response can be divided into two parts, the innate immune response, that is fast, and the adaptative immune response [68].

The innate immune defense system is the first system to activate on the site of infection, it responds within minutes. The first defense of this system is the surface barriers, i.e. skin and mucosae. In the lung this protection consists in the mucus, a viscoelastic gel, and the ciliated cells on the bronchi's walls. The mucus, which catches the pathogens, is moved by the cilia towards the oesopharyngeal region, where it is either swallowed or expectorated [32]. Once a pathogen breaches this first defense, the second one comes into action. This internal defense is composed of chemicals and white blood cells, also called leucocytes, which are produced in the bone marrow. First, the macrophages already present in the respiratory epithelial barrier respond. These cells are phagocytes which means that they ingest and destruct pathogens. They also product citokines that summon other cells to the site of infection. Dendritic cells, also present in the respiratory epithelial barrier, capture the antigen of the pathogen and trigger the adaptative immune system. Next, neutrophils, present in the blood, arrive to the site of infection. They are the most numerous phagocytes in the body and they represent $60 - 70\,\%$ of all leucocytes. Others leucocytes such as basophiles and eosophiles, are present in the blood, but in small quantity.

The adaptative immune system, also called the acquired immune system, is composed of white blood cells called lymphocytes. This system is specific to a pathogen and create immunological memory after an initial infection. These cells are divided into two categories, the lymphocytes B and the lymphocytes T. The humoral immune response is the production by lymphocytes B of specific antibodies that corresponds to the encountered antigen. This system fights against pathogens before their entry in the human's cells. The cell mediated immune response fights against the infected cells. This response corresponds to an injection by the lymphocytes T of a toxic substance into the body's cells to destroy the infected cells.

Inflammation is a reaction from the immune system that appears at the site of infection once the tissue is injured. First, there is a vasodilation of the blood vessels due to the presence of chemical mediators released by the macrophages present in the tissue at the site of infection. It induces an increase of the blood supply and of the capillaries permeability which allows the passage of some of the plasma from the blood vessels to the tissue spaces. As a result of this inflow of plasma in the tissues, an oedema appears and it induces the migration of the leucocytes from the blood vessels to the site of infection.

2.2.2 Drug response

Medicines is sometimes prescribed to help the immune system to fight infections faster. Aerosol therapy is one of the major curative way to treat obstructive pulmonary diseases. It delivers drugs directly into the lung by inhaling solid or liquid particles that can remain dispersed in the air. It allows to have a high local drug concentration in the lung tissue and, because of its local distribution, it limits systemic toxicity, which is the occurance of toxic effects at multiple sites.

The deposition fraction, which is the fraction of inhaled particles that deposit, and the localization of this deposit are two of the most important characteristics of aerosol therapy. They depend on the interaction of three factors [78]. The first factor is the physical properties of the droplets like its mass or its shape. The second factor concerns the air flow. Indeed the ventilation frequency and the tidal volume can influence the deposit of the particles. Finally, the last factor is the anatomy of the bronchi, whether they are inflamed and hence partially blocked, or healthy. Usually droplets have a tendency to deposit more in the first generations bronchi. It is due to the inertial impaction which happens when a particle fails to follow the streamlines of the air flow. Therefore the particles impact on the obstacle instead of bypassing it.

Chapter 3

Gas transport model

The main goal of the respiratory system is to supply the body with oxygen and to remove carbon dioxide from it. During inspiration, fresh air with a high concentration in oxygen and low concentration in carbon dioxide is brought from the nose and the mouth through the bronchial tree to the alveolar region. Once in the acinus, oxygen and carbon dioxide exchanges take place by diffusion through the alveolar membrane to or from the blood capillaries. At expiration, a higher carbon dioxide and lower oxygen concentration is expelled from the lung until fresh air comes in again at the next inspiration [119]. The fulfillment of the required gas exchange is made possible by the thin alveolar membrane combined with a large alveolar surface.

Two main appproaches have been proposed in the litterature to model gas transport. The first one is based on an effective diffusion in porous media [59, 60, 10]. This type of approach have the benefit of working with an homogeneous material mimicking the last generations of the lung. The second approach is one based on tree-like structures [57, 95, 69, 17]. This type of models have the benefit of having a detailed description of gas transport.

We choose this last approach for our model, with the main hypotheses that the lung is a symmetric dichotomic bifurcating tree [113, 70] connecting ambient air to an exchange surface and ventilated thanks to an airflow that varies with time as a sine function.

3.1 Oxygen and carbon dioxide transport in the lung

3.1.1 Geometry of the human lung

Our geometrical model mimicking the human lung is based on a symmetric dichotomic bifurcating tree [70]. A generation corresponds to branches with the same number of bifurcations from the root of the tree that mimics the trachea. Our bronchi are assumed to be cylindrical. The tree is divided into two distinct parts [113]: the first G generations ($G = 17$) form the conductive tree and the last H generations ($H = 6$) form the acini, where exchanges with blood occur.

To account for the core geometrical properties of the lung, we assume that the size of the branches in the conductive tree decreases from one generation to the next with a ratio $0 < h < 1$ [113, 70, 56]:

$$l_{i+1} = l_i h \Rightarrow l_i = l_0 h^i,$$
$$r_{i+1} = r_i h \Rightarrow r_i = r_0 h^i,$$

with l_i the length and r_i the radius of a generation i branch ($i \in [\![0, G-1]\!]$). Furthermore, we assume that in the acinus, the size of the bronchi remains constant [113]. It means that the factor h is equal to one. We can deduce that the radius r_A and the length l_A of the branches in the acinus are respectively equal to the radius and length of the branches of the last generation in the conductive tree.

We can express the lumen area S_i of a branch in generation i with the radius, $S_i = \pi r_i^2$. Consequently, the area of one branch decreases with the generation in the conductive tree, $S_i = h^{2i} S_0$ but remains constant in the acinus, $S_A = h^{2(G-1)} S_0$.

The volumetric flow rate in a branch from generation i is the product of the fluid velocity u_i and the lumen area of the branch S_i. We assume here that air is an incompressible fluid because compressibility effects are considered small even during forced expiration [30]. Consequently, mass conservation between a branch in generation i and its two daughters in generation $i+1$ leads to a scaling on the mean air velocity u_i in each generation,

$$u_{i+1} S_{i+1} = \frac{u_i S_i}{2} \quad \Rightarrow \quad u_i = \left(\frac{1}{2h^2}\right)^i u_0.$$

We can rewrite this equation for the acinus, we obtain for $i \in [\![G, N]\!]$, where $N = G + H - 1$,

$$u_i = \frac{u_{G-1}}{2^{i-G+1}}.$$

3.1.2 Model equations

Now that a model for the lung's geometry is defined, we can expressed the equations of the gas transport in each bronchi. We assume the bronchi to be cylindrical. The transport of oxygen and carbon dioxide in the bronchial tree is driven by three main phenomena: convection, diffusion and exchange with the walls in the case of the acini. We will describe the fluid motion along the axis of the bronchus, using a unidimensional model in space. As the bronchi and the fluid properties are the same in all the branches from a same generation, the equations of transport are the same for each branch in a same generation.

Let us evaluate the matter balance (see Figure 3.1) in a cylinder slice localized in x and with a thickness dx. We denote $C_i(x)$ the mean O_2 or CO_2 concentration ($\mathrm{mol} \cdot \mathrm{m}^{-3}$) in the section. The quantity of matter entering the slice by the left side Q_l writes,

$$Q_l = \left(u_i(t) C_i(x) - D \frac{dC_i}{dx}(x)\right) \pi r_i^2,$$

where D is the diffusion coefficient in air of the species considered ($\mathrm{m}^2 \cdot \mathrm{s}^{-1}$), $u_i(t)$ is the mean velocity of the fluid ($\mathrm{m} \cdot \mathrm{s}^{-1}$) and r_i is the radius (m) of the bronchus

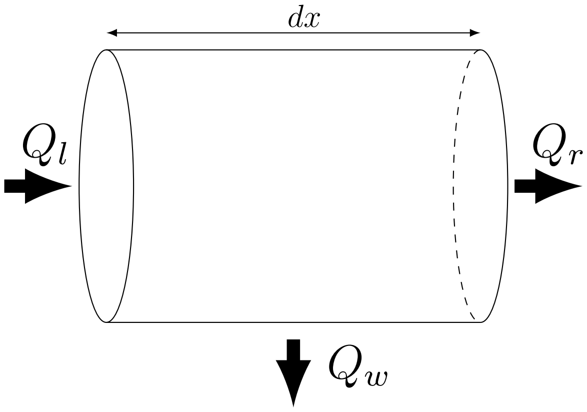

Figure 3.1: Matter balance in a slice of a bronchus.

of generation i. Then the quantity of matter leaving the slice by the right side Q_r writes,

$$Q_r = -\left(u_i(t)C_i(x+dx) - D\frac{dC_i}{dx}(x+dx)\right)\pi r_i^2.$$

Finally the quantity of matter exchanged with the bronchus walls writes,

$$Q_w = -\alpha_i \varrho_s \left(P_i(x) - P_{\text{blood}}\right) 2\pi r_i dx,$$

where P_i is the mean O_2 or CO_2 partial pressure (mmHg) on the section, and P_{blood} is the O_2 or CO_2 partial pressure (mmHg) in the blood. The amount of exchange surface per unit of alveolar duct surface, $\varrho_s \approx 9.3$ is computed as the ratio of the alveolar surface over the bronchial surface in the acinus [115, 81]. Assuming that each alveoli is half a sphere, the alveolar surface is computed as follow, $S_A = 2\pi r_A^2 \times N_{alv} \approx 150\,\text{m}^2$, where r_A is the radius of the bronchi in the acinus and $N_{alv} = 480 \times 10^6$ is the number of alveoli in the human lung [81]. α_i is the permeability of the alveolar membrane ($\text{mol} \cdot \text{m}^{-2} \cdot \text{s}^{-1} \cdot \text{mmHg}^{-1}$), we can express it as follow [34]

$$\alpha_i = \begin{cases} 0, & \text{for } i \in [\![0, G-1]\!], \\ \alpha = \dfrac{D_{gas,H_2O}\sigma_{gas,H_2O}}{\tau}, & \text{for } i \in [\![G, N]\!], \end{cases} \tag{3.1}$$

where D_{gas,H_2O} is the diffusion coefficient of the gas in water ($\text{m}^2 \cdot \text{s}^{-1}$), σ_{gas,H_2O} is the solubility coefficient ($\text{mol} \cdot \text{m}^{-3} \cdot \text{mmHg}^{-1}$) of the gas in water and finally τ is the thickness (m) of the alveolar membrane.

Finally, the variation of the gas concentration over time writes,

$$\pi r_i^2 dx \frac{\partial C_i}{\partial t} = Q_l + Q_r + Q_w.$$

Making the length of the slice dx go to zero, we obtain for $x \in [0, l_i]$,

$$\frac{\partial C_i}{\partial t}\pi r_i^2 \underbrace{- D\frac{\partial^2 C_i}{\partial x^2}\pi r_i^2}_{\text{diffusion}} + \underbrace{u_i(t)\frac{\partial C_i}{\partial x}\pi r_i^2}_{\text{convection}} + \underbrace{\alpha_i \varrho_s \left(P_i - P_{\text{blood}}\right) 2\pi r_i}_{\text{exchange with blood}} = 0.$$

As the concentration and the partial pressure are proportional, we can work only with partial pressure. We can then define the transport dynamics of the partial pressure of oxygen and carbon dioxide in a single branch from the previous equation,

$$\frac{\partial P_i}{\partial t} - \underbrace{D\frac{\partial^2 P_i}{\partial x^2}}_{\text{diffusion}} + \underbrace{u_i(t)\frac{\partial P_i}{\partial x}}_{\text{convection}} + \underbrace{\beta_i\left(P_i - P_{\text{blood}}\right)}_{\text{exchange with blood}} = 0 \quad \text{for } x \in [0, l_i]. \tag{3.2}$$

The exchange coefficient β_i (s^{-1}) is expressed as follow,

$$\beta_i = \begin{cases} 0, & \text{for } i \in [\![0, G-1]\!], \\ \varrho_s \dfrac{2k}{r_A}\alpha_i & \text{for } i \in [\![G, N]\!], \end{cases} \tag{3.3}$$

where k is the ratio relating partial pressure of the gas to its concentration in water and r_A is the radius of the branches in the acinus.

3.1.3 Boundary conditions

The bronchi are connected together with bifurcations. Mass conservation in the bifurcation leads to

$$S_i\left(u_i(t)P_i(t,l_i) - D\frac{\partial P_i(t,l_i)}{\partial x}\right) = 2S_{i+1}\left(u_{i+1}(t)P_{i+1}(t,0) - D\frac{\partial P_{i+1}(t,0)}{\partial x}\right).$$

We suppose that we have partial pressure continuity at bifurcations, it writes $P_i(t,l_i) = P_{i+1}(t,0)$. Mass conservation can then be rewritten,

$$-DS_i\frac{\partial P_i(t,l_i)}{\partial x} = -2DS_{i+1}\frac{\partial P_{i+1}(t,0)}{\partial x}. \tag{3.4}$$

To close the system of equations, boundary conditions at both ends of the tree are needed. We assume $P_0(t,0) = P_{\text{air}}$ at the inlet of the root of the tree that models the trachea where P_{air} is the partial pressure of the gas considered in the air. And for the end of the last generation of the acini, we use a flux boundary condition, based on the exchange laws previously defined,

$$-D\frac{\partial P_N}{\partial x}(t,l_N) = \alpha k \varrho_s\left(P_N(t,l_N) - P_{\text{blood}}\right).$$

3.1.4 Oxygen and carbon dioxide flow

Our model allows to easily compute the oxygen and carbon dioxide flows exchanged with the blood. Indeed, we just need to provide a temporal velocity profile to our equations to obtain the partial pressure of the gases in all the bronchi of the lung. To simulate the ventilation, we suppose that the velocity at the entrance of the trachea follows a periodic pattern written as follow,

$$u_0(t) = A\sin\left(\frac{2\pi}{T}t\right),$$

where A is the amplitude of the ventilation ($\mathrm{m} \cdot \mathrm{s}^{-1}$) and T is the ventilation's period (s). Then, both flows depend only on the amplitude and the period of the ventilation, thanks to the difference of partial pressures between the alveolar region and the blood,

$$f(A,T) = \sum_{i=G}^{N} \frac{2^i}{T} \int_{t_C}^{t_C+T} \int_0^{l_i} \gamma \left(P_i(t,x) - P_{\mathrm{blood}}\right) \mathrm{d}x \, \mathrm{d}t, \tag{3.5}$$

with t_C a time at which the system has reached a periodic regime, and

$$\gamma = 2\pi r_A \alpha \varrho_s. \tag{3.6}$$

3.1.5 Choice of physiological parameters

Our model is based on a set of anatomical parameters that needs to be quantified from the physiology. The parameters' list and values for humans are shown on Table 3.1. The lung's geometry is defined from the radius (r_0) of the root of the branch, mimicking the trachea, and from the size reduction factor h that allows to compute the radius and lengths of all the branches in the tree. The length of the branches is related to the diameter of branches using the ratio $\frac{l_0}{2r_0} = 3$ [71, 105], and we use $l_0 = 6r_0$. Although this value is not fully accurate for the main bronchi, it is a good approximation for the other branches. Since, the global behavior is mainly driven by the most numerous bronchi, extending the length over diameter ratio to all the branch of the tree is a reasonable approximation. Furthermore to describe properly the gas exchange between air and blood, we also need the thickness of the alveolar membrane.

PARAMETERS	VALUES
Radius of the trachea	$0.9 \cdot 10^{-2}$ m [71]
Homothetic ratio (h)	0.7937 [71]
Thickness of the alveolar membrane	$1 \cdot 10^{-6}$ m [34]

Table 3.1: Table of parameters for the geometry of the human's lung.

Once the geometry of the lung is defined, we can define the parameters linked to the oxygen and the carbon dioxide behaviors, see Table 3.2 and Table 3.3. In order to solve equation (3.2), we need the oxygen and the carbon dioxide diffusion coefficients in air, and the partial pressure of the gas in the blood. The diffusion coefficient of the gas in water, the solubility coefficient of the gas in blood and the dimensionless Henry solubility allows to describe the gas exchanges between alveolar gas and blood. The dimensionless Henry solubility is the ratio between the aqueous-phase concentration of a gas and its gas-phase concentration. It can be computed as the product of the solubility coefficient in the blood, the gas constant and the temperature [94]. The temperature in our model is fixed at 310.15 K (37^o Celsius). Finally for the boundary condition at the entry of the trachea, we need the partial pressure of the gases in the ambient air.

PARAMETERS	VALUES
Diffusion coefficient in air	$0.2 \cdot 10^{-4}\ \mathrm{m}^2 \cdot \mathrm{s}^{-1}$ [71]
Partial pressure in the blood	40 mmHg [33]
Diffusion coefficient in water	$3.3 \cdot 10^{-9}\ \mathrm{m}^2 \cdot \mathrm{s}^{-1}$ [34]
Solubility coefficient in the blood	$1.34 \cdot 10^{-3}\ \mathrm{mol} \cdot \mathrm{m}^{-3} \cdot \mathrm{mmHg}^{-1}$ [62]
Henry solubility	$2.592 \cdot 10^{-2}$ [94]
Partial pressure in the air	150 mmHg [33]

Table 3.2: Table of parameters for the oxygen

PARAMETERS	VALUES
Diffusion coefficient in air	$0.14 \cdot 10^{-4}\ \mathrm{m}^2 \cdot \mathrm{s}^{-1}$ [71]
Partial pressure in the blood	47 mmHg [33]
Diffusion coefficient in water	$2.505 \cdot 10^{-9}\ \mathrm{m}^2 \cdot \mathrm{s}^{-1}$ [67]
Solubility coefficient in the blood	$3.07 \cdot 10^{-2}\ \mathrm{mol} \cdot \mathrm{m}^{-3} \cdot \mathrm{mmHg}^{-1}$ [49]
Henry solubility	0.594 [94]
Partial pressure in the air	0.3 mmHg [33]

Table 3.3: Table of parameters for the carbon dioxide

3.2 Analysis of the model

In order to see if our problem is well posed and has a solution, we need to analyze it. For simplicity, let us first adimensionalize our equation (3.2) in space. We make here a misuse of langage as we keep the same notations for the dimensionless variables than for the dimensional ones in equation (3.2). We obtain,

$$\frac{\partial P_i}{\partial t} - \frac{D}{l_i^2}\frac{\partial^2 P_i}{\partial x^2} + \frac{u_i(t)}{l_i}\frac{\partial P_i}{\partial x} + \beta_i \left(P_i - P_{\text{blood}}\right) = 0 \quad \text{for } x \in [0,1], \tag{3.7}$$

and we assume in this section that the partial pressure in the blood P_{blood} is a constant.

3.2.1 Stationnary case

In our analysis, we start by simplifying our model. Let us study the stationnary case and observe if it could be a good enough approximation of the non-stationnary solution.

We want to resolve the equations in the stationnary case. It means that for all $i \in [\![0, N]\!]$, we have

$$\frac{\partial P_i}{\partial t} = 0,$$

and now P_i depends only on the space variable x.

Each equations can be rewritten as follow,

$$-\frac{D}{l_i^2}\frac{\mathrm{d}^2 P_i}{\mathrm{d}x^2} + \frac{u_i}{l_i}\frac{\mathrm{d}P_i}{\mathrm{d}x} + \beta_i P_i = \beta_i P_{blood},$$

or,

$$\frac{\mathrm{d}^2 P_i}{\mathrm{d}x^2} - \frac{u_i l_i}{D}\frac{\mathrm{d}P_i}{\mathrm{d}x} - \frac{\beta_i l_i^2}{D} P_i = -\frac{\beta_i l_i^2}{D} P_{\text{blood}}. \tag{3.8}$$

Air velocity $u_i = 0$

In this paragraph, we suppose that the air velocity is equal to zero. We know that in the convective tree ($i \in [\![0, G-1]\!]$) the coefficient β_i is equal to zero. We just have to solve,

$$\frac{\mathrm{d}^2 P_i}{\mathrm{d}x^2} = 0.$$

The solution is a linear function,

$$P_i(x) = A_i x + B_i.$$

In the acinus ($i \in [\![G, N]\!]$), we have to solve the following equation,

$$\frac{\mathrm{d}^2 P_i}{\mathrm{d}x^2} - \frac{\beta_i l_i^2}{D} P_i = -\frac{\beta_i l_i^2}{D} P_{\text{blood}}.$$

We start by solving the homogeneous equations. The solutions are,

$$P_i(x) = A_i e^{rx} + B_i e^{-rx},$$

where $r = l_N \sqrt{\beta_N / D}$.
P_{blood} is a constant, therefore it is a particular solution. We obtain,

$$P_i(x) = A_i e^{rx} + B_i e^{-rx} + P_{\text{blood}}$$

Now we want to find the coefficients A_i et B_i. In order to do that we need boundary conditions and bifurcations conditions. We have,

$$\begin{cases} P_0(0) = P_{\text{air}} \\ -\dfrac{DS_i}{l_i}\dfrac{\mathrm{d}P_i(1)}{\mathrm{d}x} = -\dfrac{2DS_{i+1}}{l_{i+1}}\dfrac{\mathrm{d}P_{i+1}(0)}{\mathrm{d}x} \\ P_i(1) = P_{i+1}(0) \\ -\dfrac{D}{l_N}\dfrac{\mathrm{d}P_N(1)}{\mathrm{d}x} = \alpha k \varrho_s \left(P_N(1) - P_{\text{blood}}\right) \end{cases}$$

With the explicit solution we can deduce,

$$B_0 = P_{\text{air}}.$$

For $i \in [\![0, G-2]\!]$, we have

$$\begin{cases} A_i = 2h A_{i+1}, \\ A_i + B_i = B_{i+1}. \end{cases}$$

At the bifurcation between the bronchial tree and the acinus, we obtain,

$$\begin{cases} A_{G-1} = 2rA_G - 2rB_G, \\ A_{G-1} + B_{G-1} = A_G + B_G + P_{\text{blood}}. \end{cases}$$

For $i \in [\![G, N-1]\!]$, we have,

$$\begin{cases} A_i re^r - B_i re^{-r} = 2\left(A_{i+1}r - B_{i+1}r\right), \\ A_i e^r + B_i e^{-r} = A_{i+1} + B_{i+1}. \end{cases}$$

Finally we have,

$$A_N e^r \left(\frac{D}{l_N} r + \alpha k \varrho_s\right) + B_N e^{-r} \left(-\frac{D}{l_N} r + \alpha k \varrho_s\right) = 0.$$

All these coefficients are easily found by solving a linear system.

Let us make an example by computing the explicit solution for a tree containing only two generations ($N = 1$), one in the bronchial tree ($G = 1$) and one in the acinus ($H = 1$). The solution in the first generation is then,

$$P_0(x) = A_0 x + B_0.$$

The solution in the second generation writes,

$$P_1(x) = A_1 e^{rx} + B_1 e^{-rx} + P_{\text{blood}}.$$

In this case, we need four equations to compute the coefficients A_0, B_0, A_1 and B_1. The first one corresponds to the boundary condition at the entrance of the tree. It writes,

$$B_0 = P_{\text{air}}.$$

The next two equations are the ones corresponding to the birfurcations conditions and since there are only two generations in our example, the bifurcation is the one between the bronchial tree and the acinus. We have,

$$\begin{aligned} A_0 &= 2rA_1 - 2rB_1, \\ A_0 + B_0 &= A_1 + B_1 + P_{\text{blood}}. \end{aligned}$$

Finally the last equation corresponds to the boundary conditions at the outlets of the tree. It writes,

$$A_1 e^r \left(\frac{D}{l_1} r + \alpha k \varrho_s\right) + B_1 e^{-r} \left(-\frac{D}{l_1} r + \alpha k \varrho_s\right) = 0.$$

This equations can be rewritten as a linear system, defined as follow, $MX = V$. We have,

$$M = \begin{pmatrix} 1 & 0 & 0 & 0 \\ 0 & 1 & a & -a \\ -1 & -1 & 1 & 1 \\ 0 & 0 & b & c \end{pmatrix}, \text{ with } a = 2r,\ b = e^{-r}\left(-\frac{D}{l_1} r + \alpha k \varrho_s\right)$$

$$\text{and } c = e^r \left(\frac{D}{l_1} r + \alpha k \varrho_s \right).$$

$$X = \begin{pmatrix} B_0 \\ A_0 \\ B_1 \\ A_1 \end{pmatrix} \text{ and } V = \begin{pmatrix} P_{\text{air}} \\ 0 \\ -P_{\text{blood}} \\ 0 \end{pmatrix}.$$

The coefficients A_0, B_0, A_1 and B_1 are easily found by computing the inverse of the matrix M. Indeed we have $X = M^{-1}V$. The inverse of the matrix M is equal to,

$$M^{-1} = \begin{pmatrix} 1 & 0 & 0 & 0 \\ \frac{-ab-ac}{dM} & \frac{c-b}{dM} & \frac{-ab-ac}{dM} & \frac{2a}{dM} \\ \frac{c}{dM} & \frac{c}{dM} & \frac{c}{dM} & \frac{a-1}{dM} \\ \frac{-b}{dM} & \frac{-b}{dM} & \frac{-b}{dM} & \frac{a+1}{dM} \end{pmatrix},$$

where $dM = b(2r-1) + c(2r+1)$, is the determinant of the matrix M.

We can then deduce the coefficients,

$$\begin{cases} B_0 = P_{\text{air}} \\ A_0 = \dfrac{(P_{\text{air}} - P_{\text{blood}})(-2rb - 2rc)}{dM} \\ B_1 = \dfrac{(P_{\text{air}} - P_{\text{blood}})c}{dM} \\ A_1 = -\dfrac{(P_{\text{air}} - P_{\text{blood}})b}{dM}. \end{cases}$$

Thanks to these coefficients, we have found the explicit solution of the equation (3.8) in a tree with two generations and when $u_i = 0$.

The explicit solution of the equation (3.8) for oxygen when $u_i = 0$ in a tree mimicking the human lung with 23 generations including 17 in the bronchial tree and 6 in the acinus is shown on Figure 3.2). Since $u_i = 0$, the transport of the gases is only made by diffusion. It explains the steep decrease of the partial pressure in the first generations of the tree.

Air velocity $u_i \neq 0$

In this section, we suppose that the air velocity is different than zero. We start by solving the homogeneous equations. In order to do that we need to solve the characteristic polynomial,

$$r_i^2 - \frac{u_i l_i}{D} r_i - \frac{\beta_i l_i^2}{D} = 0.$$

We know that in the bronchial tree no exchange is made with the blood which implies that $\beta_i = 0$. We then obtain two roots to our equation in the bronchial tree,

$$r_{i,1} = \frac{u_i l_i}{D},$$

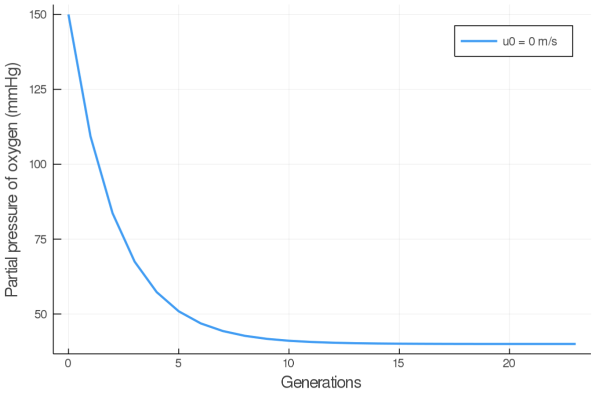

Figure 3.2: Explicit solution of the equation (3.8) for oxygen in a tree of 23 generations with 17 generations in the bronchial tree and 6 generations in the acinus when $u_i = 0$.

and,

$$r_{i,2} = 0.$$

In the acinus, since exchange is made with the blood, we have $\beta_i > 0$ and hence we compute,

$$\Delta = \frac{u_i^2 l_i^2}{D^2} + \frac{4\beta_i l_i^2}{D} = \frac{l_i^2}{D^2}\left(u_i^2 + 4\beta_i D\right) > 0.$$

We also obtain two roots,

$$r_{i,1} = \frac{u_i l_i}{2D} + \frac{\sqrt{\Delta}}{2} = \frac{l_i}{2D}\left(u_i + \sqrt{u_i^2 + 4\beta_i D}\right),$$

and,

$$r_{i,2} = \frac{u_i l_i}{2D} - \frac{\sqrt{\Delta}}{2} = \frac{l_i}{2D}\left(u_i - \sqrt{u_i^2 + 4\beta_i D}\right).$$

The solutions of the homogeneous equations are,

$$P_i(x) = A_i e^{r_{i,1}x} + B_i e^{r_{i,2}x}.$$

Since P_{blood} is a constant, it is also a particular solution. The solution of the equations are then,

$$P_i(x) = A_i e^{r_{i,1}x} + B_i e^{r_{i,2}x} + P_{\text{blood}}.$$

In order to find the coefficients A_i and B_i, we need the boundary conditions and the bifurcation conditions. We have,

$$\left\{\begin{array}{c} P_0(0) = P_{\text{air}} \\ -\dfrac{DS_i}{l_i}\dfrac{\mathrm{d}P_i(1)}{\mathrm{d}x} = -\dfrac{2DS_{i+1}}{l_{i+1}}\dfrac{\mathrm{d}P_{i+1}(0)}{\mathrm{d}x} \\ P_i(1) = P_{i+1}(0) \\ -\dfrac{D}{l_N}\dfrac{\mathrm{d}P_N(1)}{\mathrm{d}x} = \alpha k \varrho_s \left(P_N(1) - P_{\text{blood}}\right) \end{array}\right.$$

Thanks to the explicit solutions we obtain,

$$A_0 + B_0 = P_{\text{air}} - P_{\text{blood}}.$$

For $i \in [\![0, G-2]\!]$, we have,

$$\begin{cases} A_i r_{i,1} e^{r_{i,1}} + B_i r_{i,2} e^{r_{i,2}} = 2h \left(A_{i+1} r_{i+1,1} + B_{i+1} r_{i+1,2} \right), \\ A_i e^{r_{i,1}} + B_i e^{r_{i,2}} = A_{i+1} + B_{i+1}. \end{cases}$$

For $i \in [\![G-1, N-1]\!]$, we have,

$$\begin{cases} A_i r_{i,1} e^{r_{i,1}} + B_i r_{i,2} e^{r_{i,2}} = 2 \left(A_{i+1} r_{i+1,1} + B_{i+1} r_{i+1,2} \right), \\ A_i e^{r_{i,1}} + B_i e^{r_{i,2}} = A_{i+1} + B_{i+1}. \end{cases}$$

Finally we have,

$$A_N e^{r_{N,1}} \left(\frac{D}{l_N} r_{N,1} + \alpha k \varrho_s \right) + B_N e^{r_{N,2}} \left(\frac{D}{l_N} r_{N,2} + \alpha k \varrho_s \right) = 0.$$

All these coefficients can be determined by solving a linear system. Thanks to them we can find the explicit solutions for the equation (3.8) for all generations in the case $u_i \neq 0$.

Let us also make an example by computing the explicit solution for a tree containing only two generations ($N = 1$), one in the bronchial tree ($G = 1$) and one in the acinus ($H = 1$). The solution in the first generation is then,

$$P_0(x) = A_0 e^{r_{0,1} x} + B_0 e^{r_{0,2} x} + P_{\text{blood}}.$$

We know that in the bronchial tree, we have $r_{0,2} = 0$. The solution can then be rewritten as follow,

$$P_0(x) = A_0 e^{r_{0,1} x} + B_0 + P_{\text{blood}}.$$

The solution in the second generation writes,

$$P_1(x) = A_1 e^{r_{1,1} x} + B_1 e^{r_{1,2} x} + P_{\text{blood}}.$$

In this case, we need four equations to compute the coefficients A_0, B_0, A_1 and B_1. The first one corresponds to the boundary condition at the entrance of the tree. It writes,

$$A_0 + B_0 = P_{\text{air}} - P_{\text{blood}}.$$

The next two equations are the ones corresponding to the birfurcations conditions between the bronchial tree and the acinus. We have since $r_{0,2} = 0$,

$$\begin{aligned} A_0 r_{0,1} e^{r_{0,1}} &= 2 \left(A_1 r_{1,1} + B_1 r_{1,2} \right), \\ A_0 e^{r_{0,1}} + B_0 &= A_1 + B_1. \end{aligned}$$

Finally the last equation corresponds to the boundary conditions at the outlets of the tree. It writes,

$$A_1 e^{r_{1,1}}\left(\frac{D}{l_1}r_{1,1}+\alpha k\varrho_s\right)+B_1 e^{r_{1,2}}\left(\frac{D}{l_1}r_{1,2}+\alpha k\varrho_s\right)=0.$$

This four equations can be rewritten as a linear system, written as follow, $MX = V$, where,

$$M=\begin{pmatrix}1 & 1 & 0 & 0\\ 0 & a & b & c\\ -1 & d & 1 & 1\\ 0 & 0 & f & g\end{pmatrix},\ \text{with } a=r_{0,1}e^{r_{0,1}},\ b=-2r_{1,2},\ c=-2r_{1,1}$$

$$d=-e^{r_{0,1}},\ f=e^{r_{1,2}}\left(\frac{D}{l_1}r_{1,2}+\alpha k\varrho_s\right)\ \text{ and } g=e^{r_{1,1}}\left(\frac{D}{l_1}r_{1,1}+\alpha k\varrho_s\right).$$

$$X=\begin{pmatrix}B_0\\ A_0\\ B_1\\ A_1\end{pmatrix}\ \text{and } V=\begin{pmatrix}P_{\text{air}}-P_{\text{blood}}\\ 0\\ 0\\ 0\end{pmatrix}.$$

The coefficients four coefficients of the vector X are easily found by computing the inverse of the matrix M. Indeed we have $X = M^{-1}V$. The inverse of this matrix M is written as follow,

$$M^{-1}=\frac{1}{dM}\begin{pmatrix}-af+cdf+ag-bdg & f-g & bg-cf & c-b\\ cf-bg & g-f & cf-bg & b-c\\ ag & -dg-g & ag & -a+c+cd\\ -af & df+f & -af & a-b-bd\end{pmatrix}$$

where the dM is the determinant of the matrix M. It is equal to,

$$\begin{aligned}dM =& f(-a+c+cd)+g(a-b-bd)\\ =& f\left(-r_{0,1}e^{r_{0,1}}-2r_{1,1}+2r_{1,1}e^{r_{0,1}}\right)+g\left(r_{0,1}e^{r_{0,1}}+2r_{1,2}-2r_{1,2}e^{r_{0,1}}\right).\end{aligned}$$

The coefficients can then be easily deduced. We obtain,

$$\begin{cases}B_0=\dfrac{(P_{\text{air}}-P_{\text{blood}})(-r_{0,1}e^{r_{0,1}}f+2r_{1,1}e^{r_{0,1}}f+r_{0,1}e^{r_{0,1}}g-2r_{1,2}e^{r_{0,1}}g)}{dM}\\ A_0=\dfrac{(P_{\text{air}}-P_{\text{blood}})(-2r_{1,1}f+2r_{1,2}g)}{dM}\\ B_1=\dfrac{(P_{\text{air}}-P_{\text{blood}})r_{0,1}e^{r_{0,1}}g}{dM}\\ A_1=\dfrac{(P_{\text{air}}-P_{\text{blood}})(-r_{0,1}e^{r_{0,1}}f)}{dM}\end{cases}$$

Thanks to these coefficients, we have found the explicit solution of the equation (3.8) in a tree with two generations and when $u_i \neq 0$.

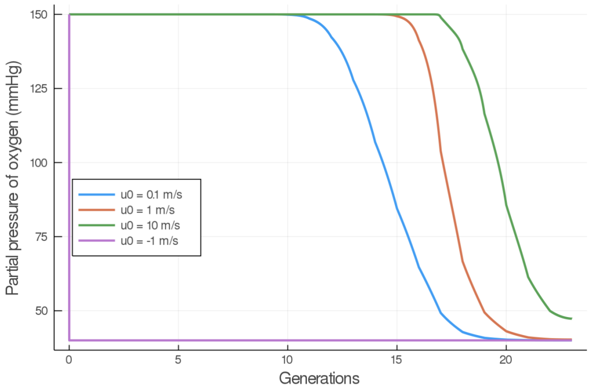

Figure 3.3: Explicit solution of the equation (3.8) in a tree of 23 generations with 17 generations in the bronchial tree and 6 generations in the acinus for different velocities $u_i \neq 0$.

The explicit solution of the equation (3.8) in the case of oxygen for different non null velocities in a tree mimicking the human lung with 23 generations (17 in the bronchial tree and 6 in the acinus) is shown on Figure 3.3. With a high velocity, the convection is important and hence, induces the air flow to go deep into the lung. However, when the velocity is negative the oxygen partial pressure goes from its value in the ambient air to the one in the blood instantaneously. This phenomenon is due to the boundary condition at the entrance of the tree. Indeed, we impose the same partial pressure in the ambient air and at the entrance of the trachea, alrhough the exhaled air flow is poor in oxygen.

Continuity of the solution in time

We obtained two solutions, one when $u_i = 0$ and one when $u_i \neq 0$. We now want to prove that the overall solution is continuous relatively to u_i in $u_i = 0$. It means that we want to see if the solution when $u_i \to 0$ tends to the solution when $u_i = 0$.

Proposition 3.2.1 (Continuity of the non stationnary solution)**.** *The solution of the following equation,*

$$\frac{d^2 P_i}{dx^2} - \frac{u_i l_i}{D}\frac{dP_i}{dx} - \frac{\beta_i l_i^2}{D} P_i = -\frac{\beta_i l_i^2}{D} P_{blood},$$

is continuous relatively to u_i in $u_i = 0$

Proof. For simplicity let us prove the continuity of the solution relatively to u_i in a reduced tree. We suppose that our tree only have two generations, one in the convective tree and one in the acinus.

First let us recall the explicit solutions of the equation (3.8) computed in the previous section. Let us denote with an exponent 0 the solutions when $u_i = 0$ and with an exponent 1 the solutions when $u_i \neq 0$.

When $u_i = 0$, the solutions are the following functions,

$$P_0^0(x) = A_0^0 x + B_0^0,$$

$$P_1^0(x) = A_1^0 e^{rx} + B_1^0 e^{-rx} + P_{\text{blood}}.$$

We have $r = l_N\sqrt{\beta_N/D}$, and

$$\begin{cases} B_0^0 = P_{\text{air}}, \\ A_0^0 = \dfrac{(P_{\text{air}} - P_{\text{blood}})\left(-2re^{-r}\left(-\frac{D}{l_1}r + \alpha k\varrho_s\right) - 2re^{r}\left(\frac{D}{l_1}r + \alpha k\varrho_s\right)\right)}{dM^0} \\ B_1^0 = \dfrac{(P_{\text{air}} - P_{\text{blood}})e^{r}\left(\frac{D}{l_1}r + \alpha k\varrho_s\right)}{dM^0} \\ A_1^0 = -\dfrac{(P_{\text{air}} - P_{\text{blood}})e^{-r}\left(-\frac{D}{l_1}r + \alpha k\varrho_s\right)}{dM^0}, \end{cases}$$

and $dM^0 = e^{-r}\left(-\frac{D}{l_1}r + \alpha k\varrho_s\right)(2r-1) + e^{r}\left(\frac{D}{l_1}r + \alpha k\varrho_s\right)(2r+1)$.

When $u_i \neq 0$ the solutions are the following functions,

$$\begin{aligned} P_0^1(x) &= A_0^1 e^{r_{0,1}x} + B_0^1 + P_{\text{blood}}, \\ P_1^1(x) &= A_1^1 e^{r_{1,1}x} + B_1^1 e^{r_{1,2}x} + P_{\text{blood}}. \end{aligned}$$

We have $r_{0,1} = \frac{u_0 l_0}{D}$, $r_{1,1} = \frac{l_1}{2D}\left(u_1 + \sqrt{u_1^2 + 4\beta_1 D}\right)$ and $r_{1,2} = \frac{l_1}{2D}\left(u_1^2 - \sqrt{u_1 + 4\beta_1 D}\right)$.

The coefficients are

$$\begin{cases} B_0^1 = \dfrac{(P_{\text{air}} - P_{\text{blood}})(-r_{0,1}e^{r_{0,1}}f + 2r_{1,1}e^{r_{0,1}}f + r_{0,1}e^{r_{0,1}}g - 2r_{1,2}e^{r_{0,1}}g)}{dM} \\ A_0^1 = \dfrac{(P_{\text{air}} - P_{\text{blood}})(-2r_{1,1}f + 2r_{1,2}g)}{dM} \\ B_1^1 = \dfrac{(P_{\text{air}} - P_{\text{blood}})r_{0,1}e^{r_{0,1}}g}{dM} \\ A_1^1 = \dfrac{(P_{\text{air}} - P_{\text{blood}})(-r_{0,1}e^{r_{0,1}}f)}{dM} \end{cases}$$

with

$$f = e^{r_{1,2}}\left(\frac{D}{l_1}r_{1,2} + \alpha k\varrho_s\right),\ g = e^{r_{1,1}}\left(\frac{D}{l_1}r_{1,1} + \alpha k\varrho_s\right),$$

and

$$dM^1 = f\left(-r_{0,1}e^{r_{0,1}} - 2r_{1,1} + 2r_{1,1}e^{r_{0,1}}\right) + g\left(r_{0,1}e^{r_{0,1}} + 2r_{1,2} - 2r_{1,2}e^{r_{0,1}}\right).$$

Let us now focus on the continuity relatively to u_i in $u_i = 0$. We know that the solution in the first generation when $u_i \neq 0$ is,

$$P_0^1(x) = A_0^1 e^{r_{0,1}x} + B_0^1 + P_{\text{blood}}.$$

We want to observe this solution when $u_i \to 0$. We then have $r_{0,1} \to 0$ when $u_i \to 0$ and since $x \in [0,1]$ we have

$$|r_{0,1}x| < |r_{0,1}| \xrightarrow[u_i \to 0]{} 0$$

. The development in series of the exponential is then possible. We obtain

$$P_0^1(x) \approx A_0^1(1 + r_{0,1}x) + B_0^1 + P_{\text{blood}} = A_0^1 + B_0^1 + P_{\text{blood}} + A_0^1 r_{0,1}x.$$

Let us prove that this solution tends when $u_i \to 0$ to the following solution ,

$$P_0^0(x) = A_0^0 x + B_0^0.$$

We have

$$\begin{aligned} A_0^1 + B_0^1 + P_{\text{blood}} =& P_{\text{blood}} + (P_{\text{air}} - P_{\text{blood}})\times \\ & \frac{e^{r_{0,1}}\left(2r_{1,1}f - r_{0,1}f + r_{0,1}g - 2r_{1,2}g\right) - 2r_{1,1}f + 2r_{1,2}g}{dM^1} \\ =& P_{\text{air}} - P_{\text{blood}} + P_{\text{blood}} = P_{\text{air}} = B_0^0. \end{aligned}$$

Let us now compute

$$A_0^1 r_{0,1} = \frac{(P_{\text{air}} - P_{\text{blood}})(-2r_{1,1}f + 2r_{1,2}g)r_{0,1}}{dM^1}.$$

We have

$$\begin{aligned} \frac{dM^1}{r_{0,1}} &= -e^{r_{0,1}}f - \frac{2r_{1,1}}{r_{0,1}}f + \frac{2r_{1,1}e^{r_{0,1}}f}{r_{0,1}} + e^{r_{0,1}}g + \frac{2r_{1,2}}{r_{0,1}}g - \frac{2r_{1,2}e^{r_{0,1}}g}{r_{0,1}} \\ &= -f\left(e^{r_{0,1}} - 2r_{1,1}\left(\frac{e^{r_{0,1}}-1}{r_{0,1}}\right)\right) + g\left(e^{r_{0,1}} - 2r_{1,2}\left(\frac{e^{r_{0,1}}-1}{r_{0,1}}\right)\right). \end{aligned}$$

We know that $r_{0,1} \underset{u_i \to 0}{\longrightarrow} 0$, it implies that we have $e^{r_{0,1}} \underset{u_i \to 0}{\longrightarrow} 1 + r_{0,1}$. We can deduce that $\dfrac{e^{r_{0,1}}-1}{r_{0,1}} \underset{u_i \to 0}{\longrightarrow} 1$. Finally we obtain,

$$A_0^1 r_{0,1} \underset{u_i \to 0}{\longrightarrow} \frac{(P_{\text{air}} - P_{\text{blood}})(-2r_{1,1}f + 2r_{1,2}g)}{-f\left(e^{r_{0,1}} - 2r_{1,1}\right) + g\left(e^{r_{0,1}} - 2r_{1,2}\right)}.$$

Futhermore we know that $f \underset{u_i \to 0}{\longrightarrow} e^{-r}\left(-\frac{D}{l_1}r + \alpha k \varrho_s\right)$, $g \underset{u_i \to 0}{\longrightarrow} e^{r}\left(\frac{D}{l_1}r + \alpha k \varrho_s\right)$, $r_{1,1} \underset{u_i \to 0}{\longrightarrow} r$ and $r_{1,2} \underset{u_i \to 0}{\longrightarrow} -r$. We obtain,

$$A_0^1 r_{0,1} \underset{u_i \to 0}{\longrightarrow} \frac{(P_{\text{air}} - P_{\text{blood}})\left(-2re^{-r}\left(-\frac{D}{l_1}r + \alpha k \varrho_s\right) - 2re^{r}\left(\frac{D}{l_1}r + \alpha k \varrho_s\right)\right)}{dM^0} = A_0^0.$$

We proved that the solution in the bronchial tree is continuous relatively to u_i in $u_i = 0$. Let us now prove it in the acinus.

When $u_i \neq 0$, we have the following solution,

$$P_1^1(x) = A_1^1 e^{r_{1,1}x} + B_1^1 e^{r_{1,2}x} + P_{\text{blood}}.$$

And when $u_i = 0$, we have,

$$P_1^0(x) = A_1^0 e^{rx} + B_1^0 e^{-rx} + P_{\text{blood}}.$$

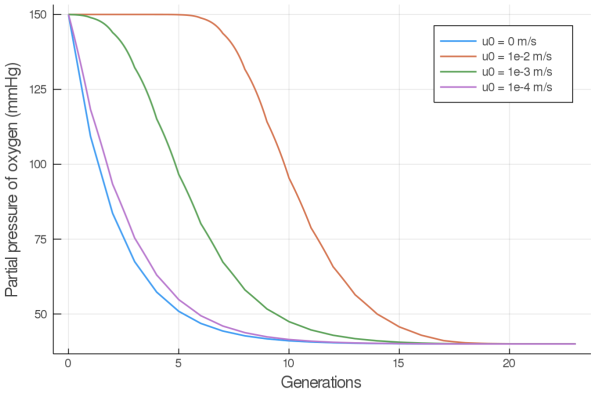

Figure 3.4: Partial pressure of the oxygen in the lung for different velocity.

Since we know that $r_{1,1} \underset{u_i \to 0}{\longrightarrow} r$ and $r_{1,2} \underset{u_i \to 0}{\longrightarrow} -r$ We then want to prove that $A_1^1 \underset{u_i \to 0}{\longrightarrow} A_1^0$ and that $B_1^1 \underset{u_i \to 0}{\longrightarrow} B_1^0$.

Let us first focus on A_1^1, we have,

$$A_1^1 = \frac{(P_{\text{air}} - P_{\text{blood}})(-r_{0,1} e^{r_{0,1}} f)}{dM^1}.$$

We computed previously,

$$\frac{dM^1}{r_{0,1}} \underset{u_i \to 0}{\longrightarrow} dM^0.$$

We then have,

$$A_1^1 \underset{u_i \to 0}{\longrightarrow} -\frac{(P_{\text{air}} - P_{\text{blood}}) e^{-r} \left(-\frac{D}{l_1} r + \alpha k \varrho_s\right)}{dM^0} = A_1^0.$$

Likewise, we have

$$B_1^1 = \frac{(P_{\text{air}} - P_{\text{blood}}) r_{0,1} e^{r_{0,1}} g}{dM^1}$$
$$B_1^1 \underset{u_i \to 0}{\longrightarrow} \frac{(P_{\text{air}} - P_{\text{blood}}) e^{r} \left(\frac{D}{l_1} r + \alpha k \varrho_s\right)}{dM^0} = B_1^0.$$

We proved for two generations the continuity of the solution relatively to u_i. This continuity can be extended to more generations. We can observe the continuity relatively to u_i in $u_i = 0$ numerically on Figure 3.2.1 for 23 generations.

We proved the uniform continuity relatively to u_i of the explicit solution, *i.e.* for all $x \in [0, 1]$, we have

$$P_i^1(x) \underset{u_i \to 0}{\longrightarrow} P_i^0(x).$$

$\square$

3.2.2 Physical analysis of the transport

Now that we have obtained our stationnary explicit solutions, let us observe if it is a good enough approximation of the general solution in the case of the lung. Let's start by adimensionaling the equation (3.7). The space was already adimensionalized previously for simplicity. However we still have to adimensionalize the time. Let us define the dimensionless time as $s = \frac{t}{\tilde{T}}$ where we chose $\tilde{T} = 0.1$ s. We obtain,

$$\frac{1}{\tilde{T}}\frac{\partial \tilde{P}_i}{\partial s} - \frac{D}{l_i^2}\frac{\partial^2 \tilde{P}_i}{\partial x^2} + \frac{u_i(s\tilde{T})}{l_i}\frac{\partial \tilde{P}_i}{\partial x} + \beta_i(\tilde{P}_i - P_{\text{blood}}) = 0,$$

or also,

$$\lambda_i\frac{\partial \tilde{P}_i}{\partial s} - \frac{\partial^2 \tilde{P}_i}{\partial x^2} + Pe_i\frac{\partial \tilde{P}_i}{\partial x} + \zeta_i(\tilde{P}_i - P_{\text{blood}}) = 0,$$

where,

$$\lambda_i = \frac{l_i^2}{D\tilde{T}} \quad Pe_i = \frac{l_i u_i}{D} \quad \zeta_i = \frac{\beta_i l_i^2}{D}.$$

λ_i represents the relative amplitude of the transitory effects and of the diffusion; the Peclet number Pe_i represents the relative amplitude of the convection by air and of the diffusion; and ζ_i represents the relative amplitude of the gas capture by blood and of diffusion and is meaningful only in the acini. These numbers are plotted on Figure 3.5.

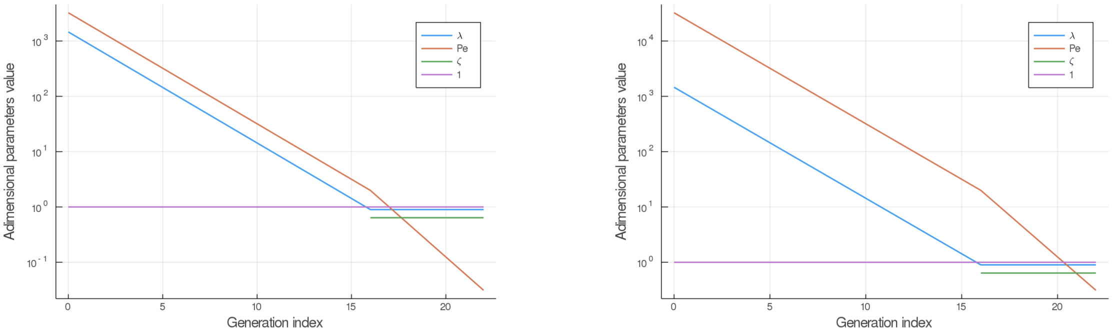

Figure 3.5: Dimensionless numbers at rest (left) and exercise (right). Results for oxygen. The case of carbon dioxide is very similar as diffusion coefficients of oxygen and carbon dioxide are similar. λ is the relative amplitude of the transitory effects and of the diffusion; Peclet number Pe is the relative amplitude of the convection and of the diffusion; ζ is the relative amplitude of the gas capture by blood and of diffusion. The variable $\tilde{T}$ is chosen to be 0.1 s.

These numbers gives us interesting insights on the behavior of gas transport. We can observe on Figure 3.5 that at rest, convection is dominant in the whole conductive tree. However transitory effects are only slightly smaller than convection effects, they are of the same order. Interestingly, in the acini, transport by diffusion, transitory effects and absorption by blood are of similar. It results the geometrical properties of the acini. At exercise, convection is dominant on every other phenomena down to the last quarter of the acini, where diffusion, transitory effects and absorption by blood become dominant, with similar amplitude.

We can deduce that at rest the stationnary solution is not a good approximation in the case of the lung because the two coefficient λ and Pe are of the same order. But during exercise, we could approximate the general solution by its stationnary one in the convective tree, when the air velocity is sufficiently large, for example when it is at its highest in a respiratory cycle which corresponds to the inspiration peak.

3.2.3 General Case

In the following, we will work with the non stationnary equation. Let us study some of its properties such as the existence of an unique solution.

Equations in the complete space domain

The equations (3.7) are defined for each generations $i \in [\![0, N]\!]$, where $N+1$ is the number of generations in the lung. We want to rewrite it so we have an unique equation for the whole tree.

The first step is to change the space variable in order to have each equation for each generation on a different space domain (see Figure 3.6).

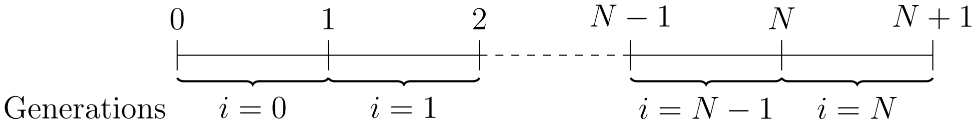

Figure 3.6: Organization of the new space domains.

The new space variable is defined for each generation i as follow,

$$\hat{x} = x + i.$$

Then we have $\hat{P}_i(t, \hat{x}) = P_i(t, x)$ that verifies,

$$\frac{\partial \hat{P}_i}{\partial t} - \frac{D}{l_i^2}\frac{\partial^2 \hat{P}_i}{\partial \hat{x}^2} + \frac{u_i(t)}{l_i}\frac{\partial \hat{P}_i}{\partial \hat{x}} + \beta_i\left(\hat{P}_i - P_{\text{blood}}\right) = 0 \quad \text{for } \hat{x} \in [i, i+1]. \tag{3.9}$$

Now let us make a second change in the space variable, but only in the acinus. We want to extend our space domain in order to remove the non boundary terms coming from the conditions at the bifurcations in the variational formulation of the equation on the space domain for the whole lung. Indeed, to prove the existence of a solution we require to only have boundary conditions at the inlet and at the outlets of the tree. We know that in the acinus the length of the bronchi are the same in all generations and that the velocity decreases as follow,

$$u_{i+1} = \frac{u_i}{2}.$$

To compensate this decrease in velocity, we look for functions $s_i(\hat{x})$ such that,

$$s_i'(\hat{x})u_i = s_{i+1}'(\hat{x})u_{i+1},$$

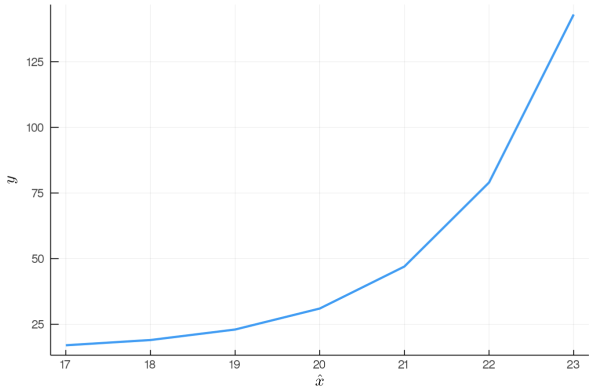

Figure 3.7: Function s_i representing the change in space variable in the acinus ($i \in [\![G, N]\!]$)

which implies for $\hat{x} \in [i, i+1]$,

$$2s_i'(\hat{x}) = s_{i+1}'(\hat{x}).$$

We also want the space domains to be connected, which implies for $i \in [\![G, N]\!]$ where G is the number of generations in the bronchial tree,

$$\begin{cases} s_G(G) = G, \\ s_{i+1}(i+1) = s_i(i+1). \end{cases}$$

So for all $i \in [\![G, N]\!]$, and for $j = i - G + 1$, the function s_i (see Figure 3.7) writes,

$$y = s_i(\hat{x}) = 2^j \hat{x} + (1 - 2^j)G + \sum_{k=1}^{j} 2^k - 2^j j, \quad \text{for } \hat{x} \in [i, i+1]. \tag{3.10}$$

Then we have $\tilde{P}_i(t, y) = \hat{P}_i(t, \hat{x})$ and $\mathrm{d}y = 2^j \mathrm{d}\hat{x}$. Finally we can rewrite the equation (3.9) in the acinus for the generations $i \in [\![G, N]\!]$,

$$\frac{\partial \tilde{P}_i}{\partial t} - \frac{2^{2j} D}{l_i^2} \frac{\partial^2 \tilde{P}_i}{\partial y^2} + \frac{2^j u_i(t)}{l_i} \frac{\partial \tilde{P}_i}{\partial y} + \beta_i \tilde{P}_i = \beta_i P_{\text{blood}}, \quad \forall y \in [k_{i,1}, k_{i,2}],$$

where the bounds of our domains are,

$$k_{i,1} = 2^j i + (1 - 2^j)G + \sum_{k=1}^{j} 2^k - 2^j j,$$

and

$$k_{i,2} = 2^j (i+1) + (1 - 2^j)G + \sum_{k=1}^{j} 2^k - 2^j j.$$

Let us now define our complete space domain Ω,

$$\Omega = \bigcup_{i=0}^{N} [k_{i,1}, k_{i,2}] = [0, k_{N,2}].$$

where we have in the convective tree ($i \in [\![0, G-1]\!]$),

$$[k_{i,1}, k_{i,2}] = [i, i+1].$$

Then, the function $\tilde{P}$ defined on Ω verifies the following equation,

$$\frac{\partial \tilde{P}}{\partial t} - \theta_1(y)\frac{\partial^2 \tilde{P}}{\partial y^2} + \theta_2(t,y)\frac{\partial \tilde{P}}{\partial y} + \theta_3(y)\tilde{P} = \tilde{f}(y), \ \ \forall y \in \Omega, \tag{3.11}$$

where,

$$\theta_1(y) = \sum_{i=0}^{G-1} \frac{D}{l_i^2}\mathbf{1}_{[k_{i,1},k_{i,2}[}(y) + \sum_{i=G}^{N} \frac{2^{2(i-G+1)}D}{l_i^2}\mathbf{1}_{[k_{i,1},k_{i,2}[}(y),$$

$$\theta_2(t,y) = \sum_{i=0}^{G-1} \frac{u_i(t)}{l_i}\mathbf{1}_{[k_{i,1},k_{i,2}[}(y) + \sum_{i=G}^{N} \frac{2^{i-G+1}u_i(t)}{l_i}\mathbf{1}_{[k_{i,1},k_{i,2}[}(y),$$

$$\theta_3(y) = \sum_{i=0}^{N} \beta_i \mathbf{1}_{[k_{i,1},k_{i,2}[}(y),$$

and,

$$\tilde{f}(y) = \sum_{i=0}^{N} \beta_i P_{\text{blood}} \mathbf{1}_{[k_{i,1},k_{i,2}[}(y).$$

This equation is completed with the following boundary conditions,

$$\tilde{P}(t,0) = P_{\text{air}},$$

$$-\frac{2^{N-G+1}D}{l_N}\frac{\partial \tilde{P}}{\partial y}(t, k_{N,2}) = \alpha k \varrho_s(\tilde{P}(t,k_{N,2}) - P_{\text{blood}}),$$

and with the following bifurcations conditions in the convective tree,

$$-\frac{D}{l_i}\frac{\partial \tilde{P}(t,k_{i,2})}{\partial y} = -\frac{2Dh^2}{l_{i+1}}\frac{\partial \tilde{P}(t,k_{i+1,1})}{\partial y}, \tag{3.12}$$

and in the acinus,

$$-\frac{D}{l_i}\frac{\partial \tilde{P}(t,k_{i,2})}{\partial y} = -\frac{4D}{l_{i+1}}\frac{\partial \tilde{P}(t,k_{i+1,1})}{\partial y}. \tag{3.13}$$

Homogeneous boundary condition in $y = 0$

Let us define a function $r(y)$ in order for our boundary condition at the entrance of the tree to be homogenous. It is defined such that the function

$$Q(t, y) = \tilde{P}(t, y) - r(y),$$

verifies the following conditions at the inlet and at the outlets of the tree,

$$\begin{cases} Q(t, 0) = 0, \\ -\dfrac{2^{N-G+1} D}{l_N} \dfrac{\partial Q(t, k_{N,2})}{\partial y} = \alpha k \varrho_s Q(t, k_{N,2}). \end{cases} \tag{3.14}$$

The function r is defined as a sum of affine functions,

$$r(y) = \sum_{i=0}^{N} r_i(y) \mathbf{1}_{[k_{i,1}, k_{i,2}]},$$

where $r_i(y) = A_i y + B_i$ for each generation $i \in [\![0, N]\!]$. We suppose that the functions r_i satisfy the same properties as the function $\tilde{P}$ at the boundaries of the domain and at the bifurcations. Then, the function r satisfies at the inlet and at the outlets of the tree,

$$\begin{cases} r(0) = P_{\text{air}} \\ -\dfrac{2^{N-G+1} D}{l_N} \dfrac{\partial r(k_{N,2})}{\partial y} = \alpha k \varrho_s (r(k_{N,2}) - P_{\text{blood}}). \end{cases}$$

The functions r_i satisfy the following equations at the bifurcations in the convective tree,

$$\begin{cases} r_i(k_{i,2}) = r_{i+1}(k_{i+1,1}) \\ -\dfrac{D}{l_i} \dfrac{\partial r_i(k_{i,2})}{\partial y} = -\dfrac{2Dh^2}{l_{i+1}} \dfrac{\partial r_{i+1}(k_{i+1,1})}{\partial y} \end{cases},$$

and in the acinus,

$$\begin{cases} r_i(k_{i,2}) = r_{i+1}(k_{i+1,1}) \\ -\dfrac{D}{l_i} \dfrac{\partial r_i(k_{i,2})}{\partial y} = -\dfrac{4D}{l_{i+1}} \dfrac{\partial r_{i+1}(k_{i+1,1})}{\partial y} \end{cases}.$$

Thanks to the existence of this function r, we can now rewrite the equation (3.11),

$$\frac{\partial Q}{\partial t} - \theta_1(y) \frac{\partial^2 Q}{\partial y^2} + \theta_2(t, y) \frac{\partial Q}{\partial y} + \theta_3(y) Q = f(t, y), \tag{3.15}$$

where $f(t, y) = \tilde{f}(y) + \theta_1(y) \frac{\partial^2 r}{\partial y^2} - \theta_2(t, y) \frac{\partial r}{\partial y} - \theta_3(y) r(y) \in H^{-1}(\Omega)$.

The bifurcation conditions remains the same, but the boundary conditions are now those in equation (3.14).

Variationnal formulation

We start our analysis by computing the variational formulation of the equation (3.15).

Proposition 3.2.2 (Variationnal formulation)**.** *Let us define* $V_0 = \{v \in H^1(\Omega), v(0) = 0\}$*. The variationnal formulation of our model writes,*

$$\forall \Psi \in V_0, \int_\Omega \frac{\partial Q}{\partial t} \Psi \, dy + a(Q, \Psi) = \int_\Omega f(t, x) \Psi \, dy, \tag{3.16}$$

where,

$$\begin{aligned} a(Q, \Psi) = \int_\Omega \theta_1(y) \frac{\partial Q}{\partial y} \frac{\partial \Psi}{\partial y} \, dy + \theta_2(t) \int_\Omega \frac{\partial Q}{\partial y} \Psi \, dy + \int_\Omega \theta_3(y) Q \Psi \, dy \\ + \frac{2^{N-G+1} \alpha k \varrho_s}{l_N} Q(t, k_{N,2}) \Psi(k_{N,2}), \end{aligned} .$$

Proof. We multiply our equation (3.15) by a test function $\Psi \in V_0$ and we integrate over the domain Ω,

$$\begin{aligned} \int_\Omega \frac{\partial Q}{\partial t} \Psi dy - \int_\Omega \theta_1(y) \frac{\partial^2 Q}{\partial y^2} \Psi dy + \theta_2(t, y) \int_\Omega \frac{\partial Q}{\partial y} \Psi dy + \int_\Omega \theta_3(y) Q \Psi dy \\ = \int_\Omega f \Psi dy. \end{aligned}$$

First, let us take a look at the function $\theta_2(t, y)$.

Analysis of the function $\theta_2(t, y)$.

We know that,

$$\frac{u_{i+1}(t)}{l_{i+1}} = \frac{u_i(t)}{l_i} \frac{1}{2h^3}.$$

In the convective tree, we have $h = 2^{-1/3}$, we can deduce that,

$$\frac{u_{i+1}(t)}{l_{i+1}} = \frac{u_i(t)}{l_i}.$$

And in the acinus, we have $h = 1$, so we obtain,

$$\frac{u_{i+1}(t)}{l_{i+1}} = \frac{u_i(t)}{2l_i}.$$

It means that for $i \in [\![G, N]\!]$, we have

$$\frac{2^{i-G+2} u_{i+1}(t)}{l_{i+1}} = \frac{2^{i-G+1} u_i(t)}{l_i}.$$

The function θ_2 is then a constant regarding space, it writes

$$\theta_2(t, y) = \theta_2(t) = \frac{u_0(t)}{l_0}.$$

We now want to compute the following part,

$$I = -\int_{\Omega} \theta_1(y) \frac{\partial^2 Q}{\partial y^2} \Psi dy.$$

In order to compute it, we split it on the intermediate domains and obtain,

$$\begin{aligned}
I &= -\sum_{i=0}^{N} \int_{k_{i,1}}^{k_{i,2}} \theta_1(y) \frac{\partial^2 Q}{\partial y^2} \Psi dy \\
&= -\sum_{i=0}^{G-1} \frac{D}{l_i^2} \int_{k_{i,1}}^{k_{i,2}} \frac{\partial^2 Q}{\partial y^2} \Psi dy - \sum_{i=G}^{N} \frac{2^{2(i-G+1)} D}{l_i^2} \int_{k_{i,1}}^{k_{i,2}} \frac{\partial^2 Q}{\partial y^2} \Psi dy \\
&= \sum_{i=0}^{G-1} \frac{D}{l_i^2} \int_{k_{i,1}}^{k_{i,2}} \frac{\partial Q}{\partial y} \frac{\partial \Psi}{\partial y} dy + \sum_{i=G}^{N} \frac{2^{2(i-G+1)} D}{l_i^2} \int_{k_{i,1}}^{k_{i,2}} \frac{\partial Q}{\partial y} \frac{\partial \Psi}{\partial y} dy \\
&\quad - \sum_{i=0}^{G-1} \left[\frac{D}{l_i^2} \frac{\partial Q}{\partial y} \Psi \right]_{k_{i,1}}^{k_{i,2}} - \sum_{i=G}^{N} \left[\frac{2^{2(i-G+1)} D}{l_i^2} \frac{\partial Q}{\partial y} \Psi \right]_{k_{i,1}}^{k_{i,2}} \\
&= \int_{\Omega} \theta_1(y) \frac{\partial Q}{\partial y} \frac{\partial \Psi}{\partial y} dy + \theta_4,
\end{aligned}$$

where θ_4 is defined as follow,

$$\theta_4 = \underbrace{-\sum_{i=0}^{G-1} \left[\frac{D}{l_i^2} \frac{\partial Q}{\partial y} \Psi \right]_{k_{i,1}}^{k_{i,2}}}_{\theta_{4,1}} \underbrace{-\sum_{i=G}^{N} \left[\frac{2^{2(i-G+1)} D}{l_i^2} \frac{\partial Q}{\partial y} \Psi \right]_{k_{i,1}}^{k_{i,2}}}_{\theta_{4,2}}.$$

To compute it, let's start by studying the first term.

Analysis of $\theta_{4,1}$.

We have,

$$\theta_{4,1} = -\sum_{i=0}^{G-1} \left[\frac{D}{l_i^2} \frac{\partial Q}{\partial y} \Psi \right]_{k_{i,1}}^{k_{i,2}}.$$

$$\begin{aligned}
\theta_{4,1} &= \sum_{i=0}^{G-1} \frac{D}{l_i^2} \left(\frac{\partial Q(t, k_{i,1})}{\partial y} \Psi(k_{i,1}) - \frac{\partial Q(t, k_{i,2})}{\partial y} \Psi(k_{i,2}) \right) \\
&= \frac{D}{l_0^2} \frac{\partial Q(t,0)}{\partial y} \Psi(0) + \sum_{i=0}^{G-2} \left(\frac{D}{l_{i+1}^2} \frac{\partial Q(t, k_{i+1,1})}{\partial y} - \frac{D}{l_i^2} \frac{\partial Q(t, k_{i,2})}{\partial y} \right) \Psi(k_{i,2}) \\
&\quad - \frac{D}{l_{G-1}^2} \frac{\partial Q(t, k_{G-1,2})}{\partial y} \Psi(k_{G-1,2}).
\end{aligned}$$

We know that $\Psi(0) = 0$ because $\Psi \in V_0$. Furthermore we know that,

$$-\frac{D}{l_i} \frac{\partial Q(t, k_{i,2})}{\partial y} = -\frac{2Dh^2}{l_{i+1}} \frac{\partial Q(t, k_{i+1,1})}{\partial y}.$$

If we divide the last equation by l_i which is equals to $\frac{l_{i+1}}{h}$, we obtain,

$$\frac{2Dh^3}{l_{i+1}^2}\frac{\partial Q(t,k_{i+1,1})}{\partial y}-\frac{D}{l_i^2}\frac{\partial Q(t,k_{i,2})}{\partial y}=0.$$

Yet in the bronchial tree when $i\in[\![0,G-1]\!]$, we know that $h=\left(\frac{1}{2}\right)^{1/3}$. We obtain,

$$\frac{D}{l_{i+1}^2}\frac{\partial Q(t,k_{i+1,1})}{\partial y}-\frac{D}{l_i^2}\frac{\partial Q(t,k_{i,2})}{\partial y}=0.$$

It implies that,

$$\theta_{4,1}=-\frac{D}{l_{G-1}^2}\frac{\partial Q(t,k_{G-1,2})}{\partial y}\Psi(k_{G-1,2}).$$

Now, let us focus on the second term of θ_4.

<u>Analysis of $\theta_{4,2}$.</u>
We obtain,

$$\begin{aligned}\theta_{4,2}=&-\sum_{i=G}^{N}\left[\frac{2^{2(i-G+1)}D}{l_i^2}\frac{\partial Q}{\partial y}\Psi\right]_{k_{i,1}}^{k_{i,2}}\\
=&\sum_{i=G}^{N}\frac{2^{2(i-G+1)}D}{l_i^2}\left(\frac{\partial Q(t,k_{i,1})}{\partial y}\Psi(k_{i,1})-\frac{\partial Q(t,k_{i,2})}{\partial y}\Psi(k_{i,2})\right)\\
=&\sum_{i=G}^{N-1}\left(\frac{2^{2(i-G+2)}D}{l_{i+1}^2}\frac{\partial Q(t,k_{i+1,1})}{\partial y}-\frac{2^{2(i-G+1)}D}{l_i^2}\frac{\partial Q(t,k_{i,2})}{\partial y}\right)\Psi(k_{i,2})\\
&+\frac{4D}{l_G^2}\frac{\partial Q}{\partial y}(t,k_{G,1})\Psi(k_{G,1})-\frac{2^{2(N-G+1)}D}{l_N^2}\frac{\partial Q}{\partial y}(t,k_{N,2})\Psi(k_{N,2}).\end{aligned}$$

But we know that,

$$-\frac{D}{l_i}\frac{\partial Q(t,k_{i,2})}{\partial y}=-\frac{4D}{l_{i+1}}\frac{\partial Q(t,k_{i+1,1})}{\partial y}.$$

Since $l_i=l_{i+1}$, we have,

$$\begin{aligned}&\frac{2^{2(i-G+2)}D}{l_{i+1}^2}\frac{\partial Q(t,k_{i+1,1})}{\partial y}-\frac{2^{2(i-G+1)}D}{l_i^2}\frac{\partial Q(t,k_{i,2})}{\partial y}\\
&=\frac{2^{2(i-G+1)}D}{l_{i+1}^2}\left(4\frac{\partial Q(t,k_{i+1,1})}{\partial y}-\frac{\partial Q(t,k_{i,2})}{\partial y}\right)\\
&=0.\end{aligned}$$

We can deduce that,

$$\theta_{4,2}=\frac{4D}{l_G^2}\frac{\partial Q}{\partial y}(t,k_{G,1})\Psi(k_{G,1})-\frac{D2^{2(N-G+1)}}{l_N^2}\frac{\partial Q}{\partial y}(t,k_{N,2})\Psi(k_{N,2})$$

Finally, thanks to the computations of $\theta_{4,1}$ and $\theta_{4,2}$ we can deduce the value for θ_4.

Analysis of θ_4.
We obtain,

$$\begin{aligned}\theta_4 =& \theta_{4,1}+\theta_{4,2}\\ =& -\frac{D}{l_{G-1}^2}\frac{\partial Q}{\partial y}(t,k_{G-1,2})\Psi(k_{G-1,2})+\frac{4D}{l_G^2}\frac{\partial Q}{\partial y}(t,k_{G,1})\Psi(k_{G,1})\\ &-\frac{D2^{2(N-G+1)}}{l_N^2}\frac{\partial Q}{\partial y}(t,k_{N,2})\Psi(k_{N,2})\end{aligned}$$

We know that,

$$-\frac{D}{l_{G-1}}\frac{\partial Q(t,k_{G-1,2})}{\partial y}=-\frac{4D}{l_G}\frac{\partial Q(t,k_{G,1})}{\partial y},$$

and that $l_G = l_{G-1}$. It results in

$$\theta_4=-\frac{D2^{2(N-G+1)}}{l_N^2}\frac{\partial Q}{\partial y}(t,k_{N,2})\Psi(k_{N,2}).$$

Or, thanks to the boundary condition,

$$\theta_4=\frac{2^{N-G+1}\alpha k\varrho_s}{l_N}Q(t,k_{N,2})\Psi(k_{N,2}).$$

We finally obtain the following variationnal formulation, $\forall\Psi\in V_0$,

$$\begin{aligned}\int_\Omega \frac{\partial Q}{\partial t}\Psi\,dy+\int_\Omega\theta_1(y)\frac{\partial Q}{\partial y}\frac{\partial \Psi}{\partial y}\,dy+\theta_2(t)\int_\Omega\frac{\partial Q}{\partial y}\Psi\,dy+\int_\Omega\theta_3(y)Q\Psi\,dy\\ +\frac{2^{N-G+1}\alpha k\varrho_s}{l_N}Q(t,k_{N,2})\Psi(k_{N,2})=\int_\Omega f\Psi\,dy.\end{aligned}$$

□

Gårding Coercivity

Now, we will focus on the bilinear form $a(Q,\Psi)$. We will prove that it is Gårding coercive. It will be useful in the following in order to prove the existence of a unique solution to our equation (3.15).

Theorem 3.2.3. *The bilinear form,*

$$\begin{aligned}a(Q,\Psi)=\int_\Omega\theta_1(y)\frac{\partial Q}{\partial y}\frac{\partial \Psi}{\partial y}\,dy+\theta_2(t)\int_\Omega\frac{\partial Q}{\partial y}\Psi\,dy+\int_\Omega\theta_3(y)Q\Psi\,dy\\ +\frac{2^{N-G+1}\alpha k\varrho_s}{l_N}Q(t,k_{N,2})\Psi(k_{N,2}),\end{aligned}$$

is Gårding coercive. It means that $\forall Q\in V_0$,

$$a(Q,Q)\geqslant C_1\left\|Q\right\|^2_{H^1(\Omega)}-C_2\left\|Q\right\|^2_{L^2(\Omega)},$$

where $C_1>0$ *and* C_2 *are constants.*

Proof. To start let us split our bilinear form a in two parts. Let us define $\forall Q, \Psi \in V_0$:

$$a_1(Q,\Psi) = \int_\Omega \theta_1(y) \frac{\partial Q}{\partial y} \frac{\partial \Psi}{\partial y} \, dy + \int_\Omega \theta_3(y) Q \Psi \, dx + \frac{2^{N-G+1} \alpha k \varrho_s}{l_N} Q(k_{N,2}) \Psi(k_{N,2}),$$

and,

$$a_2(Q,\Psi) = \theta_2(t) \int_\Omega \frac{\partial Q}{\partial y} \Psi \, dy.$$

We have,

$$a(Q,\Psi) = a_1(Q,\Psi) + a_2(Q,\Psi).$$

Let us start by analyzing the symmetric bilinear form a_1.

Analysis of $a_1(Q,Q)$.

We want to prove that the symmetric bilinear form a_1 is H^1 coercive. We know that $\alpha k \varrho_s \geqslant 0$, then,

$$a_1(Q,Q) \geqslant \int_\Omega \theta_1(y) \left(\frac{\partial Q}{\partial y} \right)^2 dy + \int_\Omega \theta_3(y) Q^2 \, dy.$$

Furthermore we know that the functions $\theta_1 > 0$ and $\theta_3 \geqslant 0$ are bounded. We can write that,

$$a_1(Q,Q) \geqslant \min(\theta_1) \left\| \frac{\partial Q}{\partial y} \right\|^2_{L^2(\Omega)} + \min(\theta_3) \left\| Q \right\|^2_{L^2(\Omega)} .$$

We know that the minimum of the function θ_3 is 0, then,

$$a_1(Q,Q) \geqslant \min(\theta_1) \left\| \frac{\partial Q}{\partial y} \right\|^2_{L^2(\Omega)} = \frac{\min(\theta_1)}{2} \left(\left\| \frac{\partial Q}{\partial y} \right\|^2_{L^2(\Omega)} + \left\| \frac{\partial Q}{\partial y} \right\|^2_{L^2(\Omega)} \right)$$

Let us use the Poincaré inequality since we have $Q(0) = 0$. We obtain,

$$a_1(Q,Q) \geqslant \frac{\min(\theta_1)}{2} \left(\left\| \frac{\partial Q}{\partial y} \right\|^2_{L^2(\Omega)} + C \left\| Q \right\|^2_{L^2(\Omega)} \right),$$

where $C > 0$ is a constant. Thus we have,

$$\begin{aligned} a_1(Q,Q) &\geqslant \frac{\min(\theta_1 C, \theta_1)}{2} \left(\left\| \frac{\partial Q}{\partial y} \right\|^2_{L^2(\Omega)} + \left\| Q \right\|^2_{L^2(\Omega)} \right) \\ &\geqslant \frac{\min(\theta_1 C, \theta_1)}{2} \left\| Q \right\|^2_{H^1(\Omega)} \end{aligned}$$

The coefficient $\eta_1 = \frac{\min(\theta_1 C, \theta_1)}{2} > 0$ is a constant. We proved that a_1 is H^1-coercive.

Let us now focus on $a_2(Q,Q)$.

Analysis of $a_2(Q,Q)$.
The function $\theta_2(t)$ is bounded, hence,

$$-\left\|\theta_2\right\|_{L^\infty(\mathbb{R}^+)} \leqslant \theta_2(t) \leqslant \left\|\theta_2\right\|_{L^\infty(\mathbb{R}^+)}.$$

We can deduce thanks to the Cauchy-Schwarz inequality,

$$a_2(Q,\Psi) \geqslant -\left\|\theta_2\right\|_{L^\infty(\mathbb{R}^+)} \left\|\frac{\partial Q}{\partial y}\right\|_{L^2(\Omega)} \left\|Q\right\|_{L^2(\Omega)}.$$

Finally, let us focus of the bilinear form $a(Q,Q)$.

Analysis of $a(Q,Q)$.
We obtain from the analyses of a_1 and a_2,

$$a(Q,Q) \geqslant \eta_1 \left\|Q\right\|^2_{H^1(\Omega)} - \left\|\theta_2\right\|_{L^\infty(\mathbb{R}^+)} \left\|\frac{\partial Q}{\partial y}\right\|_{L^2(\Omega)} \left\|Q\right\|_{L^2(\Omega)}$$

Let us define $\eta_2 = \left\|\theta_2\right\|_{L^\infty(\mathbb{R}^+)}$. We know that for all A, B, and $\kappa > 0$, we have $\left(\sqrt{\frac{\kappa}{2}}A - \frac{B}{\sqrt{2\kappa}}\right)^2 \geqslant 0$. By expanding this expression, we obtain

$$-AB \geqslant -\frac{\kappa}{2}A^2 - \frac{B^2}{2\kappa}.$$

Let us choose $A = \left\|\frac{\partial Q}{\partial y}\right\|_{L^2(\Omega)}$ and $B = \eta_2\|Q\|_{L^2(\Omega)}$. It results that,

$$\begin{aligned} a(Q,Q) &\geqslant \eta_1 \left\|Q\right\|^2_{H^1(\Omega)} - \frac{\kappa}{2}\left\|\frac{\partial Q}{\partial y}\right\|^2_{L^2(\Omega)} - \frac{\eta_2^2}{2\kappa}\|Q\|^2_{L^2(\Omega)} \\ &\geqslant \left(\eta_1 - \frac{\kappa}{2}\right)\left\|Q\right\|^2_{H^1(\Omega)} - \frac{\eta_2^2}{2\kappa}\|Q\|^2_{L^2(\Omega)} \end{aligned}$$

We can finally choose $\kappa = \eta_1 > 0$, and we obtain,

$$a(Q,Q) \geqslant \frac{\eta_1}{2}\left\|Q\right\|^2_{H^1(\Omega)} - \frac{\eta_2^2}{2\eta_1}\|Q\|^2_{L^2(\Omega)}$$

We proved that the quadratic form a is Gårding coercive, since $C_1 = \frac{\eta_1}{2} > 0$ and $C_2 = \frac{\eta_2^2}{2\eta_1}$ are constants.

□

Let us note that if our boundary conditions at the outlets of the tree were Dirichlet conditions, the quadratic form $a(Q,\Psi)$ would be coercive, *i.e.* it would satisfy the following property,

$$a(Q,Q) \geqslant C\left\|Q\right\|^2_{H^1(\Omega)},$$

where $C > 0$ is a constant.

Furthermore, if we assume that for all $t \geqslant 0$ we have $\alpha\varrho_s k + \frac{u_N(t)}{2} \geqslant 0$, then our quadratic form $a(Q,\Psi)$ would also be coercive [28] .

However, in our case the Gårding coercivity is sufficient to prove the existence and uniqueness of a solution.

Existence and uniqueness

In order to prove the existence and the uniqueness of a solution for our model, we need the theorem 3.2.4 de J.L. Lions. The proof of this theorem is detailed in [63].

Theorem 3.2.4 (J.L. Lions)**.** *Let H and V be two Hilbert spaces. We suppose that $V \subset H$ with a dense and continuous injection and with $V \subset H \subset V'$. Let us have a fixed $\Psi > 0$; for almost every $t \in [0,T]$, let us have a bilinear form $a(t;u,v) : V \times V \to \mathbb{R}$ that verify the following properties :*

1. *the function $t \mapsto a(t;u,v)$ is measurable $\forall u, v \in V$,*
2. *$|a(t;u,v)| \leqslant M\|u\|_V\|v\|_V$ a.e. $t \in [0,T]$, $\forall u, v \in V$*
3. *$a(t;u,u) \geqslant C_1\|u\|_V^2 - C_2\|u\|_H^2$ a.e. $t \in [0,T]\, \forall u \in V$,*

where $M, C_1 > 0$ and C_2 are constants. If we have $f \in L^2(0,T;V')$ and $u_0 \in H$, then there exists an unique function u such that

$$u \in L^2(0,T;V) \cap C([0,T];H) \qquad et \qquad \frac{du}{dt} \in L^2(0,T;V')$$

$$\begin{cases} \langle \frac{du}{dt}(t), v\rangle + a(t;u(t),v) = \langle f(t), v\rangle, & \forall v \in V \\ u(0) = u_0. \end{cases}$$

Theorem 3.2.5. *Let us define $T > 0$ fixed, $\Omega = [0, k_{N,2}]$ where $N \geqslant 1$ is an integer. Let us have $V_0 = \{v \in H^1(\Omega), v(0) = 0\}$. If we have $f \in H^{-1}(\Omega)$ and $Q^0 \in L^2(\Omega)$, then there exists an unique function Q such that,*

$$Q \in L^2(0,T;V_0) \cap C([0,T];L^2(\Omega)), \qquad \frac{dQ}{dt} \in L^2(0,T;H^{-1}(\Omega)).$$

and,

$$\begin{cases} \int_\Omega \frac{\partial Q}{\partial t}\Psi\, dy + a(Q,\Psi) = \int_\Omega f(t,y)\Psi\, dy, \\ Q(0,y) = Q^0(y). \end{cases} \tag{3.17}$$

Futhermore since we are in one dimension, the solution is also continuous in space.

Proof. First, let us prove that the injection of V_0 in $L^2(\Omega)$ is continuous and dense. We know that $\forall v \in H^1(\Omega)$, we have by definition :

$$\|v\|_{H^1}^2 = \|v\|_{L^2}^2 + \|v'\|_{L^2}^2.$$

Then we have,

$$\|v\|_{H^1}^2 \geqslant \|v\|_{L^2}^2,$$

or also,

$$\|v\|_{H^1} \geqslant \|v\|_{L^2}.$$

It proves that the injection is continuous.

Now, let us prove that the injection is dense. We know from Adams [1] that the space $C_0^\infty(\Omega)$ is dense in the space $L^2(\Omega)$. Furthermore

$$C_0^\infty(\Omega) \subset V_0 \subset H^1(\Omega),$$

we can deduce that V_0 and $H^1(\Omega)$ are dense in $L^2(\Omega)$.

Now we want to verify the properties of the quadraticform $a(Q,\Psi)$:

1. The function $t \mapsto a(Q,\Psi)$ is measurable for all $Q,\Psi \in V_0$ since the function $\theta_2(t)$ is continuous in time, hence measurable.
2. Let us define $\kappa_1 = \|\theta_1\|_{L^\infty(\Omega)}$, $\kappa_2 = \|\theta_2\|_{L^\infty([0,\Psi])}$, $\kappa_3 = \|\theta_3\|_{L^\infty(\Omega)}$ and $\kappa_4 = \frac{2^{N-G+1}\alpha k \varrho_s}{l_N}$.

   Let $Q \in V_0$ and $\Psi \in V_0$, we have,

   $$\begin{aligned}|a(Q,\Psi)| \leqslant \kappa_1 \left|\int_\Omega \frac{\partial Q}{\partial y}\frac{\partial \Psi}{\partial y}\,\mathrm{d}y\right| + \kappa_2 \left|\int_\Omega \frac{\partial Q}{\partial y}\Psi\,\mathrm{d}y\right| \\ + \kappa_3 \left|\int_\Omega Q\Psi\,\mathrm{d}y\right| + \kappa_4 Q(k_{N,2})\Psi(k_{N,2})\end{aligned}$$

   We obtain thanks to the Cauchy-Schwarz inequality,

   $$\begin{aligned}|a(Q,\Psi)| \leqslant \kappa_1 \left\|\frac{\partial Q}{\partial y}\right\|_{L^2(\Omega)} \left\|\frac{\partial \Psi}{\partial y}\right\|_{L^2(\Omega)} + \kappa_2 \left\|\frac{\partial Q}{\partial y}\right\|_{L^2(\Omega)} \|\Psi\|_{L^2(\Omega)} \\ + \kappa_3 \|Q\|_{L^2(\Omega)} \|\Psi\|_{L^2(\Omega)} + \kappa_4 Q(k_{N,2})\Psi(k_{N,2})\end{aligned}$$

   We can deduce by continuity of the trace,

   $$|a(Q,\Psi)| \leqslant (\kappa_1+\kappa_2+\kappa_3+\kappa_4 C)\,\|Q\|_{H^1(\Omega)}\,\|\Psi\|_{H^1(\Omega)}$$

   where C is a constant. We proved the continuity of the quadraticform $a(Q,\Psi)$ since $\kappa_1+\kappa_2+\kappa_3+\kappa_4 C$ is a constant.
3. Previously we proved that the quadraticform a is Gårding coercive.

We verified the three properties in order to apply the theorem 3.2.4. We proved the existence and uniqueness of the function Q. We proved that the solution is in $H^1(\Omega)$ and since we are in 1D in space we know that $H^1(\Omega) \subset C^0(\Omega)$. We can deduce that the solution is continuous in space.

□

We have proved the continuity of the solution in space, but we can go further on each bronchus. Indeed on each open domain $]k_{i,1}, k_{i,2}[$, we can prove that the solution is C^1. We know that we have,

$$\int_{k_{i,1}}^{k_{i,2}} \frac{D}{l_i^2}\frac{\partial^2 Q_i}{\partial y^2}\Psi dy = \int_{k_{i,1}}^{k_{i,2}} \left(\frac{\partial Q_i}{\partial t} + \frac{u_i(t)}{l_i}\frac{\partial Q_i}{\partial y} + \beta_i Q_i - f_i\right)\Psi dy.$$

Since $Q_i \in H^1(\Omega_i)$, $\frac{\partial Q_i}{\partial t} \in L^2([0,T])$ and $f_i \in L^2(]k_{i,1}, k_{i,2}[)$, we can deduce that $\frac{\partial Q_i}{\partial y} \in H^1(]k_{i,1}, k_{i,2}[)$. Since we are in 1D we can deduce that $\frac{\partial Q_i}{\partial y}$ is continuous. It means that $Q_i \in C^1(]k_{i,1}, k_{i,2}[)$. The function Q_i is not derivable at $k_{i,1}$ and $k_{i,2}$. Indeed our condition at the bifurcations imply that at each bifurcation (see equations (3.12) and (3.13)), the derivative on the right and the one on the left are different.

Periodicity

We suppose that the function $u_i(t)$ is periodic with a period T, *i.e.*

$$u_i(T+t) = u_i(t).$$

We know that a solution to our model exists and is continuous in time. We now want to know if our solution is asymptotically periodic of period T.

Theorem 3.2.6 (Periodicity). *Let us assume that,*

$$\alpha k \varrho_s + \frac{u_N(t)}{2} \geqslant 0.$$

The solution of our equations (3.15) is then asymptotically periodic in time for the L^2 *norm with a period* T*, i.e. we have,*

$$\|Q(T+t,y) - Q(t,y)\|_{L^2(\Omega)} \underset{t\to+\infty}{\longrightarrow} 0. \tag{3.18}$$

Proof. Let us have,

$$\tilde{Q}(t,y) = Q(T+t,y) - Q(t,y).$$

It verifies the following equation,

$$\frac{\partial \tilde{Q}}{\partial t} - \theta_1(y)\frac{\partial^2 \tilde{Q}}{\partial y^2} + \theta_2(t)\frac{\partial \tilde{Q}}{\partial y} + \theta_3(y)\tilde{Q} = 0.$$

and the following boundary conditions,

$$\begin{cases} \tilde{Q}(t,0) = 0 \\ -\dfrac{2^{N-G+1}D}{l_N}\dfrac{\partial \tilde{Q}(t,k_{N,2})}{\partial y} = \alpha k \varrho_s \tilde{Q}(t,k_{N,2}). \end{cases}$$

The conditions at the bifurcations remain the same. And finally the initial condition writes,

$$\tilde{Q}(0,y) = \tilde{Q}^0(y) = Q(T,y) - Q(0,y).$$

The variationnal formulation writes for $\Psi \in V_0$,

$$\int_\Omega \frac{\partial \tilde{Q}}{\partial t}\Psi \, \mathrm{d}y + a(\tilde{Q},\Psi) = 0,$$

where

$$a(\tilde{Q},\Psi) = \int_\Omega \theta_1(y)\frac{\partial \tilde{Q}}{\partial y}\frac{\partial \Psi}{\partial y}\,\mathrm{d}y + \theta_2(t)\int_\Omega \frac{\partial \tilde{Q}}{\partial y}\Psi\,\mathrm{d}y + \int_\Omega \theta_3(y)\tilde{Q}\Psi\,\mathrm{d}y$$
$$+\frac{2^{N-G+1}\alpha k\varrho_s}{l_N}\tilde{Q}(t,k_{N,2})\Psi(k_{N,2}),$$

Let us choose $\Psi = \tilde{Q}$, we then have,

$$\frac{1}{2}\frac{d}{dt}\|\tilde{Q}\|^2_{L^2(\Omega)} = -a(\tilde{Q},\tilde{Q}).$$

Let us compute the following integral,

$$J = \theta_2(t)\int_\Omega \frac{\partial \tilde{Q}}{\partial y}\tilde{Q}\,dy = \theta_2(t)\left[\frac{1}{2}\tilde{Q}^2\right]_0^{k_{N,2}} = \frac{\theta_2(t)}{2}\tilde{Q}^2(t,k_{N,2}).$$

Finally we obtain the following quadratic form

$$a(\tilde{Q},\tilde{Q}) = \int_\Omega \theta_1(y)\left(\frac{\partial \tilde{Q}}{\partial y}\right)^2 dy + \int_\Omega \theta_3(y)\tilde{Q}^2\,dy$$
$$+\frac{2^{N-G+1}}{l_N}\left(\alpha k\varrho_s + \frac{u_N(t)}{2}\right)\tilde{Q}^2(t,k_{N,2}).$$

Previously we proved that,

$$a_1(\tilde{Q},\tilde{Q}) = \int_\Omega \theta_1(y)\left(\frac{\partial \tilde{Q}}{\partial y}\right)^2 dy + \int_\Omega \theta_3(y)\tilde{Q}^2\,dy$$
$$\geqslant \eta_1\left\|\tilde{Q}\right\|^2_{H^1(\Omega)} \geqslant \eta_1\left\|\tilde{Q}\right\|^2_{L^2(\Omega)}.$$

We know that $\alpha k\varrho_s + u_N(t)/2 \geqslant 0$, we then can deduce that,

$$\frac{2^{N-G+1}}{l_N}\left(\alpha k\varrho_s + \frac{u_N(t)}{2}\right)\tilde{Q}^2(t,k_{N,2}) \geqslant 0.$$

We obtain,

$$a(\tilde{Q},\tilde{Q}) \geqslant \eta_1\left\|\tilde{Q}\right\|^2_{L^2(\Omega)}.$$

Finally we have,

$$\frac{d}{dt}\left\|\tilde{Q}\right\|^2_{L^2(\Omega)} \leqslant -2\eta_1\left\|\tilde{Q}\right\|^2_{L^2(\Omega)}.$$

Thanks to the Gronwall lemma, we obtain,

$$\left\|\tilde{Q}\right\|^2_{L^2(\Omega)} \leqslant \left\|\tilde{Q}^0\right\|^2_{L^2(\Omega)}\exp(-2\eta_1 t).$$

Then,

$$\lim_{t\to\infty}\left\|\tilde{Q}\right\|^2_{L^2(\Omega)} = 0,$$

hence the solution is asymptotically periodic at $t \to \infty$.

□

We proved the asymptotic periodicity for

$$\alpha k\varrho_s + \frac{u_N(t)}{2} \geqslant 0.$$

This condition is satisfied in our model for an amplitude of ventilation inferior to $4\,\mathrm{m}\cdot\mathrm{s}^{-1}$. Let us remark that we could choose to have two different boundary conditions at the outlets of the tree depending on the velocity,

$$\begin{cases} -\dfrac{2^{N-G+1}D}{l_N}\dfrac{\partial Q(t,k_{N,2})}{\partial y} = \alpha k\varrho_s Q(t,k_{N,2}), & \text{for } u_N \geqslant 0,\\ \dfrac{u_N}{l_N}Q(t,k_{N,2}) - \dfrac{2^{N-G+1}D}{l_N}\dfrac{\partial Q(t,k_{N,2})}{\partial y} = \alpha k\varrho_s Q(t,k_{N,2}), & \text{for } u_N < 0. \end{cases}$$

With these two conditions, we could obtain the asymptotic periodicity for all velocities. However, we did not make this assumption in our model since we observed a numerical periodicity even for high amplitude of ventilation.

Comparison of the stationnary and non stationnary solutions

We proved in the last sections that the solution of the equation (3.2) exists and is unique. We can now compare the two solutions and confirm our assumption exposed previously that, in the case of the lung at rest the stationnary solution is not a good approximation of the general solution. Indeed, we can observe that at rest, when the air velocity is at its peak (Figure 3.8 (a)), the two solutions differ around the middle of the lung ($11^{\text{th}} - 12^{\text{th}}$ generation) in the convective tree. Whereas during maximal exercise, we can observe that when the velocity is as its peak (Figure 3.8 (b)) the stationnary solution is a good approximation in the convective tree. The difference appears around the 19^{th} generation of the lung, in the acinus. It confirms our analysis based on the adimensionalisation of our equations in section 3.2.2.

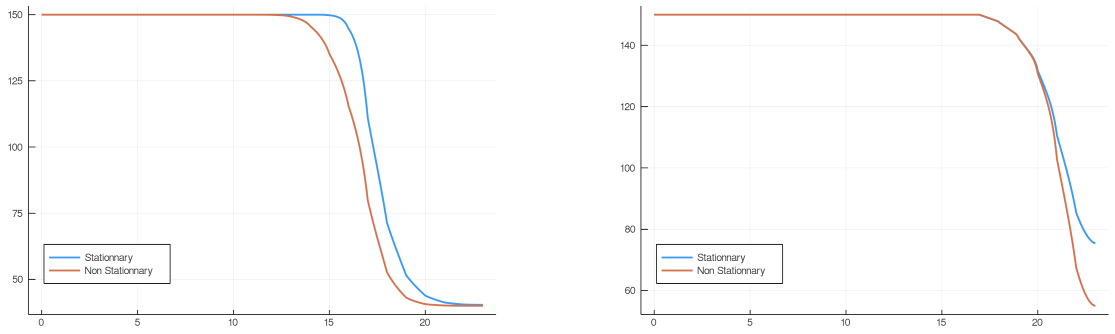

Figure 3.8: Comparison between stationnary and non stationnary solution at rest (left) and during intense exercise (right) at the inspiration peak.

Finally we can compare the two solutions when the velocity is null (Figure 3.9). The two solutions differ everywhere in the lung. This analysis shows that the time dynamics have to be included in the equations in order to reach satisfactory predictions for different metabolic regimes. In the following, we will use the non stationnary approximation of the solution computed by an implicit finite difference numerical scheme, described in appendix A, using the language Julia [11].

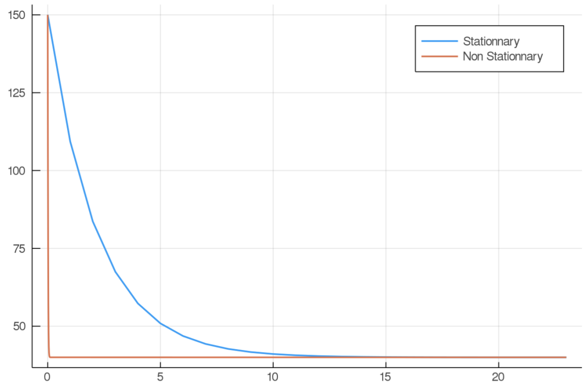

Figure 3.9: Comparison between the stationnary and the non stationnary solutions when the velocity of the air is equal to 0 m/s.

3.3 Blood partial pressures

3.3.1 Modelling the exchanges between alveolar gas and blood

In the previous section we assumed that the partial pressure of the gas in the blood (P_{blood}) was a constant, but it is actually dependent on time, space and gas species.

Oxygen

Oxygen can be found in blood dissolved in the plasma and linked to hemoglobin. To compute P_{blood,O_2} for oxygen, we use the formulation from [34]. We can relate P_{blood,O_2} to the partial pressure of oxygen in the acini, P_{AO_2}, with several physiological quantities by establishing a matter balance,

$$\overbrace{\alpha(P_{AO_2} - P_{\text{blood},O_2})}^{\text{flow going through the membrane}} \quad = \quad \underbrace{4Z_0\left(f(P_{\text{blood},O_2}) - f(P_{aO2})\right)v_s + \sigma v_s(P_{\text{blood},O_2} - P_{aO_2})}_{\text{flow transported by the blood}}.$$

The first term on the right hand side represents the link to hemoglobin. The factor 4 corresponds to the fact that a molecule of hemoglobin can link 4 molecules of oxygen. Z_0 represents the concentration of hemoglobin in the blood (9.93 $\text{mol}\cdot\text{m}^{-3}$ [24]). The function f is the oxygen saturation of hemoglobin in the blood. This function is usually modelled using the following Hill equation (Figure 3.10) [50],

$$f(x) = \frac{x^{2.6}}{x^{2.6} + 26^{2.6}}.$$

The second term on the right hand side of the equation represents the oxygen solubility in the plasma. σ is the solubility coefficient ($\text{mol}\cdot\text{m}^{-3}\cdot\text{mmHg}^{-1}$) of oxygen in blood and P_{aO_2} is the partial pressure of oxygen in pulmonary arterial blood.

Finally, present in the two parts of the equation, we have v_s the blood velocity ($\text{m}\cdot\text{s}^{-1}$). It can be computed as the ratio of the length of the capillary (l_c) over

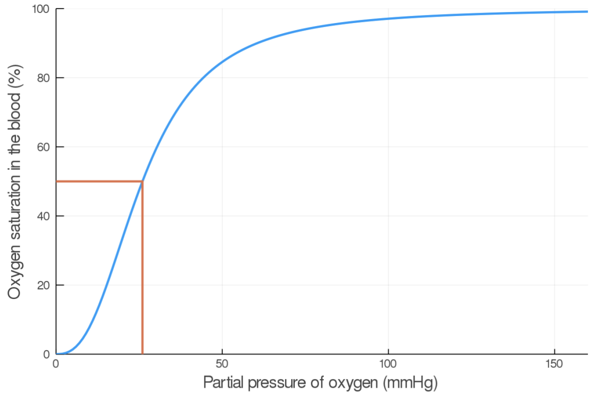

Figure 3.10: Percentage of total hemoglobin that is saturated with oxygen in the blood modeled by an Hill function (blue curve). The red curve represents the value P_{50} which is the oxygen partial pressure for which the oxygen saturation of hemoglobin is 50%. For humans, we have $P_{50} = 26$ mmHg.

the transit time in the capillary (t_c). In our model the length l_c is supposed to be constant and equals to 1 mm [113]. The transit time is defined as the time the red blood cells spend in the capillary. At rest, the value is around 1 second for humans [47].

The partial pressure of the oxygen in the blood P_{blood,O_2} is computed numerically as a function of the alveolar oxygen partial pressure P_{AO_2} (see Figure 3.11).

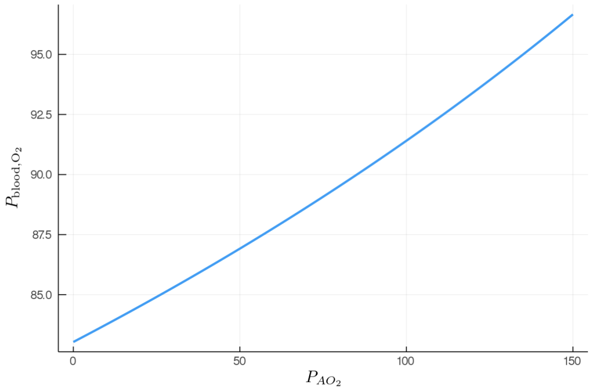

Figure 3.11: Oxygen partial pressure in the blood as a function of the alveolar oxygen partial pressure.

Carbon dioxide

In the blood, carbon dioxide can be dissolved in plasma, linked to hemoglobin or linked to bicarbonate ions. The matter balance equation for the carbon dioxide is computed using [104],

$$\overbrace{\alpha(P_{ACO_2} - P_{\text{blood},CO_2})}^{\text{flow through the membrane}} = (P_{\text{blood},CO_2} - P_{aCO_2})\,\sigma\,v_s\,\left(1 + 10^{(pH-pK)}\right)$$

$$\times \underbrace{\left(1 - \frac{0.0289\, Z_0}{(3.352 - 0.456\, SO_2) \times (8.142 - pH)}\right)}_{\text{flow transported by the blood}},$$

with v_s the blood velocity (m·s^{-1}), σ the solubility coefficient (mol·m^{-3}·mmHg^{-1}) of carbon dioxide in blood, pH the blood pH that is equal to 7.4 [104], $pK = 6.09072$ the dissociation coefficient of the chemical system $CO_2 - HCO3^-$ [104], Z_0 the hemoglobin concentration ($\mathrm{g} \cdot \mathrm{dL}^{-1}$) and SO_2 the oxygen-hemoglobin saturation (percents).

The partial pressure of the carbon dioxide in the blood P_{blood,CO_2} is shown as a function of the alveolar oxygen partial pressure P_{AO_2} in Figure 3.11.

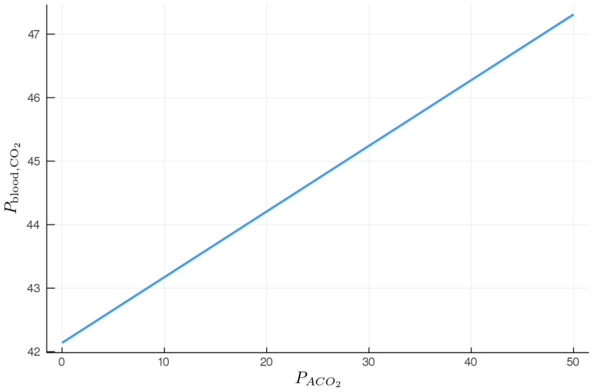

Figure 3.12: Carbon dioxide partial pressure in the blood as a function of the alveolar carbon dioxide partial pressure.

3.3.2 Effective partial pressure estimation

Practically, the arterial partial pressure of oxygen P_{aO_2} and carbon dioxide P_{aCO_2} seen by the acini might be different to that of the pulmonary arterial circulation, as the history of the blood flowing in the acini wall is unknown. Blood could have already been in contact with acini air upstream. Consequently, we compute and use, instead of P_{aO_2} and P_{aCO_2}, effective partial pressures in oxygen $\tilde{P}_{aO_2}$ and in carbon dioxide $\tilde{P}_{aCO_2}$ using rest regime as a reference state and fitting the physiological parameters known for that reference state.

To compute the exchanges between alveolar air and blood, we need to estimate the effective gas partial pressure in the pulmonary arterial and veinous blood [33]. For low oxygenated blood (pulmonary arterial blood), $P_{aO_2} = 40$ mmHg and $P_{aCO_2} = 47$ mmHg. For oxygenated blood (pulmonary veinous blood), we have $P_{vO_2} = 100$ mmHg and $P_{vCO_2} = 40$ mmHg.

In our case, tidal volume (V_T), mean air flow velocity in trachea ($u_{0,\mathrm{mean}}$) and trachea cross-sections (S_0) are related thanks to this expression,

$$V_T = \int_0^{T/2} u_{0,mean}\, S_0 \,\mathrm{d}t,$$

since u_0 is assumed to be a sine function equals to,

$$u_0(t) = A \sin\left(\frac{2\pi}{T}t\right).$$

A represents the amplitude ($\mathrm{m} \cdot \mathrm{s}^{-1}$) and T (s) the period of the idealised ventilation.

The mean airflow velocity then writes :

$$u_{0,\mathrm{mean}} = \frac{2}{T}\int_0^{T/2} A \sin(\frac{2\pi}{T}t)\, \mathrm{d}t = \frac{2A}{\pi}.$$

During rest ventilation, a human breathes around 12 times a minute, which corresponds to a period of $T = 5$ s; the tidal volume is about $0.5\,\mathrm{L}$ [33]. If we inject this expression into the tidal volume expression, we obtain $A = 1.2\ \mathrm{m} \cdot \mathrm{s}^{-1}$.

With all these parameters, our transport model allows to compute the amount of oxygen captured by the blood (VO_2) : $3.13 \times 10^{-4}\,\mathrm{mol} \cdot \mathrm{s}^{-1}$ and the amount of carbon dioxide expelled from the blood (VCO_2): $1.35 \times 10^{-4}\,\mathrm{mol} \cdot \mathrm{s}^{-1}$. These values are in the range of physiological data which is $1 - 2 \times 10^{-4}\,\mathrm{mol} \cdot \mathrm{s}^{-1}$ [54].

Another coefficient, the respiratory exchange ratio, has to be taken into account to model more accurately the gases exchanges with the blood. This coefficient is the ratio of the amount of oxygen captured by the blood and of the amount of carbon dioxide expelled from the blood. The respiratory exchange ratio (RER) is defined as follow:

$$\mathrm{RER} = \frac{VCO_2}{VO_2}.$$

The physiological range of the RER is 0.7 to 1. Using in our model typical arterial and veinous partial pressures in blood, this coefficient is predicted to be about 0.43. The physiological value at rest is however about 0.8 [33]. In order to reach a correct value of the RER, we have to account in our model for the fact that blood could have captured oxygen at its previous visited locations: we need to use an effective partial pressure for arterial blood. As shown on Figure 3.13, the value $\tilde{P}_{art} = 90.5$

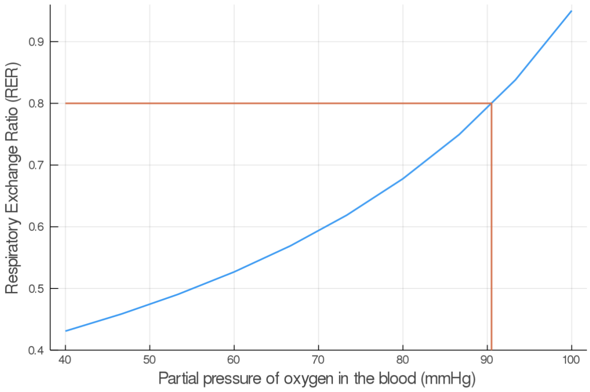

Figure 3.13: Respiratory exchange ratio in function of the partial pressure of the respiratory arterial blood.

mmHg allows to reach a correct RER. With this value, our model predicts at rest $VO_2 = 1.69 \times 10^{-4}\,\mathrm{mol} \cdot \mathrm{s}^{-1}$ and $VCO_2 = 1.35 \times 10^{-4}\,\mathrm{mol} \cdot \mathrm{s}^{-1}$ with a RER of 0.8.

In order to validate the choice for effective partial pressure, we did a perturbation analysis on the RER at rest, see Table 3.4.

T A	4	5	6
1.1	0.80	0.80	0.80
1.2	0.80	0.80	0.80
1.3	0.80	0.80	0.80

Table 3.4: Respiratory Exchange Ratio at rest with A the amplitude and T the period of the respiration.

We have satisfactory little variation on the RER when rest ventilation amplitude and frequency are perturbed and we remain in the physiological range.

Let us extend our analysis to maximal exercise. During more intense activities, our heart rate increases and blood circulates faster to supply in oxygen all of our cells correctly. The transit time t_c then decreases from 1 second at rest to 0.51 second at maximal exercise [47]. We can also observe a decrease of the following ratio, V_{dead}/V_T, where V_{dead} represents the dead volume, the volume of the lung that does not participate in the exchange with the blood. We can compute this volume as the sum of each bronchi's volume in the conductive tree,

$$\begin{aligned} V_{\text{dead}} &= \sum_{i=0}^{G-1} 2^i r_i^2 l_i \pi \\ &= r_0^2 l_0 \pi \sum_{i=0}^{G-1} 2^i h^3. \end{aligned}$$

Since in the convective tree we suppose that $h = 2^{-1/3}$, we obtain,

$$V_{\text{dead}} = r_0^2 l_0 \pi G.$$

We can now relate the radius of the trachea to the ratio V_{dead}/V_T. It gives us tracheal radius of 1.27 cm during maximal exercise whereas at rest we have a radius of 0.9 cm. It is in accordance with physiology since it has been observed that airways dilatation is related to work load [111].

During intense exercise, human can exhibit up to 59 breaths a minute, which represents a respiratory period around $T = 1$ second and the tidal volume can increase to 3.1 L [47]. With similar computation as we did for the rest regime, we compute an amplitude of $19\,\mathrm{m} \cdot \mathrm{s}^{-1}$. The values of the RER during exercise predicted by our model are shown on Table 3.5. They are fully compatible with the physiological data, as during exercise the RER increases with the metabolism and comes close to 1, or even sometimes exceeds it [41].

These last analyses show that our hypothesis to use an effective partial pressure in oxygen for exchanges in our model leads to predictions in good agreement with the expected physiological responses.

A \ T	0.9	1	1.1
18	0.94	0.96	0.97
19	0.96	0.97	0.98
20	0.97	0.99	1.00

Table 3.5: Respiratory Exchange Ratio during exercise with A the amplitude and T the period of the respiration.

3.4 Conclusion

We described and studied a model of gas transport in the human lung based on the core physical properties of the human's lung: a tree-like structure of the lung, convective and diffusive transports of oxygen and carbon dioxide and physiology-based exchange surface properties. This model has few parameters and gives us interesting insights on the gaseous exchanges with the blood. Also, it allows to better understand the gas distribution inside the human's lung, along the generations.

The oxygen flows exchanged with the blood computed with our model are close with the physiology. Futhermore our model is robust regarding the intense exercise rate. Indeed, it models properly the increase of the respiratory exchange ratio (RER) during the increase of intensity of exercise.

Some improvements of the model are worth considering. It could be interesting to model the change of volume of the alveolar region. Indeed, an airflow is created during inspiration due to the increase of the lung's volume that allows a pressure drop between the ambiant air and the acinus. This change in the model could induce a better modelisation of the exchange surface of the lung, especially during maximal exercise. Furthermore, we could also improve the determination of the effective arterial partial pressure of the oxygen. Indeed, since it represents a mean value of the arterial partial pressure of oxygen in all the blood capillaries connected to the lung, its value could depend on time and on the metabolic rate.

Chapter 4

Optimal ventilation in mammals

The transport of air in the lung requires a certain amount of energy due to physical constraints. Indeed, a viscous energy is spent due to friction effects of the air flow in the bronchi [72]. It is related to the hydrodynamic resistance of the lung. Furthermore, mechanical energy is needed to expand the thoracic cage and the lung tissues during inspiration. It is related to the compliance of the lung that represents the elasticity of the tissues. This energy is lost at expiration due to the viscoelastic recoil of the tissues. This spending of energy can influence the control of ventilation, which is based on the regulation of the volume of air that is inspired (tidal volume) and the frequency at which it is renewed (ventilation frequency) with the aim to keep oxygen and carbon dioxide partial pressure constant in blood. The lungs of mammals share morphological and functional properties that depend on their mass M with non trivial laws, called allometric scaling laws [43, 51, 53, 86, 117]. They write under the following form,

$$Y = aM^b,$$

where a is the prefactor, M is the mass of the mammals, b is the exponent and Y is the property shared by the mammals like for example the maximal metabolic rate as shown on Figure 4.1. These allometric scaling laws come from physiological and physical constraints [117].

Since the physics of ventilation is linked to the geometry of the lung, the morphological differences amongst mammals also affect the control of ventilation. It is confirmed by the allometric scaling laws for the ventilation frequency and tidal volume observed in physiology. For example, at basal metabolic rate (BMR), ventilation frequency has been estimated to follow the law $f_b^{\mathrm{BMR}} \approx 0.58\, M^{-0.25}$ Hz [121] and tidal volume to follow the law $V_T^{\mathrm{BMR}} \approx 7.14 \times 10^{-3}\, M^1$ L [117]. At other metabolic rates, less data are available in the literature except for the breathing frequency of mammals at maximal metabolic rate (MMR). It has been estimated to follow the law $f_b^{\mathrm{MMR}} \approx 5.08\, M^{-0.14}$ Hz [122].

Previous studies in the literature have been looking for optimal ventilation using modeling approaches [82, 75, 55]. In 1950, Otis et al. showed that by constraining the alveolar ventilation, which is the inspired air flow that enters the alveoli and participates to gas exchanges, $\dot{V}_A = (V_T - V_D) f_b$ with V_D the dead volume, an optimal breathing frequency could be computed analytically by canceling the derivative of

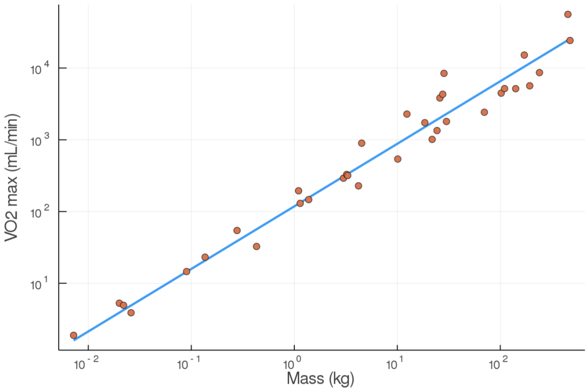

Figure 4.1: Maximal oxygen consumption $\dot{V}_{O_2}^{\max}$ as a function of the mammals mass (red dots) and the corresponding allometric scaling law (blue line), $\dot{V}_{O_2}^{\max} = 118.2\, M^{0.872}\,\mathrm{mL}\cdot\mathrm{min}^{-1}$. Values from [114].

the power relatively to the ventilation frequency f_b [82, 55],

$$f_{b,\text{pred}} = \frac{2\dot{V}_A/V_D}{1+\sqrt{1+4\pi^2 RC\dot{V}_A/V_D}}.$$

For all mammals, allometric scaling laws are available in the literature for all the quantities present in the expression for the frequency at rest. Indeed we have, $\dot{V}_A \propto M^{\frac{3}{4}}$ [43], $V_D \propto M^1$ [101], $R \propto M^{-\frac{3}{4}}$ [101, 117] and $C \propto M^1$ [101]. Consequently, we can derive an allometric scaling law for the ventilation frequency based on ventilation data in healthy humans [47], $f_{b,\text{pred}} \propto 0.9\ M^{-0.25}$ Hz. Thanks to this expression and to the alveolar ventilation expression, the allometric scaling law for the tidal volume is then, $V_{T,\text{pred}} = 7.5\ M^1$ mL. At rest, these predictions are not far from the physiological values. However, this model is not able to predict the correct allometric laws at other regimes.

More detailed models with links between ventilation, blood gas regulations and control [42, 97, 19] or even neural controls [9] have been described in the literature. These models are built on several interacting compartments mimicking the behavior of the respiratory organs and are based on large sets of parameters. However, even if it fits precisely physiological responses, these types of models do not allow to understand easily the physical phenomena linking the lung's properties and the ventilation characteristics.

We propose a model that is based on the core physical phenomena involved in lung's function and ventilation [113]. Indeed thanks to our gas transport model defined in the previous chapter, we can link the parameters of the ventilation to the amount of oxygen exchanged with the blood through the geometry of the lung. Furthermore this model can predict results close to physiological data for all mammals and at different regimes.

4.1 Minimization of the power spent for the ventilation of the lung

In the previous chapter, we assumed that the air flow velocity in the trachea could be idealized by a sinusoidal pattern in time, *i.e.*

$$u_0(t) = A \sin\left(\frac{2\pi}{T} t\right).$$

This expression is an approximation, since for example for humans, the inspiration (around 2 seconds) lasts less than expiration (around 3 seconds) [71]. The quantity A is the air velocity amplitude and T is the period of ventilation, inverse of the breathing frequency $f_b = 1/T$. Denoting $S_0 = \pi r_0^2$ the surface area of the tracheal cross-section, the tidal volume is

$$V_T = \int_0^{\frac{T}{2}} S_0 u_0(s) \mathrm{d}s = \frac{A S_0 T}{\pi}.$$

The parameterization of ventilation using (A, T) or (V_T, f_b) are equivalent.

The power spent by the lung to bring air in contact with the exchange surface can be divided in two parts [55]: a mechanical part due to the elasticity of the tissue and a viscous part due to the hydrodynamic resistance induced by the bronchial tree on the air flow.

First, the motion of the tissues out of their equilibrium position implies that the diaphragm has to furnish, during inspiration, an amount of energy that is stored in the tissues as elastic energy. This energy is then used during expiration for a passive tissues recoil. It means that there is a relaxation of the muscle to the initial volume of the lung without spending energy. The power spent $\mathcal{P}_e(A, T)$ is related to the elastic properties of the thoracic cage and of the lung. These properties depends on the lung's compliance $C \sim 5 \times 10^{-7}\,\mathrm{m}^3 \cdot \mathrm{Pa}^{-1}$ (human) [2] which is defined as the ratio between the change in volume of the lung and the change in transpulmonar pressure. Compliance depends notably on lung's volume when deformation is high, as shown by the pressure-volume curves in [3] but can be considered constant in "normal lung's functionning". In this work, the compliance is assumed constant and we neglect the non linearities arising at large lung's deformations. We obtain,

$$\mathcal{P}_e(A, T) = \frac{1}{T} \int_0^{\frac{T}{2}} \frac{1}{C} V(t) V'(t) \mathrm{d}t = \frac{1}{C} \frac{A^2 S_0^2 T}{2\pi^2},$$

where $V(t) = \int_0^t S_0 u_0(s) \mathrm{d}s$ is the volume of air inhaled as a function of time.

Second, the airflow inside the bronchi induces an energy loss due to viscous effects that has to be compensated by the motion of the diaphragm during inspiration. The viscous power dissipated depends on the hydrodynamic resistance of the lung $R \sim 2 \times 10^5$ $\mathrm{Pa} \cdot s \cdot \mathrm{m}^{-3}$ (human) [23]. It writes,

$$\mathcal{P}_v(A, T) = \frac{1}{T} \int_0^{\frac{T}{2}} R u_0^2(t) S_0^2 \mathrm{d}t = R \frac{A^2 S_0^2}{4}.$$

Finally, the total power spent is the sum of the power spent for the displacement of the tissues and for compensating viscous effects due to air motion in the bronchi,

$$\begin{aligned}\mathcal{P}(A,T) &= \mathcal{P}_e(A,T) + \mathcal{P}_v(A,T) \\ &= \mathcal{P}_e(A,T)\left(1+\frac{\pi^2}{2T}RC\right) = \frac{A^2 S_0^2 T}{2\pi^2 C}\left(1+\frac{\pi^2}{2T}RC\right). \quad (4.1)\end{aligned}$$

The power can also be expressed using the equivalent ventilation parameters (V_T, f_b), where V_T is the tidal volume and f_b is the ventilation frequency,

$$\tilde{\mathcal{P}}(V_T, f_b) = \frac{V_T^2 f_b}{2C}\left(1+\frac{\pi^2 f_b RC}{2}\right).$$

The function $(A,T) \to \mathcal{P}(A,T)$ is to be minimized relatively to the ventilation amplitude A and the period T with the constraint $f_{O_2}(A,T) = \dot{V}_{O_2}$. $f_{O_2}(A,T)$ is the oxygen flow resulting from a ventilation with characteristics (A,T). It is computed thanks to the gas transport model defined in chapter 3 with the expression 3.5. $\dot{V}_{O_2}$ is the desired oxygen flow, it depends on the metabolic rate as shown on Table 4.1. First, only the oxygen flow is constrained, the carbon dioxide flow will be constrained later in the following section.

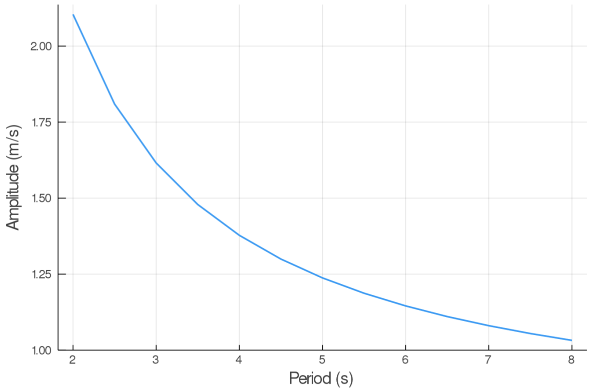

Figure 4.2: Predicted link between ventilation amplitude and period when the oxygen flow is constrained (rest regime). It is obtained by solving, $f_{O_2}(A,T) - \dot{V}_{O_2} = 0$, for each period T.

Practically, the ventilation period T and the amplitude A can be linked through the constraint on the flow of oxygen to the blood, in the form of a non linear function $T \to A(T)$. The non linear function is the result of the transport model of oxygen. For a given value of the period, only one value of the amplitude is possible in order to check the constraint. The amplitude has to be high enough to bring the oxygen source close to the exchange surface so that diffusion is quick to drive the transport. This behavior is shown on Figure 4.2 where the function $T \to A(T)$ is plotted. For each period T, we look for the corresponding amplitude A by solving thanks to the secant method,

$$f_{O_2}(A,T) - \dot{V}_{O_2} = 0.$$

Consequently, with the oxygen flow constraint, the optimization problem is unidimensional and we search for the minimum of the function $\mathcal{P}$ or the zero of its derivative relatively to T,

$$\frac{\partial \mathcal{P}}{\partial T}(A(T),T) = \left(A'(T)\left(\frac{1}{2}+\frac{T}{\pi^2 RC}\right)+\frac{A(T)}{2\pi^2 RC}\right)A(T)RS_0^2 = 0.$$

Since we impose a positive oxygen flow, the value $A(T)$ must be different than zero. Consequently we only need to search the zero of the function,

$$\mathcal{D}(T) = A'(T)\left(\frac{1}{2}+\frac{T}{\pi^2 RC}\right)+\frac{A(T)}{2\pi^2 RC}.$$

The numerical algorithm is detailed in appendix A. Interestingly, the optimal ventilation does not depend independently on the hydrodynamic resistance R and on the compliance C, as it depends on the product RC only. Hence, we are expecting the same behaviors for optimal ventilation relatively to changes in hydrodynamic resistance or changes in compliance.

4.2 Human's optimal ventilation

Let us compare the predictions of our model with different physiological cases. We choose to mimic three physiological simulations. The first one is the physical activity, the second one is the effect of altitude and finally the last one is the change in hydrodynamic resistance linked to a change in lung's size.

4.2.1 Physical activity

Our first physiological case aims to mimic the physical activity. Indeed, in the everyday life, our body experiences metabolism changes: resting, walking, exercising. Indeed, as explained in the previous chapter, the transit time in the blood capillaries decreases as the intensity rises since the blood velocity increases. Furthermore, in order to inhale more oxygen, the bronchi dilate [47]. To model exercise, we need to adjust the transit time in the blood capillaries, the increase of the bronchi radius in the bronchial tree and the increased body's need in oxygen. We run the model for different amount of oxygen, mimicking the different intensities [26] depending on the maximal oxygen consumption ($\dot{V}_{O_2}^{\max}$). The parameter's changes are detailed on Table 4.1.

At rest, the model predicts an optimal ventilation amplitude of $1.25\,\mathrm{m}\cdot\mathrm{s}^{-1}$ and a ventilation period of 4.91 seconds (see Table 4.2). Both values are very close to the acknowledged physiological values [113]. The model exhibits a robustness in term of period perturbation around the optimal. A 5% shift in the energy brings the period into a range between 3.25 seconds up to 7.5 seconds. This effect is due to the fact that, at low regimes, a low amplitude A is sufficient to perform an optimal ventilation. As the power depends on the period with the quantity A^2T, if A is small then A^2T remains small whatever reasonable values for period T. When the exercise intensity increases, the power profiles as a function of the period become

Percentage of $\dot{V}_{O_2}^{\text{MAX}}$ (Exercise)	$\dot{V}_{O_2}$ (L $\cdot$min^{-1})	r_0 (cm)	t_c (s)
Rest (Sitting)	0.24	0.90	1
30 % (Walking)	0.9	0.93	0.71
45 % (Ballet)	1.35	1.05	0.65
60 % (Bicycling)	1.8	1.20	0.59
75 % (Handball)	2.25	1.25	0.55
90 % (Basketball)	2.7	1.27	0.52
100 % (Running)	3	1.27	0.51

Table 4.1: The flows of oxygen consumed, the tracheal radius and the transit time in function of the intensity of exercise. The radius r_i of the bronchi in the bronchial tree ($i \in [\![0, G-1]\!]$) are deduced from the tracheal radius as follow, $r_i = r_0 h^i$, where $h = \left(\frac{1}{2}\right)^{1/3}$ is the reduction factor between the generations.

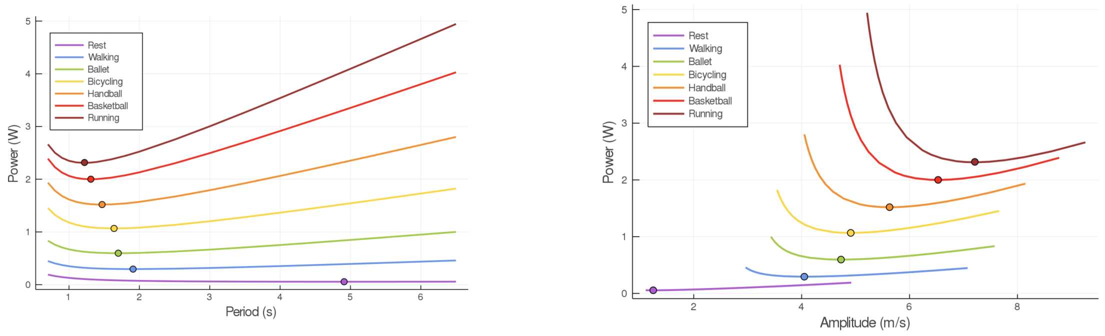

Figure 4.3: Power as a function of ventilation period (left) and amplitude (right) for different intensity of exercise.

steeper and steeper and focus the optimal value within a tighter region. It implies that a shift from the optimal configuration at high intensities is predicted to be costly in term of energy spent. This behavior is fully compatible with the fact that the control of ventilation is stronger at exercise, preventing even talking. At $\dot{V}_{O_2}^{\max}$, we observe a period of 1.22 seconds or a frequency of 49 breaths per minute during maximal exercise, which is very close to physiology (around 44 breaths per minute [47]). However, measured data for physiological amplitude [13] range between 7 and 21 $\text{m} \cdot \text{s}^{-1}$. The optimal ventilation amplitude computed in our model at maximal exercise is around $7\,\text{m} \cdot \text{s}^{-1}$, in the physiological range but on the lower side. A possible explanation for this underestimation might be that our model does not account for the wide range of possible human physiology and body needs as our study is based on one set of parameters only. Indeed, we could rise the value for $\dot{V}_{O_2}^{\max}$ and obtain a lower period but a higher amplitude. A second explanation could be that the resistance and the compliance have non linear effects at high metabolic rates which are not taken into account here.

In term of oxygen transport (Figures 4.4), as soon as the air flow is deep enough in the tree, diffusion is able to bring easily the needed oxygen flow to the exchange surface in the first generations of the acini. The deepest parts of the acini are not

Exercise	Optimal amplitude ($\mathrm{m} \cdot \mathrm{s}$)	Optimal period (s)
Sitting	1.25	4.91
Walking	4.05	1.91
Ballet	4.73	1.70
Bicycling	4.91	1.64
Handball	5.63	1.47
Basketball	6.53	1.31
Running	7.21	1.22

Table 4.2: Optimal ventilation amplitude and period for different intensities of exercise.

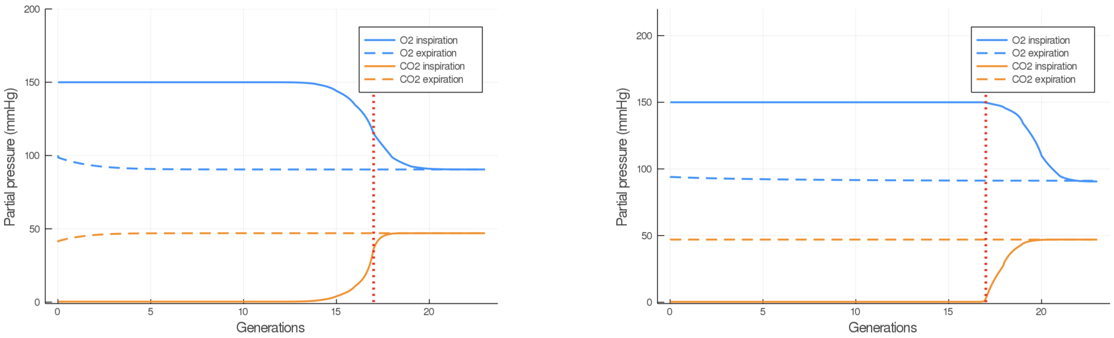

Figure 4.4: Partial pressure distribution in the human lung at rest (left) and during maximal exercise (right). Results are plotted for peak flows. The red dotted line represents the end of the bronchial tree and the start of the acinus.

contributing substantially to the oxygen flow: this effect is called acini screening [96] and it is the strongest at rest regime. The screening effect leaves some exchange surface available for exercise, as a reserve. It brings also a robustness to reduced efficiency of the exchange surface. For example, our model can mimic the physiological effects of a pulmonary oedema by increasing the thickness of the alveolo-capillary membrane τ defined in the previous chapter in equation (3.1). As shown on Figure 4.5, the oxygen flow is not really affected up to a point where the screening disappears which means that no more exchange surface is available [96]. Then, any subsequent increase of the membrane thickness τ reduces the oxygen flow, crashing suddenly the patient.

As amplitude increases, the oxygen source goes deeper within the lung, entering the acini and increasing the exchange efficiency, but by thus draining more quickly oxygen from air. Renewing of the internalized air becomes more crucial to keep sufficient oxygen flow. A similar behavior occurs for carbon dioxide, but in the opposite direction.

The respiratory exchange ratio (RER) follows the expected physiological response. Indeed we can observe on Figure 4.6 that this ratio is rising as the intensity of the exercise increases. However at $\dot{V}_{O_2}^{\max}$, the optimal value corresponds to a RER of 0.85 when it should be closer to 1, or even above it [41].

This underevaluation could be explained by the fact that only oxygen exchanges

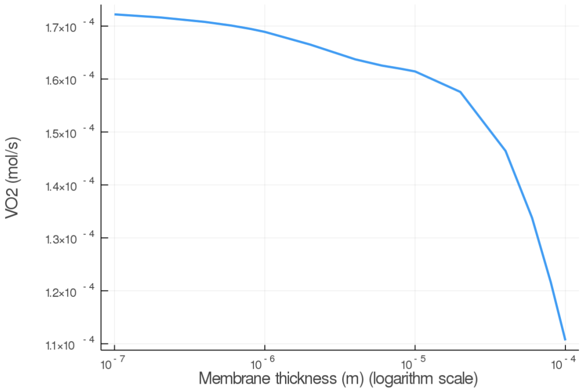

Figure 4.5: Model response in term of oxygen flow to an increase of alveolar membrane thickness at rest to mimic pulmonary oedema.

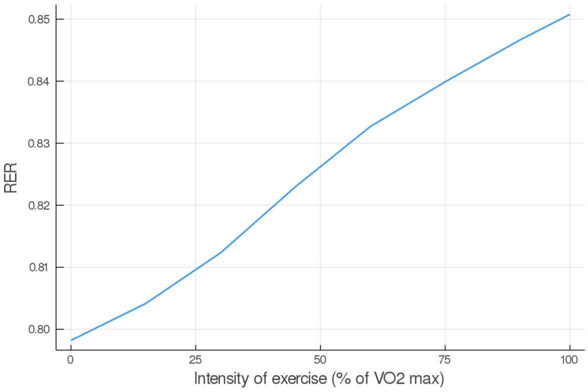

Figure 4.6: Respiratory Exchange Ratio as a function of intensity of exercise.

are constrained and not carbon dioxide. In order to validate or reject this hypothesis, let us now compute the optimal ventilation by constraining the carbon dioxide flow. We ran our model for different values of expired carbon dioxide flow [26], modeling different intensities of exercise, as shown on table 4.3. The transit time and the radius of the trachea remains the same as the one taken for the optimization with the oxygen constraint (see Table 4.1).

At rest, the optimal ventilation is very similar if we use an oxygen or a carbon dioxide constraint as shown on Figure 4.7. Indeed, the optimal amplitude is the same $1.25\,\mathrm{m}\cdot\mathrm{s}^{-1}$ for the two constraints and the optimal period is very close with 4.91 s for the oxygen constraint and 4.83 s for the carbon dioxide constraint. It might be explained by the fact that, in the previous chapter (in section 3.3.2), we imposed for a physiological ventilation with an amplitude of $1.2\ \mathrm{m}\cdot\mathrm{s}^{-1}$ and a period of 5 s, a RER of 0.8. Here, the optimal ventilation found with our model for the oxygen flow constrained is close to the physiological one and the carbon dioxide flow constrained have a RER of 0.8 with the oxygen flow.

As the intensity of the exercise increases, the optimal ventilation frequency differs more and more between the two constraints. Indeed, we impose a carbon dioxide

Percentage of $\dot{V}_{O_2}^{\text{max}}$ (Exercise)	$\dot{V}_{CO_2}$ (L $\cdot$min^{-1})
Rest (Sitting)	0.19
30 % (Walking)	0.77
45 % (Ballet)	1.21
60 % (Bicycling)	1.71
75 % (Handball)	2.31
90 % (Basketball)	3
100 % (Running)	3.3

Table 4.3: Flow of carbon dioxide exchange in function of the intensity of exercise.

flow higher than the one obtained with the optimal ventilation parameters under the oxygen constraint. Hence, the frequency has to be higher in order to expelled the right amount of carbon dioxide.

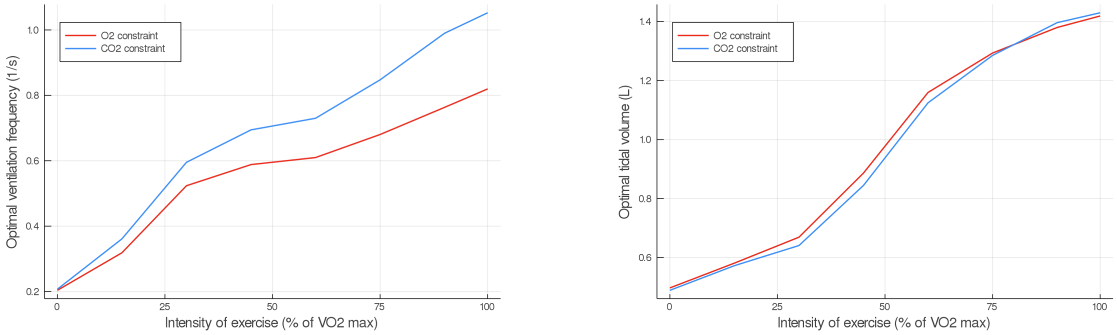

Figure 4.7: Optimal frequency (left) and tidal volume (right) as a function of the intensity of exercise when the constraint of the optimization is the O_2 flow (red curve) or the CO_2 flow (blue curve).

Interestingly, for both constraints, we obtain very similar results for the tidal volume. For each intensities, the same volume of air is inhaled but it is renewed at different frequencies depending on the constraint. At maximal exercise, under the CO_2 constraint we obtain a RER of 0.87 which is really close from the one under the O_2 constraint. We can observe that finally, we have similar results for the RER and the tidal volume whatever the constraint. Furthermore the results obtained for the period with the oxygen constraint are more compatible with the physiology. It might by explained by the fact that we only chose to use an effective arterial partial pressure for the oxygen and not for the carbon dioxide in order to obtain a RER of 0.8 at rest (see section 3.3.2 in the last chapter). This is why we will mainly use the oxygen constraint in the following.

In order to have a more physiological RER, we could think about constraining at the same time the oxygen and the carbon dioxide flow. However with our model, it is currently not feasible because we do not have enough degrees of liberty. Indeed we could suppose that the effective partial pressure of oxygen in the blood is not a constant but a parameter of the gases flow.

4.2.2 Altitude induced hypoxia

In our everyday life, we do not always remain at sea level, we may go higher in altitude and hence be confronted to an ambient air poorer in oxygen. That is why our second physiological case is mimicking hypoxia induced by altitude. Hypoxia corresponds to an insufficiant supply of oxygen regarding the body needs. It can be the consequence of an alteration of the gas flows between the alveoli and the blood or of the absence of the renewal of the air in the alveoli. This is typically one of the response observed in high altitude [103, 84] where the flows are reduced by the smaller pressure gradient at the air/blood interface. To mimic altitude in our model, we alter the variable representing the partial pressure of oxygen in the ambient air while keeping the needed oxygen flow rate constant, see [118] and Table 4.4. In this framework, we can compare the predictions of our model with known physiological responses [8].

Altitude (m)	Inspired oxygen partial pressure (mmHg)
0	150
500	140
1000	132
1500	123
2000	117
2500	108
3000	103
3500	94

Table 4.4: Inspired partial pressures in oxygen as a function of altitude. Data from [118].

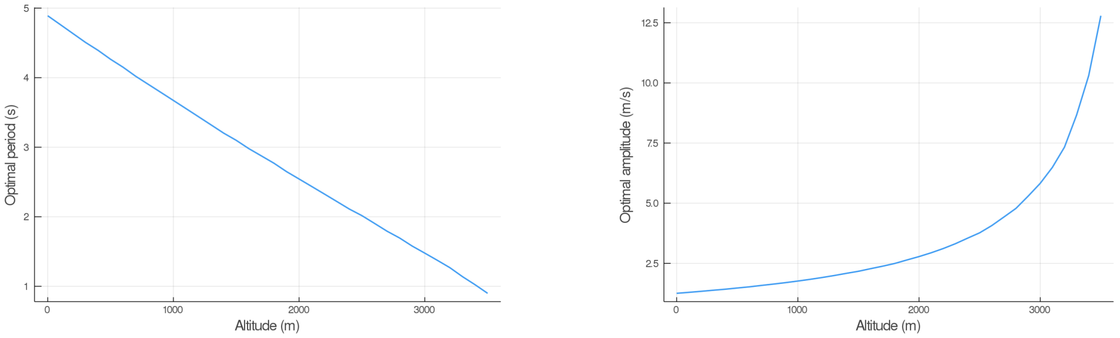

Figure 4.8: Optimal ventilation period (left) and amplitude (right) as a function of altitude.

Our model (Figure 4.8) predicts an increased ventilation in order to compensate the lower oxygen partial pressure, with lower periods and higher amplitudes. This allows to put the scarcer oxygen source deeper in the acinus and to benefit from a higher exchange surface to compensate for the lower oxygen gradient between the alveolar gas and the blood. The response predicted is fully compatible with the lung's physiology [108] and brings on the typical strategy of the lung to increase ventilation when gas exchanges are too low. When altitude is higher than 3500 meters, the model is not anymore able to fulfil the oxygen flow constraint because the inspired oxygen partial pressure is lower than our effective partial pressure in the blood, implying that blood homeostasy is not anymore sustainable in our model.

4.2.3 Response to change in hydrodynamic resistance

Finally, the lung is not identical for all humans. Indeed there are some variabilty on the size of the lung that can depend on the height, the weight, the gender of the person. The hydrodynamic resistance is a physical quantity that relates the amount of energy given to the fluid to the actual flow of the fluid. This quantity is dependent on the size of the bronchi. A change in hydrodynamic resistance then goes with a change of lung's geometry. This is why our final physiological case is the change of the hydrodynamic resistance. In our model, if we know the size reduction factor at each bifurcation of the bronchi and the tracheal radius, we can compute the equivalent hydrodynamic resistance of the whole tree as follow [71],

$$R = R_0 \left[1 + \sum_{k=1}^{NC-1} \frac{1}{(2h^3)^k} + \sum_{k=NC}^{N} \frac{1}{2^k h^{3(NC-1)}} \right].$$

R_0 is the resistance of the first generation bronchi, it writes,

$$R_0 = \frac{8\mu l_0}{\pi r_0^4},$$

where $\mu = 1.8 \times 10^{-5}\,\mathrm{Pa \cdot s}$ is the viscosity of the air. This equivalent resistance neglects the resistance of the bifurcations, the effects of inertia and turbulence, but it can give us an estimation of the evolution of the resistance regarding the parameters h and r_0. Indeed, in order to compute a value for the resistance with a different h or r_0, we chose to compute the resistance with the formula for the equivalent resistance and to determine the ratio of increase or decrease relatively to the reference value $h = \left(\frac{1}{2}\right)^{1/3} = 0.7937$ and $r_0 = 0.9$ cm. Finally, to obtain a coherent resistance we multiply this ratio with the physiological value of the resistance.

First, we chose to modify the parameter h. To increase the equivalent resistance of 30%, the corresponding size reduction factor is $h = 0.7859$ and for a decrease of the resistance of 30%, we have $h = 0.8058$.

The curves of the powers spent for the ventilation of the lung are plotted on Figure 4.9, where resistance and geometrical changes have been related with the reduction factor h between two successive generations: the amplitude of the velocity is almost the same for the three tree morphologies whereas the period decreases when the resistance increases. The highest factor h tested corresponds to an optimal period of about 6.64 seconds, the reference resistance corresponds to a period of about 4.91 seconds and the lowest factor h tested corresponds to a period of about 4.22 seconds. In all these configurations, the power remains flat around the optimal value. For an increase in resistance, typically for smaller lungs, the optimal ventilation changes significantly. Indeed if the size reduction ratio is smaller, the optimal configuration keeps the same amplitude but lowers the period. Because the

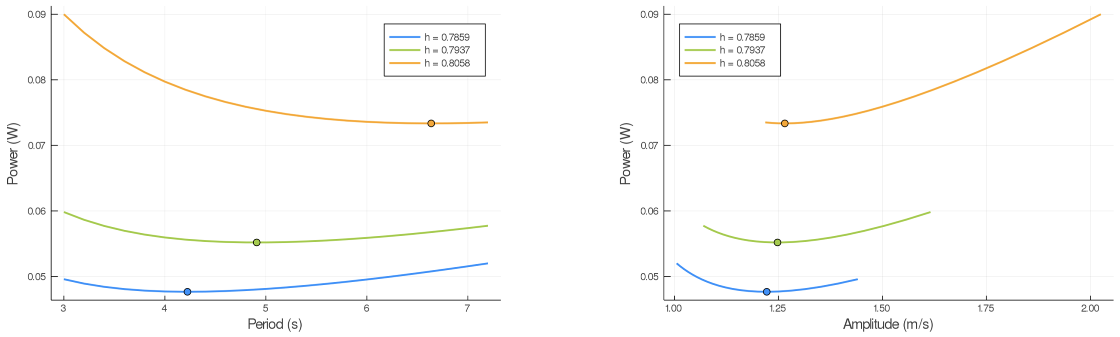

Figure 4.9: Power as a function of the ventilation period (left) and the amplitude (right) for different size reduction factor h.

exchange surface is also smaller, diffusion explores deeper in the acini, leaving less reserve for exercise. This behavior is not the one expected from physiology, mainly because the effect of an increase of resistance is first hypoxia, that induces the ventilation control to use both an higher amplitude and a smaller period. Our results show that in the optimal strategy found with our model, the resistance increase is compensated by a volume of internalized air that is smaller (same amplitude but for a lower period). The mechanical energy gained with a smaller volume to move allows a decrease of the total energy.

However, we saw that the hydrodynamic resistance depends also on the tracheal radius. Let us now modify this parameter. For a increase of resistance of about 30% we obtain a new tracheal radius of 0.82 cm and for a decrease of resistance of about 30% we have a radius of 1.01 cm.

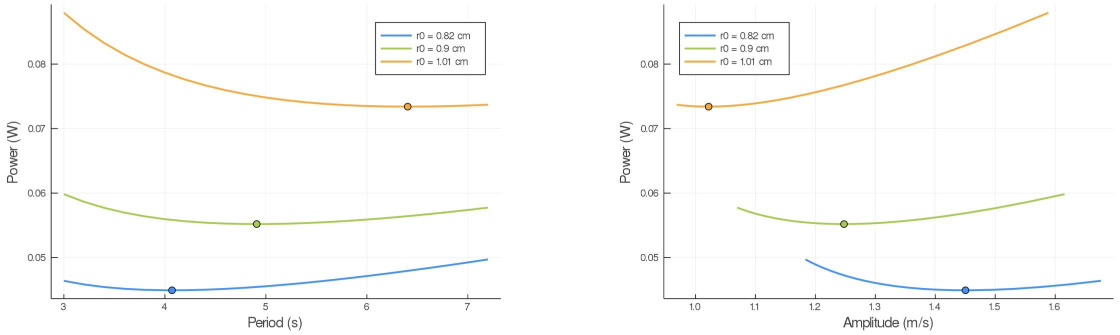

Figure 4.10: Power as a function of the ventilation period (left) and the amplitude (right) for different tracheal radii r_0.

The curves of the powers spent for the ventilation of the lung are plotted on Figure 4.10, where resistance and geometrical changes have been related to the tracheal radius r_0. Interestingly in this case the optimal ventilation is not exactly the same as the previous one with the change of the size reduction ratio. Indeed the ventilation amplitude increases when the resistance increases. The highest tracheal radius tested corresponds to an optimal amplitude of $1.02\,\mathrm{m}\cdot\mathrm{s}^{-1}$, the reference radius gives an amplitude of $1.25\,\mathrm{m}\cdot\mathrm{s}^{-1}$ and finally the lowest tracheal radius has an optimal amplitude of $1.45\,\mathrm{m}\cdot\mathrm{s}^{-1}$. However the period follows the same trend as in the previous case, and the optimal values are of the same order. In this case, for an increase of resistance, the optimal configuration increases the amplitude and lowers the period. This behavior is the one expected from physiology since the effect of an increase of the hydrodynamic resistance is first hypoxia. Our results show that in the optimal strategy found with our model, the resistance increase is compensated by a smaller lumen area which allows a decrease of the total energy.

To conclude, the response to a change in hydrodynamic resistance depends on how the lung's resistance is modified.

4.3 Mammal's optimal ventilation

The lungs of mammals share morphological and functional properties, raising the question on whether the previous results for human can be extended to all mammals. These shared properties are known to be dependent on the mass M of the animal following allometric scaling laws [43, 51, 53, 86, 117]. These laws are written as follow,

$$Y = aM^b,$$

where Y represents the morphological or functional characteristic, a is denoted as the prefactor, M is the mass of the mammals (in kg in our work) and b is the exponent. It is then essential to define the allometric scaling laws of the parameters used in our model in order to extend our work to all mammals.

4.3.1 Extension of the model to mammals

Let us extend our gas transport model and our hypotheses defined in chapter 3 in order to be validated for all mammals. First, even if there are some differences in the geometry of the lung for the mammals [105], it can be considered in a first approximation as a tree-like structure with bifurcating branches. It decomposes into two parts: the bronchial tree and the acini. The size of the branches in the bronchial tree is decreasing at each bifurcation with a ratio in the whole tree close to $h = \left(\frac{1}{2}\right)^{1/3}$ [113, 70, 56]. In the acini, the size of the branches are considered invariant at bifurcations [113, 105]. We want to relate explicitly morphological parameters in our model to the mass of the mammals. We based our hypotheses on the datasets available in [117], which brought a large set of theoretical allometric scaling laws for the cardiorespiratory system, compatible with the ecological observations.

The first morphological parameter used in our model is the trachea radius r_0. It follows the law [117],

$$r_0 = aM^{\frac{3}{8}}.$$

The prefactor a can be determined based on human data. Indeed at rest, the mean trachea radius is 0.9 cm for humans, which leads to $a = 1.83 \times 10^{-3}$, when the mass M of the animal is in kg.

The allometric law for the tracheal length is not explicitly detailed in [117]. However we can derive the exponent from the data available. Indeed the dead volume ($V_{\text{dead}} \propto M^1$) is assumed to be proportionnal to the tracheal volume [106]. Since we have

$$V_{\text{dead}} \propto \pi r_0^2 l_0 \propto M^1,$$

we can easily deduce that

$$l_0 \propto M^{\frac{1}{4}}.$$

The number of generations in the conductive tree (G) and in the acinus (H) are two essential parameters to define the geometry of the lung. The computation of G requires to assume that the radius of the alveolar ducts are similar to the radius r_A of the branches in the acini [113], for which an allometric scaling law is known [117],

$$r_A \propto M^{\frac{1}{12}}.$$

The number of generations G in the conductive tree is then obtained from the following formula,

$$r_A = r_{G-1} = r_0 h^{G-1}.$$

Indeed, since we suppose that the decreasing ratio $h = \left(\frac{1}{2}\right)^{1/3}$ is constant for all mammals, we have

$$2^{G-1} \propto M^{\frac{7}{8}}.$$

We can finally express the number of generations in the conductive tree,

$$G = \left[\frac{\log(r_A/r_0)}{\log(h)}\right] + 1 = \left[\frac{7}{8}\frac{\log(M)}{\log(2)} + \text{cst}\right] + 1.$$

We can also define the length of the branches in the acinus as follow,

$$l_A = l_{G-1} = l_0 h^{G-1}.$$

Thanks to this formula, the allometric scaling law for l_A is easily computed. Indeed we know that,

$$\frac{l_A}{r_A} = \frac{l_0 h^{G-1}}{r_0 h^{G-1}} = \frac{l_0}{r_0}.$$

Since the law for l_0, r_0 and r_A are known, we obtain,

$$l_A \propto M^{-\frac{1}{24}}.$$

We suppose in our case that the number of generations in the acinus H is independant on the mass of the mammals [93, 45]. The last allometric scaling law for the morphometric parameters left to define is the law for the amount of exchange surface per unit of alveolar duct surface ϱ_s. First the total lung's exchange surface S_A can be defined as the product of the number of alveoli $n_A \propto M^{3/4}$ [117] and the surface of an alveolus s_A. We suppose that an alveolus is a half-sphere, hence its surface is $s_A = 2\pi r_A^2$. Since we know the law for the radius of the alveolus r_A, we have the law for the surface $s_A \propto M^{1/6}$. The total lung's exchange surface is then $S_A \propto M^{11/12}$ [117]. Second, in our model, a branch in an acinus has a surface

$$s_{\text{ad}} = 2\pi r_A l_A \propto M^{\frac{1}{24}}.$$

The total surface of the alveolar ducts in the idealised lung is then

$$S_{\mathrm{ad}} = 2^G \sum_{k=0}^{H-1} 2^k s_{\mathrm{ad}} = 2^G(2^H - 1)s_{ad} \propto M^{\frac{11}{12}}.$$

Since H is independant on the mass of the animal, the amount of exchange surface per unit of alveolar duct surface,

$$\varrho_s = S_A / S_{\mathrm{ad}} \propto M^0.$$

We defined in chapter 3, the oxygen saturation of hemoglobin in the blood and we modelled this function using the following Hill equation (see Figure 3.10) [50],

$$f(x) = \frac{x^{2.6}}{x^{2.6} + 26^{2.6}}.$$

The variable P_{50} which represents the oxygen partial pressure for which the oxygen saturation of hemoglobin is 50% is an interesting parameter that express the O_2 affinity of the blood. This parameter is dependant on the mass of the mammals and follows an allometric scaling law with an exponent of $-\frac{1}{12}$ [117]. We extend the oxygen saturation in the blood to all mammals by shifting the function on order to obtain the correct oxygen partial pressure at 50 % saturation.

Finally, we recall the formula of the power that we want to minimize,

$$\mathcal{P}(A, T) = \frac{A^2 S_0^2 T}{2\pi^2 C} \left(1 + \frac{\pi^2}{2T} RC\right).$$

The hydrodynamic resistance R and the compliance C are two parameters essential for our optimization. The allometric scaling law for the resistance is already known, we have [117],

$$R \propto M^{-\frac{3}{4}}.$$

The compliance is defined as the ratio between the change in volume of the lung, i.e. the tidal volume ($V_T \propto M^1$) and the change in transpulmonary pressure which we approximate with a change in pleural pressure ($P_{\mathrm{pl}} \propto M^0$ [98]). Then, we can deduce an allometric scaling law for the compliance,

$$C \propto M^1.$$

This exponent is in agreement with the physiological data from [101]. All the allometric scaling laws previously described are summarize in Table 4.5.

4.3.2 Optimal allometric scaling laws

Our analysis explores a set of masses ranging from the mouse (20 grams) to the elephant (5 tons) under three regimes: basal metabolic rate (BMR), field metabolic rate (FMR) and maximal metabolic rate (MMR). The basal metabolic rate corresponds to a resting rate. The field metabolic rate corresponds to an intermediary rate, it

Variables	Exponent		Prefactor
	Predicted [117]	Observed	
Lung volume	1	1.06 [101]	53.5 mL [101]
Tracheal radius	3/8	0.39 [106]	1.83 mm*
Tracheal length	1/4	0.27 [106]	1.87 cm*
Radius of alveolar ducts	1/12	0.13 [107]	0.16 mm*
Length of alveolar ducts	-1/24	N.D.	1.6 mm*
Number of alveoli	3/4	N.D.	19 800 000*
Tidal volume (rest)	1	1.041 [117]	7.69 mL [101]
O_2 affinity of blood	-1/12	-0.089 [27]	37.05 mmHg*
Total resistance	-3/4	-0.70 [101]	$18\ \mathrm{mmHg \cdot s \cdot L^{-1}}$ [101]
Total compliance	1	1.04 [101]	$2.12\ \mathrm{mL \cdot mmHg^{-1}}$ [101]
Interpleural pressure	0	0.004 [44]	N.D.

Table 4.5: Predicted and observed/computed values of allometric exponents for variables of the mammalian respiratory system. *: Prefactor computed using human values (M = 70 kg) at rest. N.D.: No data found.

represents the mean energy spent during our everyday life : walking, foraging ... Finally the maximal metabolic rate represents the maximal energy spending, $\dot{V}_{O_2}^{\max}$. The amount of carbon dioxide removed from the blood by the lung is not detailed in the literature for all mammals. This is why we only use in our computations the oxygen flow exchanged with the blood.

The power $\mathcal{P}(A,T)$ is optimized with the constraint $f_{O_2}(A,T) = \dot{V}_{O_2}$. We need to define the desired flow for the three rates. At BMR, we have the following law [58, 86],

$$\dot{V}_{O_2}^{\mathrm{BMR}} = 9.92 \times 10^{-3}\, M^{\frac{3}{4}}\ \mathrm{L \cdot min^{-1}}.$$

The prefactor is computed using the human value at rest.

At FMR, the allometric scaling law [52] is,

$$\dot{V}_{O_2}^{\mathrm{FMR}} = 2.4 \times 10^{-2}\, M^{0.64}\ \mathrm{L \cdot min^{-1}}.$$

We also found the prefactor using the human value, $\dot{V}_{O_2}^{\mathrm{FMR}} = 0.58\,\mathrm{L \cdot min^{-1}}$ [79]. It represents an intensity of around 20 % of $\dot{V}_{O_2}^{\max}$ for humans.

Finally, at MMR the allometric scaling law is [116],

$$\dot{V}_{O_2}^{\max} = 1.18 \times 10^{-1}\, M^{\frac{7}{8}}\ \mathrm{L \cdot min^{-1}}.$$

When we modify the intensity of the exercise, we also modify the radius of the trachea and the velocity of the blood as explained in the previous section. There are different laws for the three rates. The allometric scaling laws for the tracheal radius keep the same exponent but the prefactor is modified. It is computed using human values. We know that for human, the oxygen flow at FMR is about 20% of $\dot{V}_{O_2}^{\max}$, and we interpolate the values taken in [26] to obtain a radius of 0.93 cm.

$$r_0^{\mathrm{BMR}} = 1.83 \times 10^{-3}\, M^{\frac{3}{8}}\,\mathrm{m},$$

$$\begin{aligned} r_0^{\mathrm{FMR}} &= 1.89 \times 10^{-3}\, M^{\frac{3}{8}}\,\mathrm{m}, \\ r_0^{\mathrm{MMR}} &= 2.58 \times 10^{-3}\, M^{\frac{3}{8}}\,\mathrm{m}. \end{aligned}$$

The blood velocity is computed as the ratio of the length of the capillary l_c over the transit time in the capillary t_c. We assume that the length of the capillary l_c is not dependant on the mass of the mammals and is a constant, as in [117]. It is chosen to be 1 mm. However the transit time in capillaries depends on the metabolic regime but also on the mammal's mass. No data is available in the literature for the field metabolic rate, so we can compute the prefactor using the human value $t_c = 0.78$ s computed by interpolation of data from [47]. Since the exponent of the allometric laws for the field metabolic rate is not known, we chose to take the same as the one for the basal metabolic rate. We finally obtain,

$$\begin{aligned} t_c^{\mathrm{BMR}} &= 0.35\, M^{\frac{1}{4}}\ \mathrm{s}\ [47,\ 117], \\ t_c^{\mathrm{FMR}} &= 0.27\, M^{\frac{1}{4}}\ \mathrm{s}, \\ t_c^{\mathrm{MMR}} &= 0.25\, M^{0.165}\ \mathrm{s}\ [12,\ 47]. \end{aligned}$$

Allometric scaling laws of breathing rates and tidal volumes

Our model predicts that the optimal ventilation follows allometric scaling laws in the three regimes, as shown in Figure 4.11.

$$\begin{array}{l} \text{At } \dot{V}_{O_2}^{\mathrm{BMR}}: \\ f_b^{\mathrm{BMR}} \simeq 0.71\ M^{-0.29}\ \mathrm{Hz}, \quad V_T^{\mathrm{BMR}} \simeq 5.7\ M^{1.05}\ \mathrm{mL}, \\ \text{at } \dot{V}_{O_2}^{\mathrm{FMR}}: \\ f_b^{\mathrm{FMR}} \simeq 1.39\ M^{-0.32}\ \mathrm{Hz}, \quad V_T^{\mathrm{FMR}} \simeq 9.4\ M^{0.98}\ \mathrm{mL}, \\ \text{at } \dot{V}_{O_2}^{\max}: \\ f_b^{\mathrm{MMR}} \simeq 2.05\ M^{-0.15}\ \mathrm{Hz}, \quad V_T^{\mathrm{MMR}} \simeq 21\ M^{1.04}\ \mathrm{mL}. \end{array}$$

Our predicted laws are close to the ones observed in physiology. Indeed at BMR, breathing frequency has been estimated in the physiology to follow the law [101],

$$f_b^{\mathrm{BMR}} = 0.89 M^{-0.26}\,\mathrm{Hz},$$

and tidal volume to follow the law [101],

$$V_T^{\mathrm{BMR}} = 7.7 M^{1.04}\,\mathrm{L}.$$

For the other rates, less data are available in the literature. We only have the law at MMR for the breathing frequency [122],

$$f_b^{\mathrm{MMR}} \simeq 5.08 M^{-0.14}\,\mathrm{Hz}.$$

A larger dead volume at exercise [47] makes the oxygen source for diffusion slower to deplete. This might lead to a decrease in the optimal breathing rate, depending on how the need of oxygen is increased. As a consequence, for small mammals, our

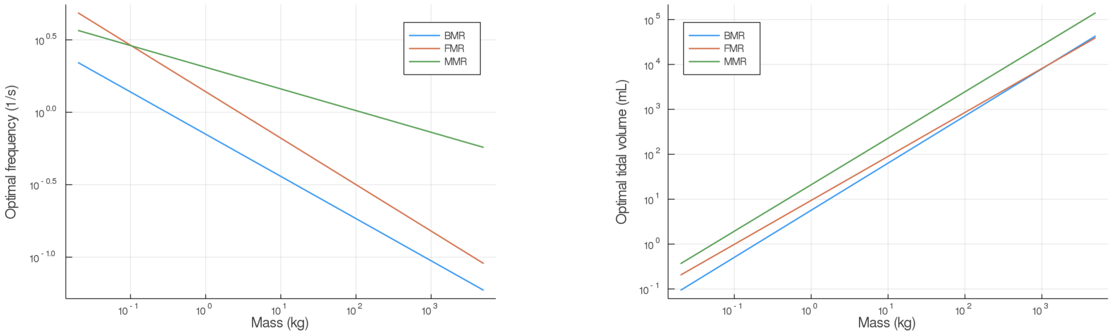

Figure 4.11: Predicted breathing frequency (left) and tidal volume (right) as a function of the mammals' mass (log-log) for three different rates, the basal metabolic rate (BMR), the field metabolic rate (FMR) and the maximal metabolic rate (MMR).

model predicts breathing frequencies at MMR smaller than breathing frequencies at FMR.

These results are only slightly sensitive to the allometric scaling law of the blood residence time in the pulmonary capillaries. Indeed we performed a sensibility analysis on this parameter. We increased and decreased of 30% the exponent of the law at FMR, our predicted laws for the breathing frequency and the tidal volume were only modified by 0.1%. It supports our trust in our results.

In our work, we suppose that the hydrodynamic resistance is independant on the ventilation regime. However if we neglect the increased inertia and turbulence in the bronchi at MMR, the change in dead volume at this regime leads the hydrodynamic resistance to be decreased by a factor 4. In this case, the corresponding exponent for breathing rate goes to -0.13. Even with a important change in resistance, the exponent of the law for breathing frequency does not have a significative change. Since we do not really know how the increased inertia and turbulence can compensate the increase in dead volume and since our predicted laws are not extremely sensitive to resistance, we can assume that taking the hydrodynamic resistance independent on the ventilation regime is a good enough approximation.

Exhaled oxygen fraction

The oxygen flow captured by the lung is a proportion of the air flow inhaled,

$$\dot{V}_{O_2} = \dot{V}_E \, (f_I - f_E),$$

with $\dot{V}_E = V_T f_b$ the air flow rate, f_I the oxygen fraction in ambiant air and f_E the mean exhaled oxygen fraction. Our model can predict the allometric laws for the drop in oxygen fraction between ambiant and exhaled air denoted $\Delta f = f_I - f_E$. We obtain for our three regimes the following laws,

$$\begin{aligned}
\Delta f^{\mathrm{BMR}} &= 3.60 \; M^{0.02} \, \%, \\
\Delta f^{\mathrm{FMR}} &= 4.42 \; M^{-0.006} \, \%, \\
\Delta f^{\mathrm{MMR}} &= 4.47 \; M^{0.008} \, \%.
\end{aligned}$$

The drop in oxygen fraction depends only slightly on the mass and is in the range 3 to 5%, whatever the ventilation regime. Since the inhaled oxygen fraction in air is about 21 %, the oxygen fraction in the exhaled air is between 16 and 18 %, in full accordance with the the physiology [113]. Let us define the quantity $\eta = \Delta f / f_I$, it represents the efficiency of oxygen extraction by the lung. Our model suggests that the optimal value is around 20 %. Since the exponent for all regimes are not exactly zero we obtain some differences between small and large mammals. These differences could be explained by the simplications made in our model.

Transition between convection and diffusion

The localization of the transition between convective and diffusive transports can be estimated by the analysis of the variations with the mass of the Péclet number, through the generations. This number arises by writing the transport equations in their dimensionless form. Let us recall the adimensionalized equation for our transport model explained in the previous chapter,

$$\lambda_i \frac{\partial P_i}{\partial s} - \frac{\partial^2 P_i}{\partial y^2} + Pe_i \frac{\partial P_i}{\partial y} + \zeta_i (P_i - P_{\text{blood}}) = 0,$$

where,

$$\lambda_i = \frac{l_i^2}{D\tilde{T}} \quad Pe_i = \frac{l_i u_i}{D} \quad \zeta_i = \frac{\beta_i l_i^2}{D}.$$

The air flow velocity in generation $i \in [\![0, N]\!]$, where $N+1$ is the number of generations in the lung, is computed as follow,

$$\begin{cases} u_i(t) = \left(\dfrac{1}{2h^2}\right)^i u_0(t), & \text{for } i \in [\![0, G-1]\!], \\ u_i(t) = \dfrac{u_{G-1}}{2^{i-G+1}}, & \text{for } i \in [\![G, N]\!], \end{cases}$$

where $u_0(t)$ is,

$$u_0(t) = A \sin\left(\frac{2\pi}{T} t\right).$$

The mean Péclet number over a half breath is then, for $i < G$,

$$\bar{\text{Pe}}_i = \frac{2}{T} \int_0^{T/2} Pe_i(t) \mathrm{d}t = \frac{2 V_T f_b l_0}{\pi r_0^2 D} \left(\frac{1}{2h}\right)^i,$$

and for $i \geqslant G$,

$$\bar{\text{Pe}}_i = \frac{2}{T} \int_0^{T/2} Pe_i(t) \mathrm{d}t = \frac{2 V_T f_b l_0}{\pi r_0^2 D} \left(\frac{1}{2h}\right)^{G-1} \left(\frac{1}{2}\right)^{i-G+1}.$$

The localization of the transition zone is reached when $\bar{\text{Pe}}_i$ becomes smaller than one over the ventilation cycle. We suppose that the transition occurs at the generation k, it means that we have,

$$\bar{\text{Pe}}_k = 1.$$

If this generation k is in the conductive tree, we then have,

$$2^k = \left(\frac{2V_T l_0 f_b}{\pi r_0^2 D}\right)^{\frac{3}{2}} = \left(2\dot{V}_E \frac{l_0}{\pi r_0^2 D}\right)^{\frac{3}{2}} \propto \dot{V}_E^{\frac{3}{2}} \times M^{-\frac{3}{4}}.$$

However if the generation k is in the acinus, we obtain,

$$2^k = \frac{2V_T l_0 f_b}{\pi r_0^2 D}\left(2^{G-1}\right)^{\frac{1}{3}} = 2\dot{V}_E \frac{l_0}{\pi r_0^2 D}\left(2^{G-1}\right)^{\frac{1}{3}} \propto \dot{V}_E \times M^{-\frac{5}{24}}.$$

We can observe on Figure 4.12 that at rest the localization of the transition zone between convection and diffusion is in the convective tree for large mammals (mass superior to 160 kg) and in the acini for smaller mammals. Hence, we obtain two allometric scaling laws at rest. For large mammals, we have $2^{k_r} \propto M^{0.39}$ and for smaller animals we obtain, $2^{k_r} \propto M^{0.55}$. At maximal exercise, the transition between convection and diffusion happens to be deeper in the lung than at rest. It is located in the acini for all our selection of mammals. We then have only one allometric scaling law, $2^{k_e} \propto M^{0.68}$. Hence, the transition generation k can be localized relatively to the generation of the terminal bronchioles $G-1$. At rest we have,

$$k_r = G - 1 + 3.57 - 0.49\ \log(M)/\log(2),\ \text{for } M \geqslant 160\,\text{kg},$$
$$k_r = G - 1 + 2.38 - 0.3252\ \log(M)/\log(2),\ \text{for } M \leqslant 160\,\text{kg}.$$

At maximal exercise, we obtain,

$$k_e = G - 1 + 4.81 - 0.1977\ \log(M)/\log(2).$$

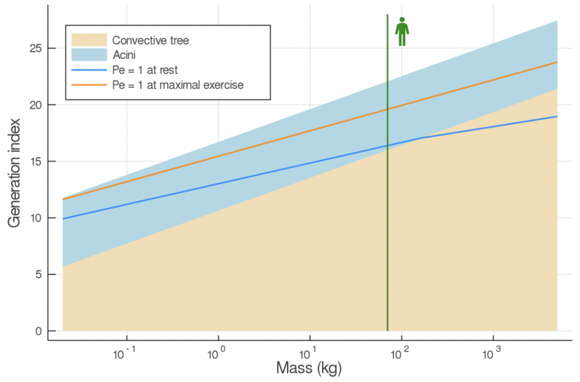

Figure 4.12: Localization of the transition between a convective and diffusive transport of the oxygen in the lung as a function of the animal's mass (logarithmic scale). This localization is predicted by our model that minimizes the power $\mathcal{P}(A, T)$. The lines correspond to the localizations of this transition at BMR (rest, blue line) and MMR ($\dot{V}_{O_2}^{\max}$, orange line). The vertical green line corresponds to human's mass (70 kg). The lower beige region corresponds to the convective zone of the lung, while the upper blue region corresponds to the exchange surface (acini).

Depending on the localization in the lung of the transition between convection and diffusion, an exchange surface in the acini can be only partly active. Indeed if this transition is made at the entrance of the acini, like for humans at rest, only the first generations of the acini have an oxygen concentration high enough to create a significant oxygen flow to the blood. This phenomenon is called the screening effect [95]. The oxygen diffuses but is quickly absorbed by the bronchi walls so that there is little oxygen in the last generations of the acinus. Our model predicts that small mammals use almost all their available exchange surface at rest, with low screening effect. However the localization of the transition between convection and diffusion for large mammals at rest happens to be at the end of the bronchial tree, with strong screening effect. They have a clear difference in term of volume usage between rest and exercise. The difference can be explained by the fact that large mammals needs less oxygen relatively to their mass than small mammals, as the exponent of the allometric law of $\dot{V}_{O_2}/M$ is negative for all metabolic regimes. Indeed we have at BMR, $\dot{V}_{O_2}/M \propto M^{-1/4}$ and at MMR, $\dot{V}_{O_2}^{\max}/M \propto M^{-1/8}$.

4.4 Conclusion

We described and studied a model that minimizes the power dissipated during respiration and how it depends on the ventilation parameters. This dissipated power depends on the resistance to the airflow in the bronchi and on the mechanical energy stored in the tissue. The optimization is made assuming that the oxygen flow exchanged with the blood has to fit the body needs.

Our results are close to the physiology for humans and for all mammals, for different metabolisms. This suggests that the control of ventilation is highly dependent on the morphological characteristics of the lung, and helps us to better understand the allometric scaling of its ventilation in mammals. These results might highlight how the evolution may have driven the design of the respiratory system.

This model could be improved in many ways, especially during maximal exercise. Indeed, we know that during intense activity, expiration is no longer a passive action. The contraction of the muscles might induce a supplementary mechanical energy in the tissue at expiration that is not taken into account in our model. Furthermore, we made the assumption that the hydrodynamic resistance is not modified during exercise even though we increased the dead volume. This new resistance should be computed by counterbalancing the increase of the bronchial radius by the augmentation of the inertia and the turbulence due to an higher airflow. Finally, we could improve the model regarding the geometry of the mammals lung. We could take into account the asymmetry of the bifurcations [105, 36] or the different types of branching patterns found in mammals (monopodial, dichotomous, polychotomous) [83].

Sections 2 and 3 were the subjects of two articles. The results presented in the papers are slightly different than the one presented here, since some parameters have been adjusted. However, the conclusions remain the same.

The section 2 of this chapter was the subject of an article published in Frontiers in Physiology. The references are:

Interplay between optimal ventilation and gas transport in a model of the human lung.
F.Noël[1,2], B. Mauroy[1,2],

Frontiers in Physiology, 10:488, 2019.

[1] Laboratoire JA Dieudonné, UMR CNRS 7351, Université Côte d'Azur, Nice, France.
[2] VADER Center, Université Côte d'Azur, Nice, France.

The section 3 of this chapter is the subject of an article that is in prepublication. The references are:

The origin of the allometric scaling of lung's ventilation in mammals.
F.Noël[1,2], C. Karamaoun[1,2], B. Mauroy[1,2],

hal-02567829v2, 2020.

[1] Laboratoire JA Dieudonné, UMR CNRS 7351, Université Côte d'Azur, Nice, France.
[2] VADER Center, Université Côte d'Azur, Nice, France.

Chapter 5

Ventilation of a non-healthy human

In the previous chapters, we considered the human's lung to be one of a young, healthy subject. However, in a lifetime several pulmonary infections can occur. For pathogens, the lung is an organ easy to infiltrate and where to proliferate. Indeed, it is an humid environment, full of oxygen, connected to the ambient air through the mouth and the nose. Once in the lung, the development of an infection induces an inflammation in the bronchi. This reaction allows the tissue to swell in order for the white blood cells of the immune system to converge at the site of infection and to start eliminating the pathogens [68]. The inflammation modifies the geometry of the lung, and hence the distribution of the airflow as well as the ventilation.

Different approaches in the litterature have been used to model the response of the immune system following a pulmonary infection. A first approach is to model the macrophage response after an infection using ordinary differential equations [25] or using models of granulomas development [46, 38, 20] which are macrophage clusters. These types of approaches have the benefit of mimicking the immune response specific to the lung and allows to explore potential treatments. However, even if macrophages are the first responders during a pulmonary infection, these models do not take into account neutrophils present in the blood that are the majority of the leucocytes. A second approach has been to model the inflammatory response in a part of the acinus [89]. This model allows to represent the infection in the whole lung and to model the exchanges with the blood. However, even if this model takes into consideration the swelling of the tissue, it does not represent the pathogen evolution in the lung which is important in order to be able to model different types and speeds of infection.

We choose to use a more global immune response model that is not specific to the lung and that can be used in any organs. This type of models has the benefit of not being specific to a certain virus or a certain bacteria. Nevertheless, simple models with only three [74, 85, 120] or four different variables [90, 18, 77, 31] describe the evolution of tissue damage all along the infection but not the inflammation of the tissue. Hence, we used a more specific, but also more complex model [91] that describes the immune response in the tissue and in the blood, but also the inflammation of the tissue. This last model is then linked to our gas transport model described in the chapter 3 to simulate the propagation of idealized lung infection and inflammation bronchi per bronchi. Our model is generic, it does not focus on one

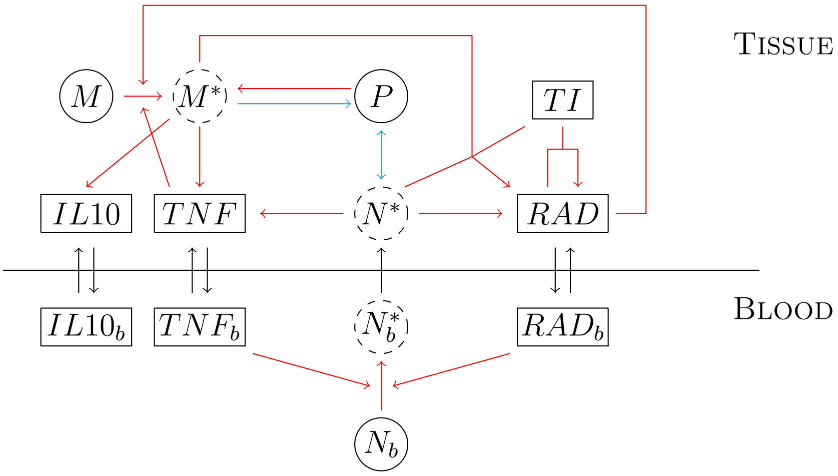

Figure 5.1: Interactions of the immune system and the pathogen. Diffusion is represented by black arrows, up-regulation of immune interactions by red arrows and down-regulation of immune interactions by blue arrows. Reproduced from [91].

pathogen only. In this explorative model, we study different stages of the infection and how the exchanges with the blood are affected by the altered lung's geometry arising from the inflammation of its airways.

5.1 Infection model

The surface barriers are the first defenses of the innate immune system. In the lung, they consist in the mucus and in the ciliated cells [32]. We focus in this chapter on the second defense of the innate immune system that responds once a pathogen has breached the barriers. It is composed of chemicals and white blood cells, which are also called leucocytes [68].

5.1.1 Inflammation of the bronchi

We choose to model an infection in the lung by using an existing model representing the response of the immune system in a human organ and its interplay with the blood [91]. It describes the evolution of several variables that represent the response of the immune system in the tissue and in the blood, as shown in Figure 5.1.

When the body detects a pathogen in the tissues (P) or in the blood (P_b), the first reaction of the immune system is to bring white blood cells (here macrophages and neutrophils) to the site of infection. When resting macrophages (M), already present in the tissue, come in contact with some pathogens, they become activated (M^*). Then, they can eliminate the pathogens and produce pro-inflammatory (TNF) and anti-inflammatory ($IL10$) cytokines. Pro-inflammatory cytokines migrate into the blood (TNF_b) and send a signal to resting neutrophils (N_b) already present in the blood. Once the signal is received by the neutrophils, they become activated (N_b^*). These activated neutrophils have the ability to go into the tissue (N^*) and to fight the pathogens. Furthermore, during this infection, the tissue becomes inflamed (Z) and the presence of radicals (RAD and RAD_b) produced by activated macrophages and neutrophils, can damage the tissue that becomes less functional (TI). This immune response can be modeled by ordinary differential equations and the values and the descriptions of all parameters used are detailed in Annexe B. All these equations and parameters come from [91].

First, let us tackle the pathogens equations:

$$\begin{aligned}\frac{dP}{dt} =& k_{pg}P\left(1-\frac{P}{P_\infty}\right)-\frac{s_b k_{pb}P}{\mu_b+k_{bp}P}-k_{pm}g_i(M^*)g(P,x_{m*p},h_{m*p})\\ &-k_{pn}g_{in}(N^*)g(P,x_{n*p},h_{n*p})+d_p(Z)\frac{d_{pb}(P_b)-d_{pt}(P)}{V_T}\\ \frac{dP_b}{dt} =& k_{pbg}P_b\left(1-\frac{P_b}{P_{b\infty}}\right)-\frac{s_{bb}k_{pbb}P_b}{\mu_{bb}+k_{bbp}P_b}\\ &-k_{pnb}g_{ib}(N_b^*)g(P_b,x_{n*pb},h_{n*pb})+d_p(Z)\frac{d_{pt}(P)-d_{pb}(P_b)}{V_B}.\end{aligned} \tag{5.1}$$

The first term in the equations represent the logistic growth of the pathogens in the tissue and in the blood. The pathogens are first destroyed by the macrophages already present on the site of infection which is modeled by the second term in the equations. The pathogens in the tissue are also eliminated by activated macrophages, a mechanism which is modeled by the third term in the first equation. However, the presence of anti-inflammatory cytokines ($IL10$) affects their ability to deplete pathogens, which is modeled by the following inhibition function,

$$g_i(x) = x\left(\frac{1-c_i}{1+\left(\frac{IL10}{IL10_\infty}\right)^{h_i}}+c_i\right).$$

Furthermore, the macrophages can eliminate the pathogens up to a maximal rate, which is modeled by an Hill function that has a sigmoid variation,

$$g(v,x,h) = \frac{v^h}{v^h+x^h}.$$

The pathogens can also be eliminated by the activated neutrophils, a mechanism which is modeled by the second to last term. As for the activated macrophages, $IL10$ affects the ability of the activated neutrophils to deplete pathogens, which is modeled by an inhibition function in the tissue,

$$g_{in}(x) = x\left(\frac{1-c_{in}}{1+\left(\frac{IL10}{IL10_{n\infty}}\right)^{h_{in}}}+c_{in}\right),$$

and in the blood,

$$g_{ib}(x) = x\left(\frac{1-c_{ib}}{1+\left(\frac{IL10_b}{IL10_{b\infty}}\right)^{h_{ib}}} + c_{ib}\right),$$

Finally the last term of the equations (5.1) represents the diffusion of the pathogens. The diffusion depends linearly on the inflammation (Z),

$$d_p(Z) = d_{bp}(1 + d_{fp}Z).$$

Furthermore, the pathogens in the tissues form colonies at high concentration. The diffusion is then dependent on the surface area of the population. The diffusion of the pathogens is then modeled by,

$$d_{pb}(P_b) = a_b P_b, \text{ and } d_{pt}(P) = \frac{a_t P^{2/3}}{1 + b_t P^{1/3}}.$$

Now, let us focus on the macrophages equations,

$$\begin{aligned}
\frac{dM}{dt} &= s_m - \mu_m M - k_{mp} g_i(M) g(P, x_{mp}, h_{mp}) \\
&\quad - k_{mtcell} g_i(M) g(TNF, x_t, h_t) - k_{mrcell} g_i(M) RAD, \\
\frac{dM^*}{dt} &= -\mu_{m*} M^* + k_{mp} g_i(M) g(P, x_{mp}, h_{mp}) \\
&\quad + k_{mtcell} g_i(M) g(TNF, x_t, h_t) + k_{mrcell} g_i(M) RAD.
\end{aligned} \tag{5.2}$$

The first terms represent the source (s_m) and the death (μ_m) of the macrophages. Indeed, only resting macrophages (M) are provided by the organism. The next terms model the activation of the macrophages when in contact with pathogens, with the pro-inflammatory cytokine (TNF) and with radicals (RAD).

Likewise, let us define the equations for the neutrophils in the blood,

$$\begin{aligned}
\frac{dN_b}{dt} &= s_{nb} - \mu_{nb} N_b + k_{snb} g(cN_b^* + dN^*, x_{snb}, h_{snb}) \\
&\quad - k_{npbcell} g_{ib}(N_b) g(P_b, x_{npb}, h_{npb}) \\
&\quad - k_{ntcell} g_{ib}(N_b) g(TNF_b, x_{tb}, h_{tb}) - k_{nrb} g_{ib}(N_b) RAD_b, \\
\frac{dN_b^*}{dt} &= -\mu_{nb*} N_b^* + k_{npb} g_{ib}(N_b) g(P_b, x_{npb}, h_{npb}) \\
&\quad + k_{ntcell} g_{ib}(N_b) g(TNF_b, x_{tb}, h_{tb}) + k_{nrb} g_{ib}(N_b) RAD_b \\
&\quad - (1 - r_b) k_{pncell} g_{ib}(N_b^*) g(P_b, x_{n*pb}, h_{n*pb}) - \frac{d_n(Z) N_b^*}{V_B}.
\end{aligned} \tag{5.3}$$

As for the macrophages, the first terms represent the source (s_{nb}) and the death (μ_{nb}) of the neutrophils. However, we also assume that the increase of inflammation increases the source of neutrophils. This phenomenon is modeled by the third term of the equation. This term depends on the resting neutrophils (N_b) in the blood through the non linear function g, which is itself depending on the number of activated neutrophils in the blood and in the tissue. As for the macrophages, the neutrophils are activated when in contact with the pathogens (P_b), with the pro-inflammatory cytokine (TNF_b) and with the radicals (RAD_b). Furthermore, activated neutrophils can be depleted during the elimination of pathogens, a mechanism which is modeled by the second to last term in the N_b^* equation. Finally, the last term of the N_b^* equation represents the fact that activated neutrophils can diffuse into the tissue. Diffusion is modeled thanks to a linear function with the inflammation (Z),

$$d_n(Z) = d_{bn}(1 + d_{fn}Z).$$

The equation for the activated neutrophils in the blood writes,

$$\frac{dN^*}{dt} = -\mu_{n*}N^* - (1-r)k_{pncell}g_{in}(N^*)g(P, x_{n*p}, h_{n*p}) + \frac{d_n(Z)N_b^*}{V_T}. \tag{5.4}$$

As for the activated neutrophils in the blood, the equation takes into account the death of the neutrophils, their depletion when eliminating the pathogens and the diffusion of the cells.

Let us now focus on the pro-inflammatory cytokines (TNF),

$$\begin{aligned} \frac{dTNF}{dt} =& -\mu_t TNF - k_{mtmol}g_i(M)g(TNF, x_t, h_t) \\ &+ \frac{d_{mol}(Z)(TNF_b - TNF)}{V_T} + k_{mat}g_{it}(g(M^*, x_{m*t}, h_{m*t})), \\ \frac{dTNF_b}{dt} =& -\mu_{tb}TNF_b - k_{ntmol}g_{ib}(N_b)g(TNF_b, x_{tb}, h_{tb}) \\ &- \frac{d_{mol}(Z)(TNF - TNF_b)}{V_B}. \end{aligned} \tag{5.5}$$

The first term of the equations represents the decay of the cytokines. Then, the second term models the binding of TNF to resting macrophages that causes the activation of the macrophages. The third term represents the diffusion of the cytokines between the tissue and the blood thanks to a linear function,

$$d_{mol}(Z) = d_{bmol}(1 + d_{fmol}Z).$$

The last term in the equation of TNF in the tissue represents the production of TNF by the activated macrophages. It is modeled thanks to the following inhibition function,

$$g_{it}(x) = x\left(\frac{1 - c_{it}}{1 + \left(\frac{IL10}{IL10_{t\infty}}\right)^{h_{it}}} + c_{it}\right).$$

The anti-inflammatory cytokines ($IL10$) equations write,

$$\begin{aligned}
\frac{dIL10}{dt} =& (-\mu_{imax} + (\mu_{imax} - \mu_{imin}) g(IL10, x_i, h_i)) IL10 \\
&+ \frac{d_{mol}(Z)(IL10_b - IL10)}{V_T} + k_{mai} g_i(g(M^*, x_{m*i}, h_{m*i})), \\
\frac{dIL10_b}{dt} =& (-\mu_{ibmax} + (\mu_{ibmax} - \mu_{ibmin}) g(IL10_b, x_i, h_i)) IL10_b \\
&+ \frac{d_{mol}(Z)(IL10 - IL10_b)}{V_B}.
\end{aligned} \tag{5.6}$$

The first term of the equations represents the decay rate of the cytokines by assuming that the decay rate is minimum when the $IL10$ concentration is at its maximum. Then, as for the pro-inflammatory cytokines, the equations take into account the diffusion between the tissue and the blood of the molecules and the production of $IL10$ by the activated macrophages.

Now we focus on the radicals (RAD) equations,

$$\begin{aligned}
\frac{dRAD}{dt} =& -\mu_r RAD + \frac{d_{mol}(Z)(RAD_b - RAD)}{V_T} + k_{nar} g_{in}(N^*) \\
&+ k_{natr} N^* TI + k_{rntp} N^* PTI + k_{rtmp} M^* PTI \\
&+ k_{rtr} RAD\, TI \\
\frac{dRAD_b}{dt} =& -\mu_{rb} RAD_b + k_{narb} g_{inb}(N_b^*) + \frac{d_{mol}(Z)(RAD - RAD_b)}{V_B}.
\end{aligned} \tag{5.7}$$

The first two terms of the equations represent the death of the radicals, and their diffusion between the blood and the tissue. The next terms model the production of radicals (RAD). First, they are released by the activated neutrophils in the tissue and in the blood where the inhibition function for the neutrophils in the blood writes,

$$g_{inb}(x) = x \left(\frac{1 - c_{inb}}{1 + \left(\frac{IL10}{IL10_{nb\infty}}\right)^{h_{inb}}} + c_{inb} \right).$$

The radicals in the tissue are also produced by tissue damage (TI). Indeed, activated neutrophils cause tissue damage that releases radicals. Then, activated neutrophils and activated macrophages damage the tissue while eliminating pathogens. Hence, this also also releases radicals. Finally, radicals themselves are causing damage to the tissue, *i.e.* they increase their own concentration.

Now let us describe the evolution of the tissue damage with the following equation,

$$\frac{dTI}{dt} = k_{tg} TI \left(1 - \frac{TI}{T_\infty}\right)(TI - a) - k_{rtt} RAD\, TI. \tag{5.8}$$

The tissue damage is assumed to follow a logistic growth, as shown by the first term of the equation. However, when TI falls below a, the tissue is unable to repair itself. Furthermore, the second term represents the fact that TI is depleted once it encounters a radical.

Finally, let us focus on the last variable Z,

$$\frac{dZ}{dt} = k_{tz}\left(g(TNF, x_{tz}, h_{tz}) + k_{zti}(1 - TI)\right)(1 - Z) - \mu_z Z. \tag{5.9}$$

This last variable Z models the evolution of the inflammation. Its growth depends on the level of TNF and on the amount of tissue damage (TI). The last term of the equation depicts the decay of the inflammation.

In our work, we focus on one particular variable of this infection model, the inflammation of the tissue Z. Its values are between 0 (no inflammation) and 1 (maximal inflammation). We suppose that this amount of inflammation can be linked to the evolution of the bronchial volume (V_{br}) during an infection through the following function [89],

$$V_{\text{br}}(Z) = \frac{V_{\text{br, he}}}{1 + m_{vta}Z}, \tag{5.10}$$

where $V_{\text{alv, he}}$ is the volume of the healthy tissue and m_{vta} is a reduction parameter. Its value is chosen to be the same as the one presented in [89]. It is equals to 1. We can link this change of volume to the radius of the bronchus. Indeed, we know that the volume of a bronchus V_i of generation i can be computed as follow,

$$V_i = \pi r_i^2 l_i,$$

with r_i and l_i being respectively the radius and the length of the bronchus. Furthermore, since the length of the bronchus is not modified during an inflammation, we can replace this last expression in the equation (5.10). It leads to,

$$r_i(Z) = \frac{r_{i,\text{he}}}{\sqrt{1 + m_{vta}Z}},$$

where r_i is the inflamed radius and $r_{i,\text{he}}$ is the healthy radius of the bronchus of generation i. Since the radius of the airways are decreasing during inflammation, it implies that the thickness of the bronchi walls is increasing. In particular, the thickness of the alveolar membrane (τ) is computed as follow,

$$\tau_i(Z) = \tau_{i,\text{he}} + r_{i,\text{he}} - r_i(Z),$$

where $\tau_{i,\text{he}} = 1 \times 10^{-6}$ m is the thickness of the alveolar membrane in generation i in a healthy case [95].

We will work with three different outcomes. The first one is a cured outcome where the pathogens are eliminated quickly by the immune system and the tissue recovers after the inflammation and goes back to a healthy state. We obtain this outcome with an initial number of pathogens between 0 and 840 P-units. In our case, we choose an initial number of 500 P-units (Figure 5.2) as in [91]. The second outcome simulated is an aseptic death. In this case, the immune system succeed to remove all the pathogens. However, the immune response is so intense that the tissue does not recover and stays inflamed. This outcome results from an initial number of pathogens between 840 and 1060 P-units. In our case, we choose an initial number of 850 P-units (Figure 5.3) as in [91]. Finally our last outcome is a septic death, where there are too many pathogens for the immune system which fails to cure the infection. This outcome results from an initial number of pathogens superior to 1060 P-units. In our case, we choose an initial number of 1200 P-units (Figure 5.4) as in [91].

5.1.2 Asymmetric transport model

Let us recall that in chapter 3, we defined the transport of oxygen and carbon dioxide in an idealized symmetric dichotomic bifurcating tree with the following equation for each generation $i \in [\![0, N]\!]$, with $N + 1$ being the number of generations in the lung, and for each bronchi $j \in [\![0, 2^i]\!]$

$$\frac{\partial P_{i,j}}{\partial t} - D\frac{\partial^2 P_{i,j}}{\partial x^2} + u_{i,j}(t)\frac{\partial P_{i,j}}{\partial x} + \beta_{i,j}P_{i,j} = \beta_{i,j}P_{\text{blood}}, \qquad \text{for } x \in [0, l_i]. \tag{5.11}$$

However, when inflammation appears in a bronchus, its radius is modified which implies that the correspoding bifurcation is no longer symmetric. Indeed, the sister branch of the inflamed bronchus does not have the same radius anymore (see Figure 5.5).

This asymmetry appears in the bifurcation equation. Indeed, the volumetric flow rate does no longer divide into two similar flow rates. We have,

$$\begin{aligned} S_{i,j}\left(-D\frac{\partial P_{i,j}(l_{i,j},t)}{\partial x} + u_{i,j}(t)P_{i,j}(l_{i,j},t)\right) = \\ S_{i+1,2j}\left(-D\frac{\partial P_{i+1,2j}(0,t)}{\partial x} + u_{i+1,2j}(t)P_{i+1,2j}(0,t)\right) + \\ S_{i+1,2j+1}\left(-D\frac{\partial P_{i+1,2j+1}(0,t)}{\partial x} + u_{i+1,2j+1}(t)P_{i+1,2j+1}(0,t)\right). \end{aligned}$$

However, we still have the conservation of the volumetric flow rate. Let us define $q_{i,j} = u_{i,j}S_{i,j}$, the volumetric flow rate in the bronchus j of generation i, $q_{i+1,2j} = u_{i+1,2j}S_{i+1,2j}$, the volumetric flow rate in one of the branch's daughter and $q_{i+1,2j+1} = u_{i+1,2j+1}S_{i+1,2j+1}$ the volumetric flow rate in the second branch. Then, we obtain,

$$q_{i,j} = q_{i+1,2j} + q_{i+1,2j+1}.$$

Thanks to this equation and the continuity of P_i between successsive generations, we can simplify the bifurcation equation. Then, we obtain,

$$S_{i,j}\frac{\partial P_{i,j}(l_{i,j},t)}{\partial x} = S_{i+1,2j}\frac{\partial P_{i+1,2j}(0,t)}{\partial x} + S_{i+1,2j+1}\frac{\partial P_{i+1,2j+1}(0,t)}{\partial x}. \tag{5.12}$$

Furthermore, with the asymmetry of the lung, the airflows do not divide into two equal values at a bifurcation. In order to compute the airflow velocities in all bronchi, we can suppose that we have the same pressure at the outlets of the tree,

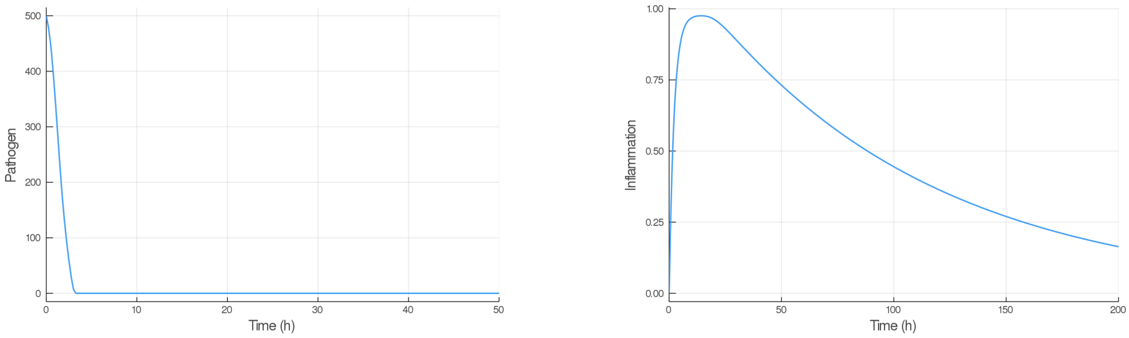

Figure 5.2: Pathogens (left) and inflammation (right) evolution for a cured outcome.

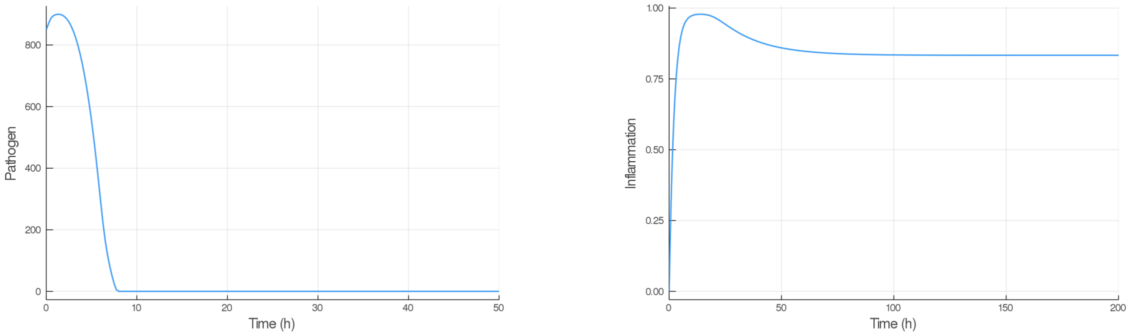

Figure 5.3: Pathogens (left) and inflammation (right) evolution for an aseptic death outcome.

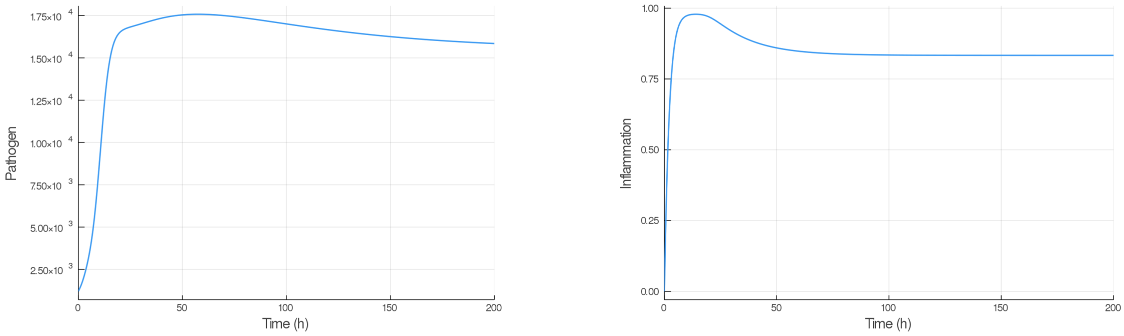

Figure 5.4: Pathogens (left) and inflammation (right) evolution for a septic death outcome

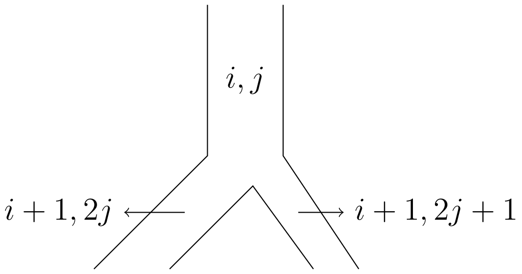

Figure 5.5: Indices of the bronchi in an asymmetric bifurcation.

which implies that the strength provided by the muscles is homogeneous in the whole lung. Furthermore, we also suppose that the viscous energy dissipated by the fluid in the tree is minimized [29]. These assumptions lead to the following equation,

$$\frac{q_{i+1,2j}^2}{E_{i+1,2j}} + \frac{q_{i+1,2j+1}^2}{E_{i+1,2j+1}} = \frac{q_{i,j}^2}{E_{i+1,2j} + E_{i+1,2j+1}},$$

where,

$$E_{i+1,2j} = \frac{l_i}{l_{i+1}} \left(\frac{r_{i+1,2j}}{r_{i,h}} \right)^4 \quad \text{and} \quad E_{i+1,2j+1} = \frac{l_i}{l_{i+1}} \left(\frac{r_{i+1,2j+1}}{r_{i,j}} \right)^4 .$$

We can deduce the volumetric flow rates in the two branch's daughters,

$$q_{i+1,2j} = q_{i,j} \frac{E_{i+1,2j}E_{i+1,2j+1} + E_{i+1,2j}^2}{(E_{i+1,2j} + E_{i+1,2j+1})^2},$$

and

$$q_{i+1,2j+1} = q_{i,j} \frac{E_{i+1,2j}E_{i+1,2j+1} + E_{i+1,2j+1}^2}{(E_{i+1,2j} + E_{i+1,2j+1})^2}.$$

We can observe that if the bronchus of generation i divides into two branches of the same size, *i.e.* $r_{i+1,2j} = r_{i+1,2j+1}$, we then have,

$$q_{i+1,2j} = q_{i+1,2j+1} = \frac{q_{i,j}}{2}.$$

It is in agreement with our computations in chapter 3. The numerical scheme used to compute numerically the approximated solution of equation 5.11 is detailed in appendix A.

Finally, the last aspect changed by the asymmetry is the oxygen and carbon dioxide flows to the blood. We can define the gas flow exchanged with the blood in the generation i, with the following equation,

$$f(A,T) = \sum_{i=G}^{N} \frac{1}{T} \int_{t_C}^{t_C+T} \sum_{k=1}^{2^i} \int_0^{l_i} \gamma_{i,k}(Z) \left(P_i(t,x) - P_{\text{blood}}(t,x) \right) \mathrm{d}x \, \mathrm{d}t,$$

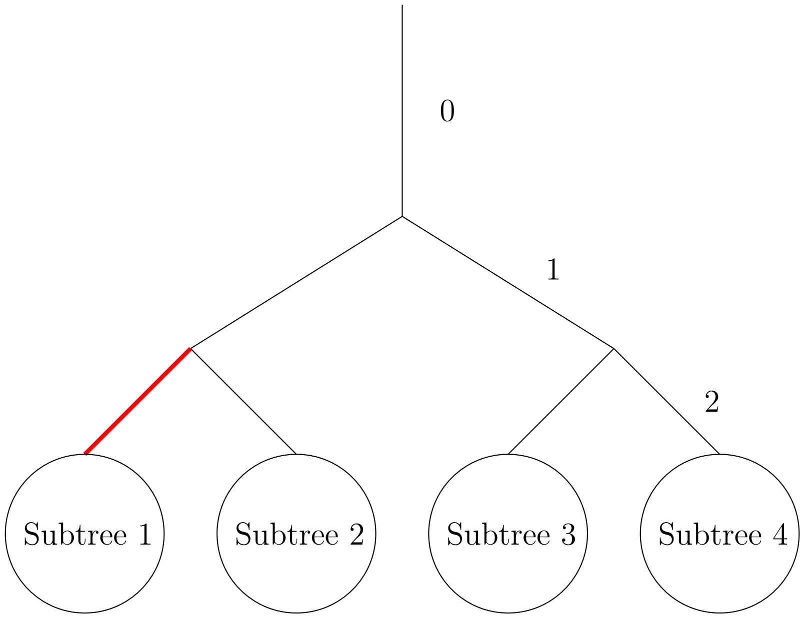

Figure 5.6: Tree model of the lung. The red bronchus represents the infected bronchus and the number on the bronchi represents the generation index.

where A is the amplitude of the ventilation, T is the period of ventilation, G is the number of generations in the conductive tree, $N+1$ is the number of generations in the lung, t_C a time at which the system has reached a periodic regime and

$$\gamma_{i,k}(Z) = 2\pi r_{i,k}(Z)\alpha_{i,k}(Z)\varrho_s.$$

$r_{i,k}(Z)$ is the radius of the number k bronchus of generation i. α_i is the permeability of the alveolar membrane, it writes,

$$\alpha_{i,k} = \frac{D_{gas,H_2O}\sigma_{gas,H_2O}}{\tau_{i,k}(Z)},$$

where D_{gas,H_2O} is the diffusion coefficient of the gas in water ($\mathrm{m}^2 \cdot \mathrm{s}^{-1}$), σ_{gas,H_2O} is the solubility coefficient ($\mathrm{mol} \cdot \mathrm{m}^{-3} \cdot \mathrm{mmHg}^{-1}$) of the gas in water and $\tau_{i,k}(Z)$ is the thickness (m) of the alveolar membrane in the number k bronchus of generation i. ϱ_s is the amount of exchange surface per unit of alveolar duct surface. It was previously defined in chapter 3.

5.2 One branch infection

Let us start by assuming that we have only one bronchus infected in the lung. We suppose that we have a cured outcome (Figure 5.2) and that the infection does not spread to the other bronchi. We suppose that the infected bronchus belongs to the third generation (index 2). We define four subtrees coming from each bronchi of the third generation, see Figure 5.6.

5.2.1 Constant ventilation parameters

First, let us assume that the ventilation is exactly the same as the healthy case. Then, we impose a ventilation amplitude of $1.2\,\mathrm{m}\cdot\mathrm{s}^{-1}$ and a ventilation period of 5 s at rest. During maximal exercise, we suppose that the ventilation amplitude is $19\,\mathrm{m}\cdot\mathrm{s}^{-1}$ and the ventilation period is $1\,\mathrm{s}$.

At rest, an interesting phenomenon appears, when only one bronchus is infected more oxygen is exchanged with the blood than when the bronchus is healthy, see Figure 5.7. It can be explained by the distribution of oxygen in the generations. Indeed, we can observe that, in the subtree 2, the air flow goes deeper into the lung. It allows the oxygen to meet a larger exchange surface and hence to counterbalance the low oxygen flow in the subtree coming from the infected bronchus.

We observe a major difference between the resting regime and the maximal exercise regime. During maximal exercise, an expected response happens: the decrease of the flow when the radius of the bronchus is lower than the healthy radius, see Figure 5.8. The repartition of the oxygen flow in the blood in each of the four subtrees (Figure 5.8) gives us an indication on this behaviour. We can observe that the flow in the subtree 1 decreases with an higher amplitude that the increase of the flow in the subtree 2. Since in the subtrees 3 and 4, the flow remains constant, this difference of amplitude explains the global decrease of the flow.

We chose to infect a bronchus in the third generation of the lung because of its proximity to the trachea. Indeed, when we infect a bronchus in a deeper generation, there are more and more healthy subtrees that help to counterbalance the lower air flow going through the inflamed bronchus. The offset and hence, the variation of the total oxygen flow to the blood is smaller and smaller as the generation of the inflamed bronchus goes deeper. Consequently, the deeper the generation, the closer the flow exchanged with the blood is to the healthy flow (Figure 5.9).

5.2.2 Constant air pressure at the outlets of the tree

We assumed in the last section that when a bronchus is infected, we have the same ventilation than when we are healthy. This hypothesis might be valid for a single infected bronchus but when the infection spreads and a whole region of the lung is blocked, the ventilation is probably not anymore adapted to the situation.

We now make the assumption that the difference of pressure between the inlet and the outlet of the tree remains constant throughout the inflammation of the bronchi. We know that this difference in pressure ΔP depends on the volumetric flow rate q_0 through the tree and the hydrodynamic resistance R of the tree [29]. It writes,

$$\Delta P(t) = Rq_0(t) = RS_0u_0(t).$$

The hydrodynamic resistance R which represents the difficulty of a fluid to pass through the bronchi, is dependent on the radius of the bronchi. Indeed, we know that the hydrodynamic resistance R_i in a cylinder writes,

$$R_i = \frac{8\mu l_i}{\pi r_i^4},$$

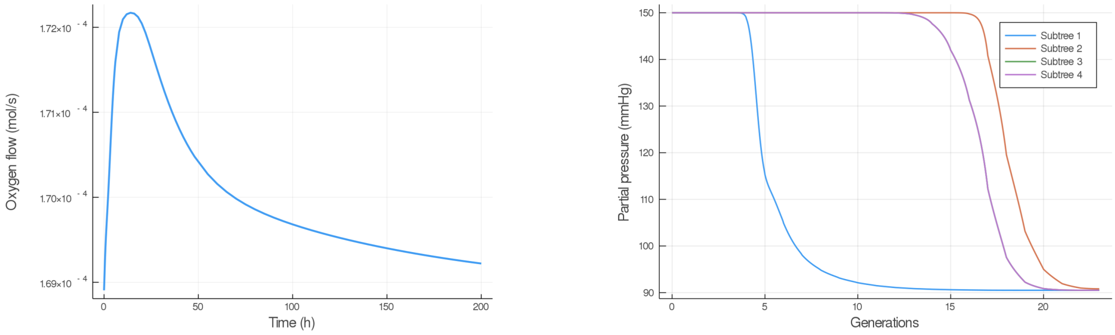

Figure 5.7: Infection of a single bronchus in the third generation at rest. Left: Evolution of the oxygen flow to the blood. Right: Oxygen partial pressure at the inspiration peak during maximal inflammation in each of the four subtrees.

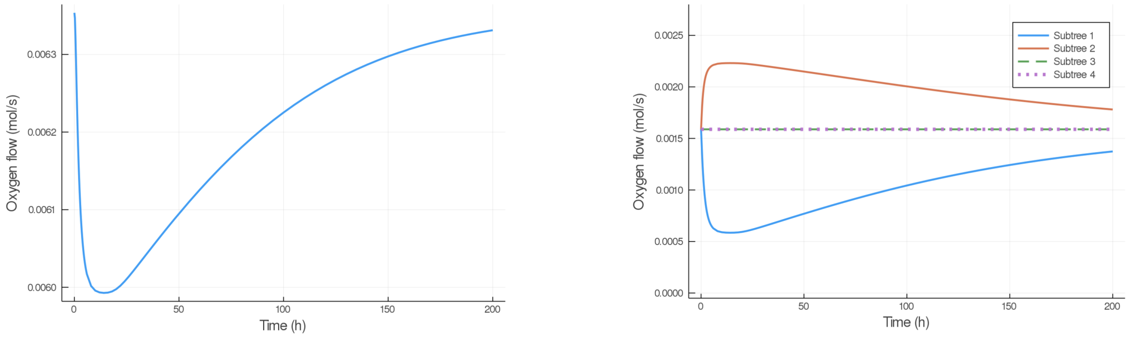

Figure 5.8: Evolution of the oxygen flow to the blood during the infection of a single bronchus in the third generation during maximal exercise. Left: in the whole lung. Right: in each of the four subtrees.

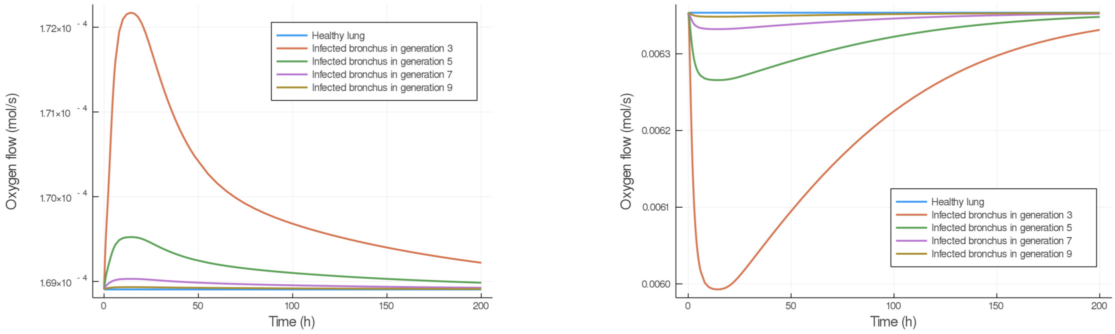

Figure 5.9: Evolution of the oxygen flow to the blood of a single bronchus in several generations at rest (left) and during maximal exercise (right).

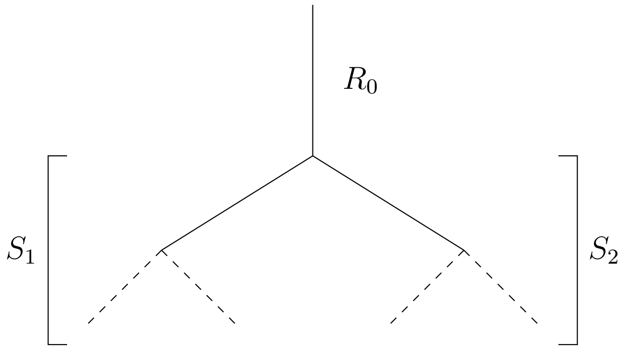

Figure 5.10: Computation of the equivalent resistance of the lung. The subtrees S_1 and S_2 have a resistance of R_1 and R_2 respectively. The total equivalent resistance of the lung is then computed as follow, $R = R_0 + \left(\frac{1}{R_1} + \frac{1}{R_2}\right)^{-1}$.

where l_i is the length of the cylinder, r_i its radius and μ is the viscosity of the fluid. In our case the fluid is the air and its viscoisty is $\mu = 1.8 \times 10^{-5}\,\mathrm{Pa \cdot s}$. Thanks to the resistance expression and the assumption that the lung is just an interlocking of cylinders, we can compute the equivalent hydrodynamic resistance of the whole tree by recurrence, see Figure 5.10. Indeed, the first bronchus of the tree, the trachea, divide into two subtrees S_1 and S_2 which each have a resistance of R_1 and R_2 respectively. The total resistance R of the lung is then,

$$R = R_0 + \left(\frac{1}{R_1} + \frac{1}{R_2}\right)^{-1},$$

with R_0 being the resistance of the trachea. The resistance of the two subtrees S_1 and S_2 is computed the same way and so on. This equivalent resistance neglects the resistance of the bifurcations and the effects of inertia. However, as in chapter 4, we chose to compute the resistance with the formula for the equivalent resistance and to determine the ratio of increase or decrease relatively to the healthy state. Finally, to obtain a coherent resistance we multiply this ratio with the physiological value of the resistance.

We defined in chapter 3 the cross section area $S_0 = \pi r_0^2$ and the velocity of the airflow in the trachea as the following sine function,

$$u_0(t) = A \sin\left(\frac{2\pi}{T} t\right),$$

where A is the ventilation amplitude and T is the ventilation period. Let us denote our variables with a "he" subscript when the bronchus is healthy and with a "inf" subscript when the bronchus is inflamed. Furthermore, we assume that the breathing frequency is the same when healthy or sick.

In this section, we assume that the difference of pressure between the inlet and the outlet of the tree remains constant throughout the inflamamation of the bronchi,

$$\Delta P_{\mathrm{he}}(t) = \Delta P_{\mathrm{inf}}(t).$$

By substituting the values, we obtain,

$$R_{\text{he}}\pi r_{0,\text{he}}^2 A_{\text{he}} \sin\left(\frac{2\pi}{T}t\right) = R_{\text{inf}}\pi r_{0,\text{inf}}^2 A_{\text{inf}} \sin\left(\frac{2\pi}{T}t\right).$$

Finally, the ventilation amplitude when the lung is infected writes,

$$A_{\text{inf}} = A_{\text{he}} \frac{R_{\text{he}}}{R_{\text{inf}}} \frac{r_{0,\text{he}}^2}{r_{0,\text{inf}}^2}.$$

Figure 5.11 depicts the evolution of the ventilation amplitude during the infection of a third generation bronchus at rest and during exercise. We can observe that this evolution is the same for the two regimes, it follows the evolution of the inflammation during the cured outcome (Figure 5.2).

Thanks to this new ventilation amplitude, we can compute the oxygen flow to the blood at rest and during maximal exercise for a cured outcome, see Figures 5.12 and 5.13.

At rest, on the contrary to the previous section, we observe a lower oxygen flow to the blood when a bronchus is inflamed. Interestingly, a curious phenomenon appears between hour 75 and hour 125 of the infection. Indeed, we observe a change of variation of the oxygen flow during the decrease of the inflammation of the bronchi. This phenomenon can be explained thanks to the oxygen flow in the subtrees of the lung. Actually, we can observe on Figure 5.12 that the flow in the subtrees 1 and 2 do not come back to the healthy situation with the same slope. The oxygen flow in the subtree 2 starts its decrease around hour 75. Since the airflow is more important in the substree 2, it can go deeper into the lung and hence, reach a larger exchange surface. However, once the air flow decreases, it will not go as deep in the lung and hence, the usable exchange surface will be smaller. In the subtree 1 the oxygen flow remains almost constant until hour 100. Indeed, small air flows do not reach the exchange surface. It is due to the localization of the transition between convection and diffusion. In chapter 4, we computed the localization of the transition with the optimal ventilation. This transition happens at the very beginning of the acinus. However, if the amplitude is smaller, the transition between convection and diffusion will occur higher in the generations. Hence, the air flow in subtree 1 has to be sufficiently large to reach the acinus.

During maximal exercise (Figure 5.13), we do not observe the same phenomenon. Actually, during intense exercise the airflow is larger and uses the totality of the exchange surface as predicted by the localization of the transition between convection and diffusion detailed in chapter 4. Hence, in the subtree 1 attached to the inflamed bronchus, the lower airflow can still reach the exchange surface. This explains why the oxygen flows in the subtrees 1 and 2 evolve similarly with time and why we obtain strickly increasing oxygen flows with time when the inflammation of the bronchus decreases.

Notice that the same computations were made for the carbon dioxide flow from the blood. Since the evolutions were very similar to those of oxygen, the results are not shown and allows to focus only on the oxygen flow in all this chapter.

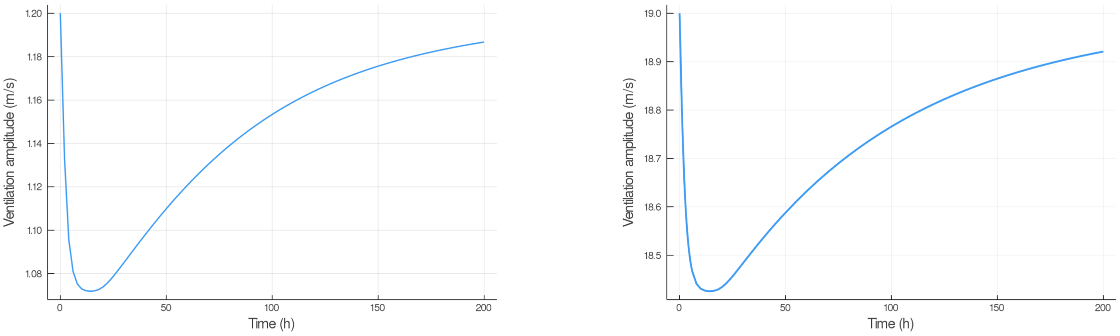

Figure 5.11: Evolution of the ventilation amplitude during an infection of a single bronchus in the third generation at rest (left) and during maximal exercise (right) for a cured outcome.

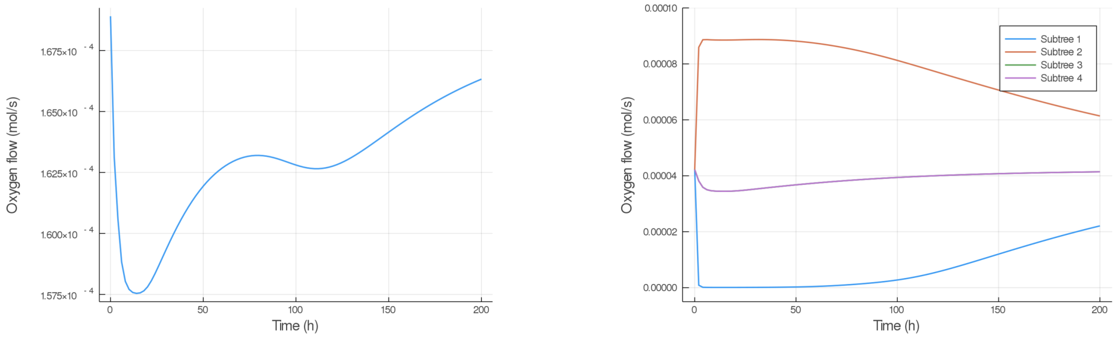

Figure 5.12: Evolution of the oxygen flow to the blood during an infection of a single bronchus in the third generation at rest in the whole lung (left) and in each of the four substrees (right).

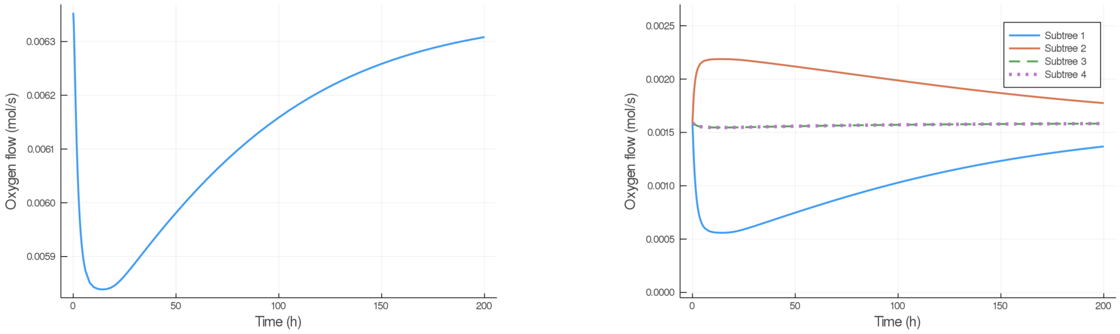

Figure 5.13: Evolution of the oxygen flow to the blood during an infection of a single bronchus in the third generation during maximal exercise in the whole lung (left) and in each of the four substrees (right).

5.3 Proximal infection

Most of the time, the infection does not remain on one bronchus only, it spreads to its neighbors bronchi. In order to be more realistic, it is important to simulate the propagation of an infection throughout the lung. First, we chose to model only a proximal infection, *i.e.* an infection that is limited to the nine first generations of the lung. Indeed, some diseases are localized in certain part of the lung. For example, pneumonia affects mainly the alveoli and bronchitis affects the first generations of the bronchial tree [78]. In our case, the limitation to the nine first generations is because of a technical limitation as explained in appendix A.

Our infection starts from the the third generation of bronchi and we suppose that we have a constant pressure drop between the inlet and the outlet of the tree during the infection, like in the previous section. To model the propagation of the infection, we suppose that we have a probability to spread the infection every 15 minutes. Once a bronchus is infected it can infect its mother bronchus and its two daughters bronchi with a probability that depends on the amount of pathogens present in the brochus. The newly infected bronchi will suffer from an infection with the same properties as the one from where the infection originates.

We assume that the probability function PF for the propagation of the infection in the bronchi has the following form,

$$PF(P, P_{\text{final}}) = \begin{cases} \dfrac{1}{2}\left(\dfrac{2P}{P_{\text{final}}}\right)^2, & \text{for } P < \dfrac{P_{\text{final}}}{2}, \\ 1 - \dfrac{1}{2}\left(\dfrac{2(P_{\text{final}} - P)}{P_{\text{final}}}\right)^2, & \text{for } \dfrac{P_{\text{final}}}{2} \leqslant P < P_{\text{final}}, \\ 1, \quad \text{for } P > P_{\text{final}}. \end{cases} \tag{5.13}$$

P is the number of pathogen present in the bronchus and P_{final} is a parameter that represents the speed of the propagation. Actually, the lower this variable is, the faster the propagation. In our simulations, we use four different P_{final} to model different speeds of infection proliferation, as shown on Figure 5.14.

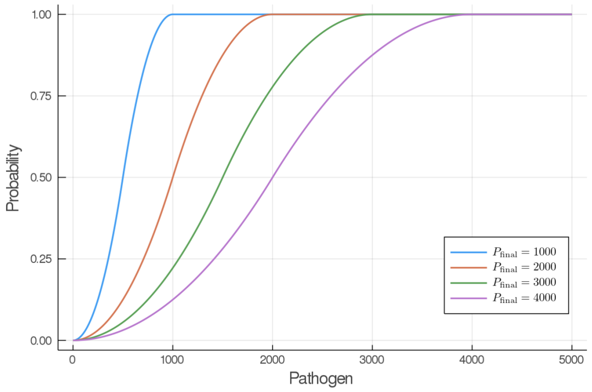

Figure 5.14: Probability functions for the propagation of infections in the lung.

Since our model is stochastic, the simulations do not always lead to the same results. We propose here several computations that are representative of the majority of the responses observed.

5.3.1 Cured outcome

Our first set of simulations reflects a propagation of an infection where each bronchus has a cured outcome (Figure 5.2). First, with the propagation speed parameter P_{final} equal to 4000, the infection tends to remain in the initial bronchus. The results for this case were already detailed in the previous section. Next, by decreasing the propagation speed parameter, the infection spreads to other bronchi but not to the whole lung. Indeed with P_{final} equals to 3000, the infection spreads to its mother bronchus and its two daughters, with a total of 4 infected bronchi. With P_{final} equals to 2000, we obtain 24 infected bronchi. Finally, with P_{final} equals to 1000, the infection propagates to 208 infected bronchi.

In this cured outcome, some interesting phenomenon appears. Indeed, as shown on Figure 5.15, we observe first that when $P_{\text{final}} = 1000$ and when $P_{\text{final}} = 2000$, the ventilation amplitude becomes higher than the healthy ventilation amplitude. This results from the propagation of the infection to the first generation bronchus. Indeed, the expression for the new amplitude writes,

$$A_{\text{inf}} = A_{\text{he}} \frac{R_{\text{he}}}{R_{\text{inf}}} \frac{r_{0,\text{he}}^2}{r_{0,\text{inf}}^2}.$$

The resistance of the inflamed lung is higher than the resistance of the healthy lung since the radius of some bronchi is reduced. Hence, the ventilation amplitude should decrease. However, since the bronchus in the first generation is inflamed the ratio $\frac{r_{0,\text{he}}^2}{r_{0,\text{inf}}^2}$ is bigger than 1, and hence increase the amplitude of the ventilation. The variation of the amplitude of the ventilation is then due to a balance between the inflammation of the tracheal radius and the increase of the hydrodynamic resistance in the lung. Consequently, we can deduce than for $P_{\text{final}} = 1000$ and for $P_{\text{final}} = 2000$, the decrease of the tracheal radius due to the inflammation is dominant over the change in hydrodynamic resistance in the whole lung.

Furthermore, we can also observe that less oxygen is exchanged with the blood in the case with 208 infected bronchi than in the one with 24 infected bronchi. This phenemenon can be explained by the difference in ventilation amplitude as seen on Figure 5.15. Indeed, with an higher amplitude of ventilation, the air flow can go deeper into the lung. Hence, the air flow reaches a larger exchange surface. This difference in amplitude is explained by the fact that the hydrodynamic resistance is higher with a larger number of inflamed bronchi while the tracheal radius is inflamed at the same intensity. Finally, once the infection propagates to the bronchus in the first generation, the oxygen flow exchange with the blood is significantly reduced regardless of the number of infected bronchi.

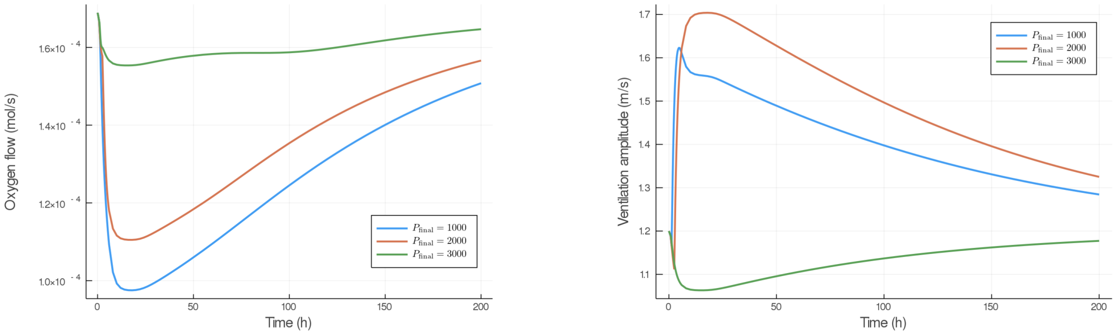

Figure 5.15: Evolution of the oxygen flow to the blood (left) and of the ventilation amplitude (right) during the propagation of an infection starting in a third generation bronchus with an cured outcome.

5.3.2 Aseptic death outcome

Our second set of simulations reflects a propagation of an infection where each bronchus follows an aseptic death outcome (Figure 5.3). The infection spreads to more bronchi than in the cured outcome since more pathogens are present. However, thanks to the elimination of the pathogens by the immune system, it spreads slowly to throughout the lung. We recall that propagation is limited to the nine first generations in the bronchial tree. With $P_{\text{final}} = 4000$, the infection spreads to 108 bronchi. With $P_{\text{final}} = 3000$, it spreads to 226 bronchi. With $P_{\text{final}} = 2000$ or lower, it spreads to the whole proximal lung studied here, *i.e.* to 511 bronchi.

As expected, the oxygen flow decreases as the number of infected bronchi increases, as shown on Figure 5.16. However, an interesting phenomenon appears regarding the ventilation amplitude: we observe two ventilation amplitudes below the healthy ventilation amplitude ($1.2 \text{ m} \cdot \text{s}^{-1}$) and one above. In the case $P_{\text{final}} = 4000$, the amplitude decreases because the first generation bronchus is not infected. In the two other cases, the infection has spread to a big part of the lung, including the first generation bronchus. However, with 226 infected bronchi the ventilation amplitude is above the healthy ventilation amplitude. But, with 511 infected bronchi the ventilation amplitude drops below the healthy ventilation amplitude. It raises the question: at which number of infected bronchi does the ventilation amplitude crashes ? We can observe on Figure 5.17 that the crash of ventilation amplitude occurs at around 300-350 infected bronchi. At this threshold, the increase of the hydrodynamic resistance in the whole lung becomes dominant over the inflammation of the tracheal radius. It confirms that in the case where $P_{\text{final}} = 3000$, the ventilation amplitude stays above the healthy ventilation amplitude. Once the propagation of an infection reaches a certain amount of infected bronchi, the optimal ventilation amplitude to keep a constant pressure drop between the ambient air and the alveoli decreases significantly.

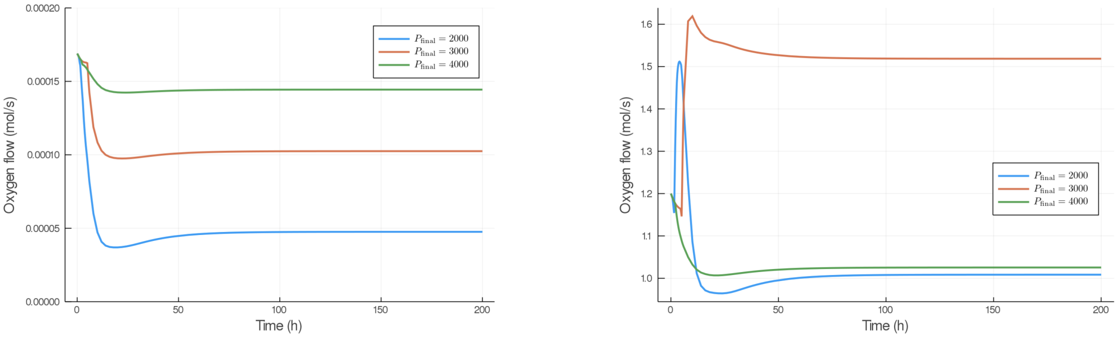

Figure 5.16: Evolution of the oxygen flow to the blood (left) and of the ventilation amplitude (right) during the propagation of an infection starting in a third generation bronchus with an aseptic death outcome.

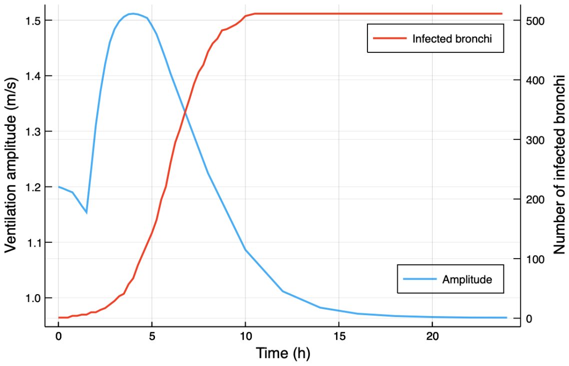

Figure 5.17: Evolution of ventilation amplitude (blue) and number of infected bronchi (red) during the propagation of an infection starting in a third generation bronchus with an aseptic death outcome.

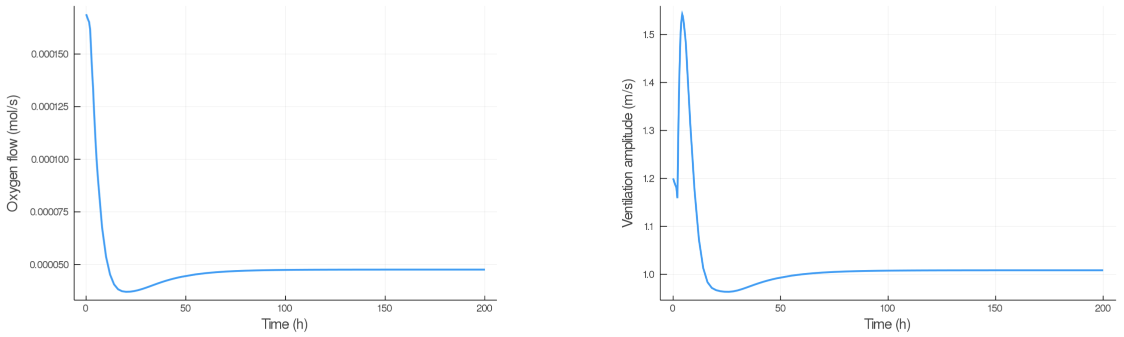

Figure 5.18: Evolution of oxygen flow exchange with the blood (left) and ventilation amplitude (right) during the propagation of an infection starting in a third generation bronchus with a septic death outcome.

5.3.3 Septic death outcome

Our last set of simulations reflects a propagation of an infection where each bronchus has a septic death outcome (Figure 5.4). Since the number of pathogens skyrocket almost to its maximal capacity (20,000), the infection propagates very quickly to the 511 bronchi considered in our simulations, whatever the propagation speed parameter.

In this case, as expected, there is almost no oxygen exchanged with the blood. Indeed, the oxygen flow is reduced by a factor 4, going from 1.7×10^{-4} mol $\cdot$ s^{-1} for the healthy case down to 4×10^{-5} mol $\cdot$ s^{-1}. The new oxygen flow cannot fulfill the body needs in oxygen. The ventilation parameters must be modified in order to hope to fulfill the body needs in oxygen. To confirm this hypothesis, we computed the optimal ventilation that minimizes the energy spent for breathing while fulfilling the oxygen needs in oxygen during maximal inflammation thanks to our model presented in chapter 4. The response predicted is fully compatible with the lung's physiology [78] and brings on the typical strategy of the lung to increase ventilation when gas exchanges are too low. Indeed, the optimal amplitude varies from $1.25\,\mathrm{m} \cdot \mathrm{s}^{-1}$ in the healthy case to $2.36\,\mathrm{m} \cdot \mathrm{s}^{-1}$ during maximal inflammation and the optimal period varies from 4.9 s in the healthy case to 4 s during maximal inflammation.

5.4 Conclusion

We described and studied a model of the propagation of the infection and of the inflammation bronchi per bronchi in the human's lung linked to the gas transport model described in the chapter 4. This last model has been modified in order to take into account the asymmetry of the lung induced by the infection. This first approach gives an insight on the gaseous exchange with the blood during an infection of the lung and also a better understanding of the distribution of the gases along the generations of the lung.

Our first results highlight two main informations. First, with the same ventilation parameters than for a healthy lung, the oxygen flow exchanged with the blood can be increased during an infection, depending on its localization and its expansion. This results from the reserve in exchange surface not used in the healthy case. The second main phenomenon happens when we impose a constant pressure drop between the ambiant air and the alveoli. The oxygen flow exchange with the blood does not always depend on the number of infected bronchi, but more on the localization of the infection.

A lot of work remains to be done concerning this model. It represents a first step towards the understanding of the behaviours of the flows exchange with the blood during an infection. The next logical step would be to minimize the energy spent during the respiration with an inflamed lung and hence, to compute the optimal ventilation for each stage of the inflammation. Furthermore, the model of infection propagation could be improved. Indeed, we assumed that all the infected bronchi follow the same behaviour (cured, aseptic death or septic death). However, we could suppose that the initial number of pathogens in a new infected bronchus is not a constant. For example, it could depend on the amount of inflammation and on the amount of pathogens present in the bronchus from where the infection is coming. The dynamics then become much more complex.

Chapter 6

Deposit of particles for aerosol therapy

Sometimes, the immune system is not efficient enough to fight a pulmonary infection. Many medication aids can be used to help eliminate pathogens. In our case, we will only focus in this chapter on the aerosol therapy, which is commonly used to treat obstructive pulmonary diseases [99]. However, it is extremely difficult to observe in vivo drug deliveries in the human lungs. This is why it appears crucial to model and be able to compute numerically the aerosol flow in the bronchi and especially the deposition fraction which is the fraction of inhaled particles that deposit and their localization with a good enough accuracy.

Aerosol particles have the ability to exchange water with the water saturated air present in the lung. Consequently the size of the aerosol droplets varies along time [66, 64, 65]. Under the assumption that the particles are and stay spherical, we study the influence of the radius growth on deposition (number of deposited particles, characteristic times of propagation/deposition inside a given realistic geometry, deposition areas...).

In the litterature, there exists different types of models that describe the motion of the aerosol particles in the air. First, in the two-phase models [6, 22], the aerosol droplets are considered as a fluid mixed with the ambient air in the lung. Then one focuses on the concentration of the aerosol in the air. However, the drawback of these models is the difficulty to determine the aerosol deposition area. The second type of models [80, 123] is the agent based models, which simulate the behavior of individual particles within an environment. However, the drawback of these models is the difficulty to track the trajectory of numerous particles, in particular when there is a strong coupling between the particles and the air flow. Finally, the kinetic models [7, 40] describe the changes in properties of the system of interest. It is relevant from the modelling point of view since numerous particles are present in the aerosol, but their volume is negligible compared to the airways volume.

This is why we choose to use this last approach. In this work, the aerosol behavior is described through a distribution function that represents the density of the particles and depends on macroscopic variables (time, space, position) as well as microscopic ones (velocity, for instance). This function satifies the Vlasov-type equation and is coupled with the incompressible Navier-Stokes equations that

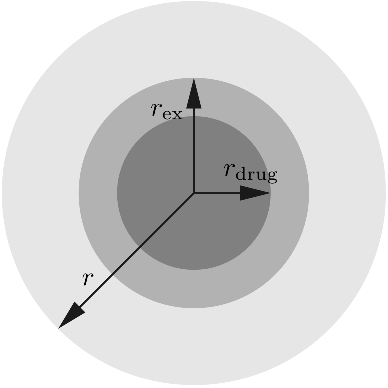

Figure 6.1: Equivalent radii in a droplet

describe the airflow [15]. Our model is an extension of a previous one [76], where the the air temperature, the mass fraction of the water vapor in the air and the dependence of the distribution function on both the size and temperature of the particles are taken into account.

6.1 Model of the deposit of aerosol particles

6.1.1 Particles behavior

An aerosol particle is composed of three different elements: active products (drug), excipient and water. For simplification, our particles are assumed to remain spherical at all times. We can then define the radius r_{drug} of the drug component (see Figure 6.1) such that the value $\frac{4}{3}\pi r_{\mathrm{drug}}^3 \varrho_{\mathrm{drug}}$ is the mass of the active product inside the particle and where ϱ_{drug} is the constant density of the drug. Likewise the radius r_{ex} of the excipient is defined such that the expression $\frac{4}{3}\pi \left(r_{\mathrm{ex}}^3 - r_{\mathrm{drug}}^3\right) \varrho_{\mathrm{ex}}$ is the mass of the excipient component in the droplet wher ϱ_{ex} is the constant density of the excipient. The radius r_{ex} is also considered as the particle dry radius since there is no water in a dry droplet. With these definitions, it is now possible to define the mass and the density of the particle, which both depend on the radius r of the droplet:

$$m(r) = \frac{4}{3}\pi \left[r_{\mathrm{drug}}^3 \varrho_{\mathrm{drug}} + (r_{\mathrm{ex}}^3 - r_{\mathrm{drug}}^3)\varrho_{\mathrm{ex}} + (r^3 - r_{\mathrm{ex}}^3)\varrho_{\mathrm{w}}\right],$$
$$\varrho_{\mathrm{d}}(r) = \frac{1}{r^3} \left[r_{\mathrm{drug}}^3 \varrho_{\mathrm{drug}} + (r_{\mathrm{ex}}^3 - r_{\mathrm{drug}}^3)\varrho_{\mathrm{ex}} + (r^3 - r_{\mathrm{ex}}^3)\varrho_{\mathrm{w}}\right],$$

where ϱ_{w} is the constant density of water.

The radius of the aerosol particles can change over time. Indeed, since the droplets are in an humid environnement (lung) and are composed of water, they can exchange water molecules with the environnement. We can define the function a that represents the evolution of the radius based on [65]. It depends on the radius r of the particle, on the temperature T of the particle and on the water vapor mass fraction in the air $Y_{\mathrm{v,air}}(t,x)$. It writes,

$$a(r,T,Y_{\mathrm{v,air}}(t,x)) = -\frac{N_{\mathrm{d}}(r,T,Y_{\mathrm{v,air}}(t,x))}{\varrho_{\mathrm{w}}}, \tag{6.1}$$

where N_d is the water mass flux at the droplet surface. This function writes [65],

$$N_{\mathrm{d}}(r,T,Y_{\mathrm{v,air}}(t,x)) = \varrho_{\mathrm{air}} \frac{\mathrm{Sh}\, D_{\mathrm{v}}(T_{\mathrm{air}})\, C_m}{2r} \frac{Y_{\mathrm{v,surf}}(r,T) - Y_{\mathrm{v,air}}(t,x)}{1 - Y_{\mathrm{v,surf}}(r,T)}.$$

Let us now define the quantities used in this expression. First we have the air density ϱ_{air}. In our work the air is assumed to be Newtonian and incompressible, hence ϱ_{air} is constant. Notice that the water vapor density in the air can be computed as $\varrho_{\mathrm{air}} Y_{\mathrm{v,air}}$. Sh is the Sherwood number, describing the water transfer between the air and the droplet. C_m is the mass Knudsen number correction [88]. The function D_v is the binary diffusion coefficient of water vapor in the air, it writes [65],

$$D_{\mathrm{v}}(T_{\mathrm{air}}(t,x)) = 0.216 \left(\frac{T_{\mathrm{air}}(t,x)}{273.15}\right)^{1.8}.$$

The temperature of the air T_{air} is expressed in Kelvin in this expression. Finally, $Y_{\mathrm{v,surf}}$ represents the water vapor mass fraction on the droplet surface. It depends on the radius and on the temperature of the particle [65]:

$$Y_{\mathrm{v,surf}}(r,T) = \frac{S(r)K(r,T)P_{\mathrm{v,sat}}(T)}{\varrho_{\mathrm{d}}(r) R_{\mathrm{v}} T}.$$

The constant R_{v} is the gas constant of water vapor. The function $S(r)$ represents the water activity coefficient:

$$S(r) = \frac{\dfrac{\varrho_{\mathrm{w}}(r^3 - r_{\mathrm{ex}}^3)}{M_{\mathrm{w}}}}{\dfrac{\varrho_{\mathrm{w}}(r^3 - r_{\mathrm{ex}}^3)}{M_{\mathrm{w}}} + i_{\mathrm{drug}} \dfrac{\varrho_{\mathrm{drug}} r_{\mathrm{drug}}^3}{M_{\mathrm{drug}}} + i_{\mathrm{ex}} \dfrac{\varrho_{\mathrm{ex}}(r_{\mathrm{ex}}^3 - r_{\mathrm{drug}}^3)}{M_{\mathrm{ex}}}},$$

where M_{w}, M_{drug} and M_{ex} are respectively the molar masses of the water, the drug and the excipient. The constants i_{drug} and i_{ex} denote the van't Hoff factors of the drug and of the excipient. It allows to take into account the molecular dissociation during dissolution. This expression was derived using the expression detailed in [65] and by stating that S must be equal to zero when the particle is dry, in other terms when $r = r_{\mathrm{ex}}$.

The function $K(r,T)$ represents the influence of the Kelvin effect on the droplet surface concentration of water vapor [65]:

$$K(r,T) = \exp\left(\frac{2\sigma}{r \varrho_{\mathrm{d}}(r) R_{\mathrm{v}} T}\right),$$

where σ, the droplet surface tension, is assumed to be constant.

Finally, we have the water vapor saturation pressure $P_{\mathrm{v,sat}}$ that depends on the temperature T of the droplet in Kelvin,

$$P_{\mathrm{v,sat}}(T) = 10 \exp\left(23.196 - \frac{3816.44}{T - 46.13}\right).$$

Let us define a lower bound for the particle's radius. We suppose that, at initial time, all droplets have a radius superior to r_{ex}. In this case, if the radius decreases and reaches the value r_{ex}, we obtain by definition $S(r_{\mathrm{ex}}) = 0$ and consequently $Y_{\mathrm{v,surf}} = 0$. This implies that the function N_{d} is negative and the function a positive. Since the function a governs the time evolution of the particle's radius, the fact that this function is positive once it reaches $r = r_{\mathrm{ex}}$ means that the radius will grow once the particle is dry. That ensures that r cannot go below r_{ex}.

The radius of the particle is not the only physical value that changes over time. The evolution of the temperature can also be taken into account. Indeed, usually the ambient air is colder than the body temperature (37° C). Hence, the inhaled air and, consequently, the particles get warmer once in the respiratory system. Since we want to take into account water vapor condensation on the droplet surface and water vapor evaporation from the droplet surface, we must define the two heat fluxes between the air and the droplet: the convective flux Q_{d} and the evaporative flux $L_v N_{\mathrm{d}}$ where L_v is the latent heat of water vaporisation. The convective flux Q_{d} depends on the radius r, on the temperature T of the droplet and on the temperature of the air T_{air} [65]:

$$Q_{\mathrm{d}}(r, T, T_{\mathrm{air}}(t, x)) = \frac{\mathrm{Nu}\, \kappa_{\mathrm{air}}\, C_T}{2r}(T - T_{\mathrm{air}}(t, x)),$$

where Nu is the droplet Nusselt number corresponding to the ratio of convective to conductive heat transfer between the particle and the air, κ_{air} is the thermal conductivity of the air as a gaseous mixture and C_T is the Knudsen correlation. This last constant is small in our work, it allows us to neglect non-continuum effects of the fluid. We can then define the function b describing the evolution of the temperature of the particles,

$$\begin{aligned} b(r, T, Y_{\mathrm{v,air}}(t, x), T_{\mathrm{air}}(t, x)) = & \frac{3}{\varrho_{\mathrm{d}}(r) c_{P_{\mathrm{d}}} r} \times \\ & (-Q_{\mathrm{d}}(r, T, T_{\mathrm{air}}(t, x)) - L_{\mathrm{v}} N_{\mathrm{d}}(r, T, Y_{\mathrm{v,air}}(t, x))), \end{aligned} \tag{6.2}$$

where $c_{P_{\mathrm{d}}}$ is the constant specific heat of the droplet.

We can define a lower bound for the droplet's temperature. If T somehow come close to 46.13 K (the value in $P_{\mathrm{v,sat}}$) then $Y_{\mathrm{v,surf}}$ tends to zero and N_{d} is negative. Furthermore Q_{d} is also non positive since T_{air} in the lung is around 300 K. The function b that governs the evolution of the temperature of the droplet, is positive when the temperature T reaches 46.13 K. It ensures that T cannot go below 46.13 K in our model. Notice that from the physiological viewpoint, it seems relevant to assume that all the temperatures remain around 300 K and that the water vapor mass fraction $Y_{\mathrm{v,air}}$ stays positive.

6.1.2 Equations of the model

Domain

First let us define our space domain Ω. It is assumed not to depend on time. Its boundary $\Gamma = \partial\Omega$ is divided into three subsets, the wall Γ^{wall}, the inlet Γ^{in} and the outlet Γ^{out}. In our case, since we want to observe the behavior of the aerosol particles in the lung, the domain represents a bronchus and its bifurcation into two smaller branches (see Figure 6.2).

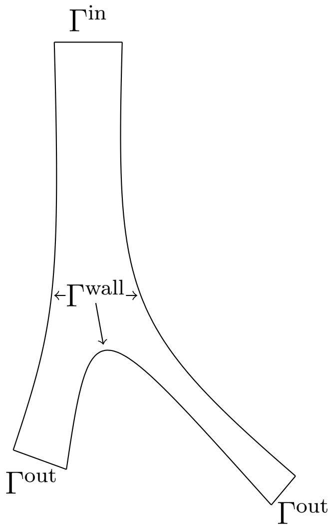

Figure 6.2: Domain Ω

Distribution function

We consider now a distribution function f representing the density of particles per unit volume. This function depends on the time $t \geqslant 0$, on the position x of the particles in the domain Ω, on the velocity $v \in \mathbb{R}^3$, on the radius of the particles $r > 0$ and on the temperature $T > 0$. We assume that the particles remain spherical and do not interact with each other since their number is not significant enough to take into account their collisions. The density function f satisfies a Vlasov-type equation [15]:

$$\partial_t f + v \cdot \nabla_x f + \operatorname{div}_v[(\alpha(u - v) + g)f] + \partial_r(af) + \partial_T(bf) = 0, \tag{6.3}$$

where g is the gravitational field and $\alpha(u - v)$ is the drag acceleration undergone by the aerosol from the air. u is the velocity of the airflow and the α function writes [15],

$$\alpha(r) = \frac{6\pi\eta r}{m(r)},$$

with η the constant air dynamic viscosity.

We can complete the equation (6.3) with the following boundary and initial conditions,

$$\begin{cases} f = f^{\text{in}} & \text{on } \mathbb{R}_+ \times \Gamma^{\text{in}} \times \mathbb{R}^3 \times \mathbb{R}_+^* \times \mathbb{R}_+^*, \\ f(t,\cdot) = 0 & \text{on } \Gamma^{\text{wall}} \times \mathbb{R}^3 \times \mathbb{R}_+^* \times \mathbb{R}_+^*, \quad \text{if } v \cdot n \leq 0, \quad \text{a.e. } t, \\ f(0,\cdot) = f_{\text{init}} & \text{on } \Omega \times \mathbb{R}^3 \times \mathbb{R}_+^* \times \mathbb{R}_+^*, \end{cases}$$

where $f^{\text{in}} : \mathbb{R}_+ \times \Gamma^{\text{in}} \times \mathbb{R}^3 \times \mathbb{R}_+^* \times \mathbb{R}_+^* \to \mathbb{R}$ and $f_{\text{init}} : \Omega \times \mathbb{R}^3 \times \mathbb{R}_+^* \times \mathbb{R}_+^* \to \mathbb{R}$ are given. The boundary condition on Γ^{wall} ensures that any droplet landing on the wall remains deposited afterwards.

Fluid dynamics of the air

Now let us express the equations of the fluid dynamics of the air. First, we want to determine the fluid velocity $u(t,x) \in \mathbb{R}^3$ and its pressure $p(t,x) \in \mathbb{R}^3$ [15]. They satisfy the incompressible Navier-Stokes equations on $\mathbb{R}_+$,

$$\varrho_{\text{air}}[\partial_t u + (u \cdot \nabla_x u)] - \eta \Delta_x u + \nabla_x p = F, \tag{6.4}$$

$$\operatorname{div}_x u = 0. \tag{6.5}$$

The function F is called the aerosol retroaction on the air:

$$F(t,x) = -\iiint_{\mathbb{R}^3 \times \mathbb{R}_+ \times \mathbb{R}} m(r)\alpha(r)(u(t,x) - v) f(t,x,v,r,T)\, \mathrm{d}v\, \mathrm{d}r\, \mathrm{d}T$$
$$= -\iiint_{\mathbb{R}^3 \times \mathbb{R}_+^* \times \mathbb{R}_+^*} 6\pi\eta r(u(t,x) - v) f(t,x,v,r,T)\, \mathrm{d}v\, \mathrm{d}r\, \mathrm{d}T.$$

We can complete this equation with the following boundary and initial conditions,

$$\begin{cases} u = u^{\text{in}} & \text{on } \mathbb{R}_+ \times \Gamma^{\text{in}}, \\ u = 0 & \text{on } \mathbb{R}_+ \times \Gamma^{\text{wall}}, \\ \sigma(u,p) \cdot n = 0 & \text{on } \mathbb{R}_+ \times \Gamma^{\text{out}}, \\ u(0,\cdot) = u_{\text{init}} & \text{on } \Omega, \end{cases}$$

with $\sigma(u,p) = \nabla_x u + (\nabla_x u)^\intercal - p\,\mathrm{Id}$, the stress tensor, n the outgoing normal vector from Γ. The function $u^{\text{in}} : \mathbb{R}_+ \times \Gamma^{\text{in}} \to \mathbb{R}^3$ is the airflow velocity at the entrance of the bronchus, it is assumed to be a Poiseuille flow in our case. The function $u_{\text{init}} : \Omega \to \mathbb{R}^3$ is the initial datum.

Second, we have to describe the evolution of the water vapor mass fraction $Y_{\text{v,air}}$ in the air. It satisfies an advection-diffusion equation on $\mathbb{R}_+ \times \Omega$, it writes,

$$\varrho_{\text{air}}[\partial_t Y_{\text{v,air}} + (u \cdot \nabla_x) Y_{\text{v,air}}] - \operatorname{div}_x(D_{\text{v}}(T_{\text{air}}) \nabla_x Y_{\text{v,air}}) = S_Y, \tag{6.6}$$

where S_Y is a source term that accounts for the water mass exchanges between the air and the aerosol. However, other effects could be taken into account in this expression such as turbulence [64, 66]. The source term S_Y is defined very similarly as in [65] by,

$$S_Y(t,x) = \varrho_{\text{w}} \iiint_{\mathbb{R}^3 \times \mathbb{R}_+^* \times \mathbb{R}_+^*} 4\pi r^2 N_{\text{d}}(r,T,Y_{\text{v,air}}(t,x))\, f(t,x,v,r,T)\, \mathrm{d}v\, \mathrm{d}r\, \mathrm{d}T.$$

We complete our equation with the following boundary and initial conditions,

$$\begin{cases} Y_{\mathrm{v,air}} = Y^{\mathrm{in}}_{\mathrm{v,air}} & \text{on } \mathbb{R}_+ \times \Gamma^{\mathrm{in}}, \\ Y_{\mathrm{v,air}} = Y_{\mathrm{v,wall}} & \text{on } \mathbb{R}_+ \times \Gamma^{\mathrm{wall}}, \\ \nabla_x Y_{\mathrm{v,air}} \cdot n = 0 & \text{on } \mathbb{R}_+ \times \Gamma^{\mathrm{out}}, \\ Y_{\mathrm{v,air}}(0,\cdot) = Y_{\mathrm{v,air,init}} & \text{on } \Omega, \end{cases}$$

where the functions $Y^{\mathrm{in}}_{\mathrm{v,air}}$, $Y_{\mathrm{v,wall}}$ and $Y_{\mathrm{v,air,init}} > 0$ are given. The boundary condition on Γ^{wall} ensures us that the wall continuously provides water vapor to the air.

Finally, let us describe the evolution of the temperature T_{air} of the air. It also satisfies an advection-diffussion equation on $\mathbb{R}_+ \times \Omega$:

$$\varrho_{\mathrm{air}} c_{P_{\mathrm{air}}} [\partial_t T_{\mathrm{air}} + (u \cdot \nabla_x) T_{\mathrm{air}}] - \kappa_{\mathrm{air}} \Delta_x T_{\mathrm{air}} = S_T, \tag{6.7}$$

with S_T a source term that represents the heat transfer between the air and the particles through the water vapor. It is also defined as in [65] by,

$$S_T(t,x) = \iiint_{\mathbb{R}^3 \times \mathbb{R}^*_+ \times \mathbb{R}^*_+} 4\pi r^2\, Q_{\mathrm{d}}(r, T, T_{\mathrm{air}}(t,x))\, f(t,x,v,r,T)\, \mathrm{d}v\, \mathrm{d}r\, \mathrm{d}T.$$

We complete this equation with the following boundary and initial conditions,

$$\begin{cases} T_{\mathrm{air}} = T^{\mathrm{in}}_{\mathrm{air}} & \text{on } \mathbb{R}_+ \times \Gamma^{\mathrm{in}}, \\ T_{\mathrm{air}} = T_{\mathrm{wall}} & \text{on } \mathbb{R}_+ \times \Gamma^{\mathrm{wall}}, \\ \nabla_x T_{\mathrm{air}} \cdot n = 0 & \text{on } \mathbb{R}_+ \times \Gamma^{\mathrm{out}}, \\ T_{\mathrm{air}}(0,\cdot) = T_{\mathrm{air,init}} & \text{on } \Omega. \end{cases}$$

To summarize let us rewrite all our equations without the boundary and initial conditions to form our complete model,

$$\begin{cases} \partial_t f + v \cdot \nabla_x f + \mathrm{div}_v[(\alpha(u-v)+g)f] + \partial_r(af) + \partial_T(bf) = F, \\ \varrho_{\mathrm{air}}[\partial_t u + (u \cdot \nabla_x u)] - \eta \Delta_x u + \nabla_x p = 0, \quad \mathrm{div}_x\, u = 0, \\ \varrho_{\mathrm{air}}[\partial_t Y_{\mathrm{v,air}} + (u \cdot \nabla_x) Y_{\mathrm{v,air}}] - \mathrm{div}_x(D_{\mathrm{v}}(T_{\mathrm{air}}) \nabla_x Y_{\mathrm{v,air}}) = S_Y, \\ \varrho_{\mathrm{air}} c_{P_{\mathrm{air}}}[\partial_t T_{\mathrm{air}} + (u \cdot \nabla_x) T_{\mathrm{air}}] - \kappa_{\mathrm{air}} \Delta_x T_{\mathrm{air}} = S_T, \end{cases} \tag{6.8}$$

6.1.3 Physical conservations

Let us check some physical conservations of the two quantities that involve water vapor. First, let us observe the water vapor mass exchange. Indeed the water vapor coming from the air is supposed to lead to a radius variation of the aerosol droplets.

Proposition 6.1.1. *Assume that* $u = 0$ *and* $\nabla_x Y_{\mathrm{v,air}} \cdot n = 0$ *on* $\partial\Omega$, *and that* $f = 0$ *on* $\partial\Omega \times \mathbb{R}^3 \times \mathbb{R}^*_+ \times \mathbb{R}^*_+$. *Then we have*

$$\frac{\mathrm{d}}{\mathrm{d}t}\left[\int_\Omega \left(\varrho_{\mathrm{air}} Y_{\mathrm{v,air}}(t,x) + \iiint_{\mathbb{R}^3 \times \mathbb{R}^*_+ \times \mathbb{R}^*_+} m(r) f(t,x,v,r,T)\, \mathrm{d}v\, \mathrm{d}r\, \mathrm{d}T\right) \mathrm{d}x\right] = 0.$$

Proof. On the one hand, multiplying equation (6.3) by $m(r)$, integrating it with respect to all the variables except t, and eliminating the conservative terms through integrations by parts, we obtain

$$\frac{\mathrm{d}}{\mathrm{d}t}\left[\int_\Omega \iiint_{\mathbb{R}^3\times\mathbb{R}_+^*\times\mathbb{R}_+^*} m(r) f(t,x,v,r,T)\,\mathrm{d}v\,\mathrm{d}r\,\mathrm{d}T\,\mathrm{d}x\right]$$
$$= \int_\Omega \iiint_{\mathbb{R}^3\times\mathbb{R}_+^*\times\mathbb{R}_+^*} m'(r)\, a(r,T,Y_{\mathrm{v,air}}(t,x))\, f(t,x,v,r,T)\,\mathrm{d}v\,\mathrm{d}r\,\mathrm{d}T\,\mathrm{d}x.$$

On the other hand, integrating equation (6.6) on Ω, we get,

$$\frac{\mathrm{d}}{\mathrm{d}t}\left[\int_\Omega \varrho_{\mathrm{air}} Y_{\mathrm{v,air}}(t,x)\,\mathrm{d}x\right] = \int_\Omega S_Y(t,x)\,\mathrm{d}x$$
$$= \int_\Omega \iiint_{\mathbb{R}^3\times\mathbb{R}_+^*\times\mathbb{R}_+^*} 4\pi r^2 \varrho_{\mathrm{w}} N_{\mathrm{d}}(r,T,Y_{\mathrm{v,air}}(t,x))\, f(t,x,v,r,T)\,\mathrm{d}v\,\mathrm{d}r\,\mathrm{d}T\,\mathrm{d}x$$
$$= -\int_\Omega \iiint_{\mathbb{R}^3\times\mathbb{R}_+^*\times\mathbb{R}_+^*} m'(r)\, a(r,T,Y_{\mathrm{v,air}}(t,x))\, f(t,x,v,r,T)\,\mathrm{d}v\,\mathrm{d}r\,\mathrm{d}T\,\mathrm{d}x.$$

That clearly concludes the formal proof. □

Second let us observe the exchange of the thermal energy associated to water transfers between the air and the aerosol droplets.

Proposition 6.1.2. *Assume that* $u = 0$ *and* $\nabla_x T_{\mathrm{air}} \cdot n = 0$ *on* $\partial\Omega$*, and that* $f = 0$ *on* $\partial\Omega \times \mathbb{R}^3 \times \mathbb{R}_+^* \times \mathbb{R}_+^*$*. Then we have*

$$\frac{\mathrm{d}}{\mathrm{d}t}\left[\int_\Omega \left(\varrho_{\mathrm{air}} c_{P_{\mathrm{air}}} T_{\mathrm{air}}(t,x) + \iiint_{\mathbb{R}^3\times\mathbb{R}_+^*\times\mathbb{R}_+^*} m(r) c_{P_{\mathrm{d}}} T f(t,x,v,r,T)\,\mathrm{d}v\,\mathrm{d}r\,\mathrm{d}T\right)\mathrm{d}x\right]$$
$$= -\int_\Omega \iiint_{\mathbb{R}^3\times\mathbb{R}_+^*\times\mathbb{R}_+^*} 4\pi r^2 (L_{\mathrm{v}} + c_{P_{\mathrm{d}}} T) N_{\mathrm{d}}(r,T,Y_{\mathrm{v,air}}(t,x))\, f(t,x,v,r,T)\,\mathrm{d}v\,\mathrm{d}r\,\mathrm{d}T\,\mathrm{d}x. \tag{6.9}$$

Proof. On the one hand, we integrate (6.7) over Ω to obtain

$$\frac{\mathrm{d}}{\mathrm{d}t}\left[\int_\Omega \varrho_{\mathrm{air}} c_{P_{\mathrm{air}}} T_{\mathrm{air}}(t,x)\,\mathrm{d}x\right] = \int_\Omega S_T(t,x)\,\mathrm{d}x.$$

Then we multiply (6.3) by $m(r) c_{P_{\mathrm{d}}} T$ and integrate it with respect to all the variables except t to get

$$\frac{\mathrm{d}}{\mathrm{d}t}\left[\int_\Omega \iiint_{\mathbb{R}^3\times\mathbb{R}_+^*\times\mathbb{R}_+^*} m(r) c_{P_{\mathrm{d}}}\, T\, f(t,x,v,r,T)\,\mathrm{d}v\,\mathrm{d}r\,\mathrm{d}T\,\mathrm{d}x\right]$$
$$= \int_\Omega \iiint_{\mathbb{R}^3\times\mathbb{R}_+^*\times\mathbb{R}_+^*} [m'(r) c_{P_{\mathrm{d}}}\, T\, a(r,T,Y_{\mathrm{v,air}}(t,x))\, f(t,x,v,r,T)$$
$$+ m(r)\, b(r,T,Y_{\mathrm{v,air}}(t,x),T_{\mathrm{air}}(t,x))\, f(t,x,v,r,T)]\,\mathrm{d}v\,\mathrm{d}r\,\mathrm{d}T\,\mathrm{d}x.$$

Then we sum both previous equalities to recover equation (6.9), noticing that the term involving Q_{d} vanishes, keeping two terms involving N_{d}: one with L_{v} to take the change of physical state into account and one with the added thermal energy in the aerosol due to the mass exchange. □

6.2 Numerical method

Now, let us perform some numerical tests in order to observe the deposit of the aerosol droplets in a model of a lung's bifurcation. First, for simplification, we suppose that the aerosol retroaction F in equation (6.4) can be neglected ($F = 0$) because it is negligible regarding the particle size range chosen in our model [15].

Now, let us explain the numerical scheme used for our system (6.8). We proceed as in [15] by using a time marching scheme and uncoupling the fluid and the particles equations. All our computations are performed in a two dimensional frame using FreeFem++ [48]. We run our model on a time interval $[0, \tau]$, where $\tau > 0$ is given. The time step is defined as $\Delta t = \tau/N > 0$, such that $N \in \mathbb{N}^*$. We can then denote $t^n = n\Delta t$ for any n in $[\![0, N]\!]$. Regarding the space, the domain Ω is discretized as a triangular mesh Ω_h.

6.2.1 Solving the air equations

We start by solving the three air equations (6.4)-(6.5), (6.6) and (6.7) using a finite element method. The first step in the finite element method is computing the weak formulation of the equations. Hence, we have to introduce the following test functions: $\chi \in L^2(\Omega)$ for the equation (6.5), and ν, ψ, $\phi \in H^1(\Omega)$, vanishing on Γ^{in} and Γ^{wall}, respectively for the equations (6.4), (6.6) and (6.7). The second step of the method is the discretization of the functions. We use $\mathbb{P}_2$ functions for the velocities u and ν and $\mathbb{P}_1$ functions for p, $Y_{\text{v,air}}$, T_{air}, χ, ψ and ϕ. To increment from time t^n to time t^{n+1}, we assume that all our functions are known at time t^n. To handle the convective terme in equation (6.4), we introduce the approximated characteristic flow X^n, which approximates the solution X of the following Cauchy problem on $[t^n, t^{n+1}]$ for any $x \in \Omega_h$,

$$\dot{X}(s) = u^n(s, X(s)), \qquad X(t^{n+1}) = x.$$

This approximated X^n is computed using the FreeFem++ command convect. It is now possible to define u^{n+1} the solution of the discrete weak formulation for the Navier Stokes equations (6.4)-(6.5):

$$\begin{aligned}\varrho_{\text{air}} \int_\Omega \frac{u^{n+1} - u^n \circ X^n}{\Delta t} \cdot \nu \, \mathrm{d}x + \eta \int_\Omega \nabla_x u^{n+1} : \nabla_x \nu \, \mathrm{d}x \\ - \int_\Omega p^{n+1} \operatorname{div}_x \nu \, \mathrm{d}x + \int_\Omega \operatorname{div}_x u^{n+1} \chi \, \mathrm{d}x = 0.\end{aligned}$$

Likewise, $Y_{\text{v,air}}^{n+1}$ and T_{air}^{n+1} are defined as the solutions of the following discrete weak formulations,

$$\begin{aligned}\varrho_{\text{air}} \int_\Omega \frac{Y_{\text{v,air}}^{n+1} - Y_{\text{v,air}}^{n} \circ X^n}{\Delta t} \phi \, \mathrm{d}x + D_{\text{v}} \int_\Omega \nabla_x Y_{\text{v,air}}^{n+1} \cdot \nabla_x \phi \, \mathrm{d}x &= \int_\Omega S_Y^n \phi \, \mathrm{d}x, \\ \varrho_{\text{air}} c_{P_{\text{air}}} \int_\Omega \frac{T_{\text{air}}^{n+1} - T_{\text{air}}^{n} \circ X^n}{\Delta t} \psi \, \mathrm{d}x + \kappa_{\text{air}} \int_\Omega \nabla_x T_{\text{air}}^{n+1} \cdot \nabla_x \psi \, \mathrm{d}x &= \int_\Omega S_T^n \psi \, \mathrm{d}x.\end{aligned}$$

As previously explained, the function D_v is assumed to be constant and not dependent on T_{air} since its value only has a 2% variation in the considered air temperature range.

6.2.2 Solving the Vlasov equation

With the fluid equations resolved at time t^{n+1}, we can now solve the aerosol equations (6.3). We discretize the distribution function f as a weighted sum of Dirac masses in the position, the velocity, the radius and the temperature [35]. Since the total number of physical aerosol particles $N_{\text{aero}} \in \mathbb{N}^*$ is high for our computations, we suppose that we have $N_{\text{num}} \in \mathbb{N}^*$ numerical particles, each of them having the representativity $\omega \in \mathbb{N}^*$, so that we have $N_{\text{aero}} = \omega N_{\text{num}}$. N_{num} must be chosen small enough with respect to N_{aero} to limit the cost of our computations, but large enough to faithfully represent the distribution of the aerosol particles. The distribution function is then discretized as follow,

$$f(t,x,v,r,T) \simeq \omega \sum_{p=1}^{N_{\text{num}}} \delta_{x_p(t)} \otimes \delta_{v_p(t)} \otimes \delta_{r_p(t)} \otimes \delta_{T_p(t)}(x,v,r,T),$$

where $x_p(t)$, $v_p(t)$, $r_p(t)$, $T_p(t)$ are the coordinates of the numerical particle $p \in \{1,\dots,N_{\text{num}}\}$ at time t, expressed in the phase space of f.

The particles coordinates are modified at each time step. They follow the following differential system,

$$\left\{\begin{array}{rcl} \dot{x}_p(t) &=& v_p(t), \\ \dot{v}_p(t) &=& \alpha(r_p(t))(u(t,x_p(t)) - v_p(t)) + (1 - \frac{\varrho_{\text{air}}}{\varrho_{\text{d}}})g, \\ \dot{r}_p(t) &=& a(r_p(t), T_p(t), Y_{\text{v,air}}(t,x_p(t))), \\ \dot{T}_p(t) &=& b(r_p(t), T_p(t), Y_{\text{v,air}}(t,x_p(t)), T_{\text{air}}(t,x_p(t))). \end{array}\right. \tag{6.10}$$

To complete this system we add initial data that fit the initial distribution of the droplets f_{init}. To solve this system at time t^{n+1}, we resolve first the radius equation using an accurate Runge Kutta 4 scheme. It involves the newly computed value $Y_{\text{v,air}}^{n+1}$ and the current position x_p^n. Then, the velocity and the temperature equations are solved with a semi-implicit Euler scheme involving the newly computed data u^{n+1}, $Y_{\text{v,air}}^{n+1}$ and T_{air}^{n+1} at the current position of the particle x_p^n. Finally, we update the position x_p^{n+1} using the newly computed velocity v_p^{n+1}. If the position of the particle x_p^{n+1} is outside the domain Ω_h or if the distance between the boundary and the position is smaller that the radius of the particle r_p^{n+1}, then our droplet is considered deposited or outside our domain, *i.e.* in the next bronchus. Once the particle is deposited or out of the domain, it is no longer treated numerically.

Since all our particles coordinates are updated, we can now define the the source terms in equations (6.6) and (6.7) for the time t^{n+1}. We obtain,

$$\begin{array}{rcl} S_Y^{n+1} &=& \omega \varrho_{\text{w}} \displaystyle\sum_{p=1}^{N_{\text{num}}} 4\pi \left(r_p^{n+1}\right)^2 N_{\text{d}}(r_p^{n+1}, T_{\text{air}}^{n+1}(x_p^{n+1}), Y_{\text{v,air}}^{n+1}(x_p^{n+1}))\delta_{x_p^{n+1}}, \\ S_T^{n+1} &=& \omega \displaystyle\sum_{p=1}^{N_{\text{num}}} 4\pi \left(r_p^{n+1}\right)^2 Q_{\text{d}}(r_p^{n+1}, T_p^{n+1}, T_{\text{air}}^{n+1}(x_p^{n+1}))\delta_{x_p^{n+1}}. \end{array}$$

We observed that a time-subcycling was necessary for our aerosol computations. Indeed, without this subcycling, the particle would be able to go accross multiple cells of the mesh during a single fluid time step. Furthermore, it allows to better deal with the very stiff temperature ODE.

6.3 Numerical simulations

6.3.1 Initial situation

Our domain (see Figure 6.2) represents the trachea and the first bifurcation of the human's lung. Our choice in sizes and shapes of this domain are the ones described in [100, 112], taking into account a 3D-2D correction coefficient for each branch length. The diameter of the trachea is set to $D_0 = 1.80$ cm and its length to $l_0 = 7.52$ cm. The right-hand bronchus has an angle of 25° with the tracheal axis, it is quite short ($l_{10} = 3.75$ cm), but its diameter quite large, $D_{10} = 1.50$ cm. The left-hand bronchus has an angle of 45° with the tracheal axis, it is longer than the first one ($l_{01} = 6.75$ cm), but its diameter is smaller, with $D_{01} = 1.00$ cm. The right-hand bronchus is the left branch on Figure 6.2, and conversely: we have the outsider's view, not the patient's. The origin of our domain is set to the middle of the boundary inlet Γ^{in}. Our simulations are run during $\tau = 1$ s.

Let us now provide all our boundary and initial conditions. First, for the fluid equations, the fluid velocity is initialized at $u_{\text{init}} = 0$, and, at the inlet, u^{in} follows a Poiseuille law, *i.e.* it is vertically oriented from up to bottom and its amplitude is given, for any $x \in \Gamma^{\text{in}}$, by

$$|u^{\text{in}}(x)| = \frac{4u_0}{{D_0}^2}\left(\frac{{D_0}^2}{4} - {x_1}^2\right),$$

where $u_0 = 50.0 \text{ cm} \cdot \text{s}^{-1}$ and x_1 the abscissa coordinates of the position x. The initial and boundary values of $Y_{\text{v,air}}$ uses the relative humidities in the airways,

$$Y_{\text{v,air,init}} = \frac{\text{RH}_{\text{lung}} P_{\text{v,sat}}(T_{\text{air,init}})}{\varrho_{\text{air}} R_{\text{v}} T_{\text{air,init}}}, \quad Y^{\text{in}}_{\text{v,air}} = \frac{\text{RH}_{\text{lung}} P_{\text{v,sat}}(T^{\text{in}}_{\text{air}})}{\varrho_{\text{air}} R_{\text{v}} T^{\text{in}}_{\text{air}}},$$
$$Y_{\text{v,wall}} = \frac{\text{RH}_{\text{wall}} P_{\text{v,sat}}(T_{\text{wall}})}{\varrho_{\text{air}} R_{\text{v}} T_{\text{wall}}}.$$

Here we suppose for homogeneity that the relative humidities in our first bifurcation are $\text{RH}_{\text{lung}} = 0.99$ and $\text{RH}_{\text{wall}} = 1.00$. However, we know that the relative humidity at the entrance of the trachea at inspiration is between 0.8 and 0.95 [56].

Likewise the air temperatures are chosen as follow,

$$T_{\text{air,init}} = 37°\text{C} = 310 \text{ K}, \quad T^{\text{in}}_{\text{air}} = 24°\text{C} = 297 \text{ K}, \quad T_{\text{wall}} = 37°\text{C} = 310 \text{ K}.$$

However, as for the relative humidity, the air temperature at the entrance of the trachea at inspiration is around $30 - 34$°C [56].

Let us now focus on the parameters for the aerosol particles. We consider 5 injections of 100 numerical particles each with a representativity $\omega = 10^4$. These injections are periodically released between the initial time and $t = 0.25$ s. Hence, we deal with $N_{\text{num}} = 500$ numerical particles and $N_{\text{aero}} = 5 \times 10^6$ physical particles. We suppose that, at the initial time, the particles do not contain excipient nor water, *i.e* $r = r_{\text{drug}} = r_{\text{ex}}$. All the numerical particles initially have the same vertical velocity $v_{p,2}(0) = -100 \text{ cm} \cdot \text{s}^{-1}$, the same radius $r_p(0) = 2.25 \times 10^{-5}$ cm, and the same temperature $T_p(0)$, equals to the air temperature $T_{\text{air}}^{\text{in}}$ at the inlet. They are released from random positions $x_p(0) \in \Gamma^{\text{in}}$ with its first coordinate in $[-D_0/4, D_0/4]$ following a uniform law. We choose this latter interval instead of $[-D_0/2, D_0/2]$ so that it allows a larger deposition phenomenon. Since we use a particle method, it is mandatory, in order to obtain meaningful results, to perform averaging computations over several initial randomly chosen distributions of droplets. In our case, we worked with 10 different distributions. We validated our code by checking the computional mass conservation of water vapor and the thermal energy balance implied by the thermodynamic state change of water vapor.

Finally, Table 6.1 summarizes all the constants used in our model.

QUANTITY	VALUE
$\lvert g\rvert$: Gravitation	980 cm $\cdot$ s^{-2}
ϱ_{air}: Air mass density	$1.18\ 10^{-3}$ g$\cdot$cm^{-3}
$c_{P_{\text{air}}}$: Air specific heat	$1.01\ 10^{7}$ cm$^2 \cdot$ s$^{-2} \cdot$ K^{-1}
κ_{air}: Air thermal conductivity	$2.60\ 10^{3}$ g$\cdot$cm$\cdot$s$^{-3} \cdot$ K^{-1}
η: Air dynamic viscosity	$1.18\ 10^{-4}$ g$\cdot$cm$^{-1} \cdot$ s^{-1}
ϱ_{w}: Water mass density	0.997 g$\cdot$cm^{-3}
ϱ_{drug}: Drug mass density	1.34 g$\cdot$cm^{-3}
ϱ_{ex}: Excipient mass density	2.17 g$\cdot$cm^{-3}
M_{w}: Water molar mass	18.0 g$\cdot$mol^{-1}
M_{drug}: Drug molar mass	577 g$\cdot$mol^{-1}
M_{ex}: Excipient molar mass	58.4 g$\cdot$mol^{-1}
i_{drug}: Drug van't Hoff coefficient	2.10
i_{ex}: Excipient van't Hoff coefficient	2.10
$c_{P_{\text{d}}}$: Droplet specific heat	$4.18\ 10^{7}$ cm$^2 \cdot$ s$^{-2} \cdot$ K^{-1}
C_m: Droplet mass Knudsen number correction	1.00
C_T : Droplet temperature Knudsen correlation	1.00
Nu: Droplet Nusselt number	2.00
Sh: Droplet Sherwood number	2.00
L_{v}: Water vaporization latent heat	$2.26\ 10^{10}$ cm$^2 \cdot$ s^{-2}
σ: Droplet surface tension	72.0 dyn$\cdot$cm^{-1}
R_{v}: Water vapor specific gas constant	$4.61\ 10^{6}$ cm$^2 \cdot$ s$^{-2} \cdot$ K^{-1}

Table 6.1: Value of the physical constants.

6.3.2 Exploration of the model

First, we observe the results obtained without aerosol particles in the domain. Figure 6.3 shows the values of the velocity u, the water vapor mass fraction in the air $Y_{\text{v,air}}$ and the temperature of the air T_{air} at the final time $\tau = 1$ s where a stationary state is reached for the fluid.

Let us now inject the aerosol particles in the domain. On Figure 6.4, we can observe the movement of the various aerosol releases and the behavior of the air velocity u. On Figure 6.5 we can observe the behavior of the air temperature T_{air} at different times. The water vapor mass fraction $Y_{\text{v,air}}$ reaches a stationnary state

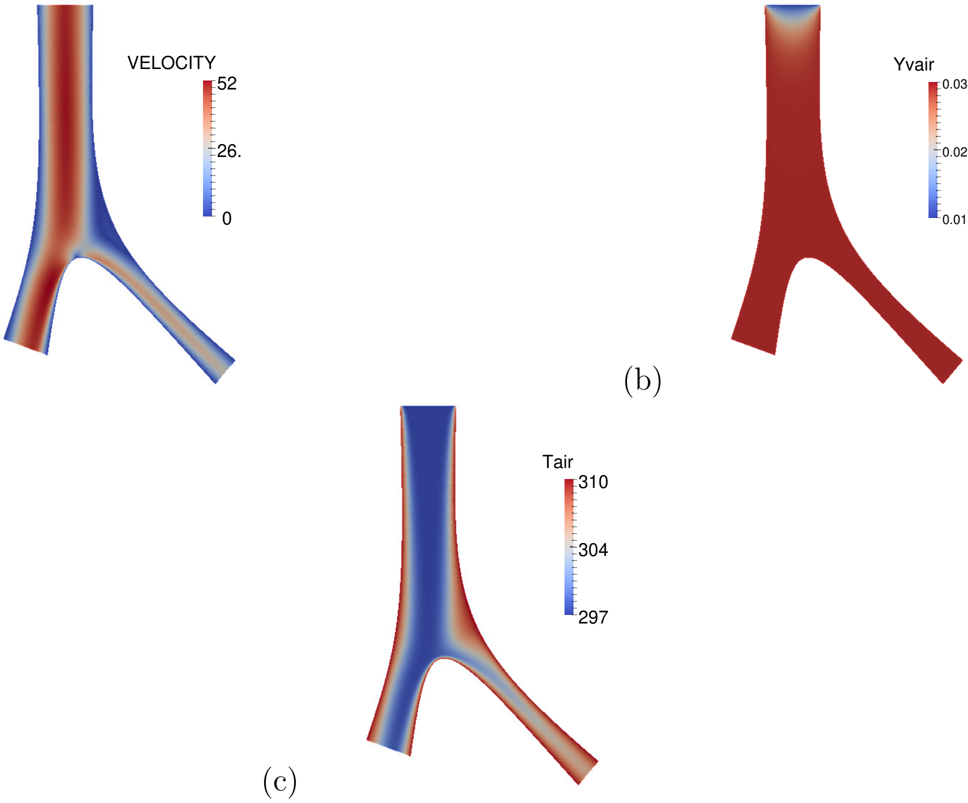

(a) (b) (c)

Figure 6.3: Distribution of (a) the velocity $|u|$, (b) the water vapor mass fraction in the air $Y_{\mathrm{v,air}}$ and (c) the temperature T_{air} at the final time $\tau = 1$ s.

very fast, whereas u and T_{air} only do so near 0.48 s. The distribution of $Y_{\mathrm{v,air}}$ in the domain is the same as on Figure 6.3.

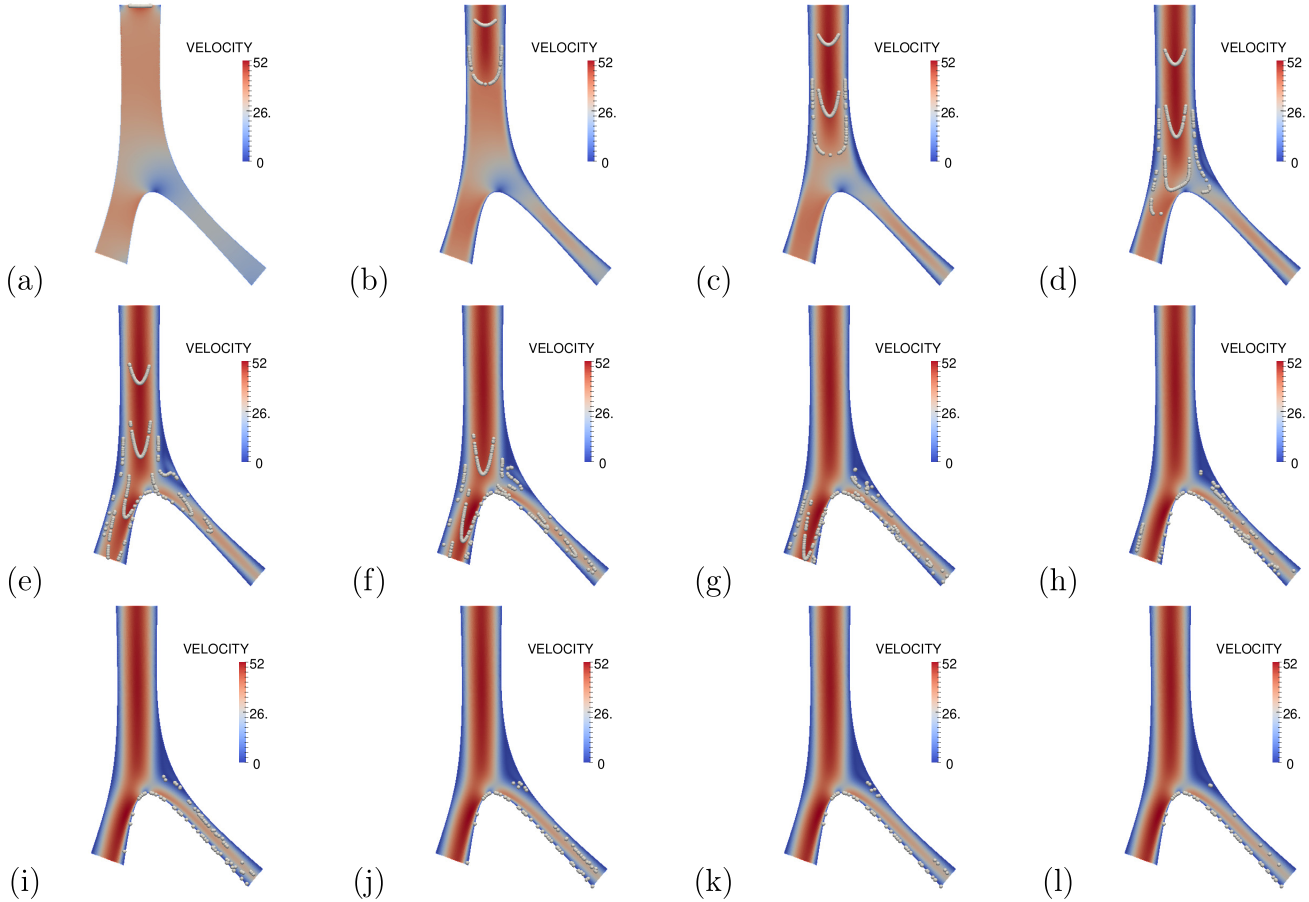

(a) (b) (c) (d)
(e) (f) (g) (h)
(i) (j) (k) (l)

Figure 6.4: Dynamics of the particles with the air velocity, at time $t = 0.00, 0.08, 0.16, ..., 0.80$ s and at final time $\tau = 1$ s. The colors represent the different range of velocities and the grey dots represent the particles.

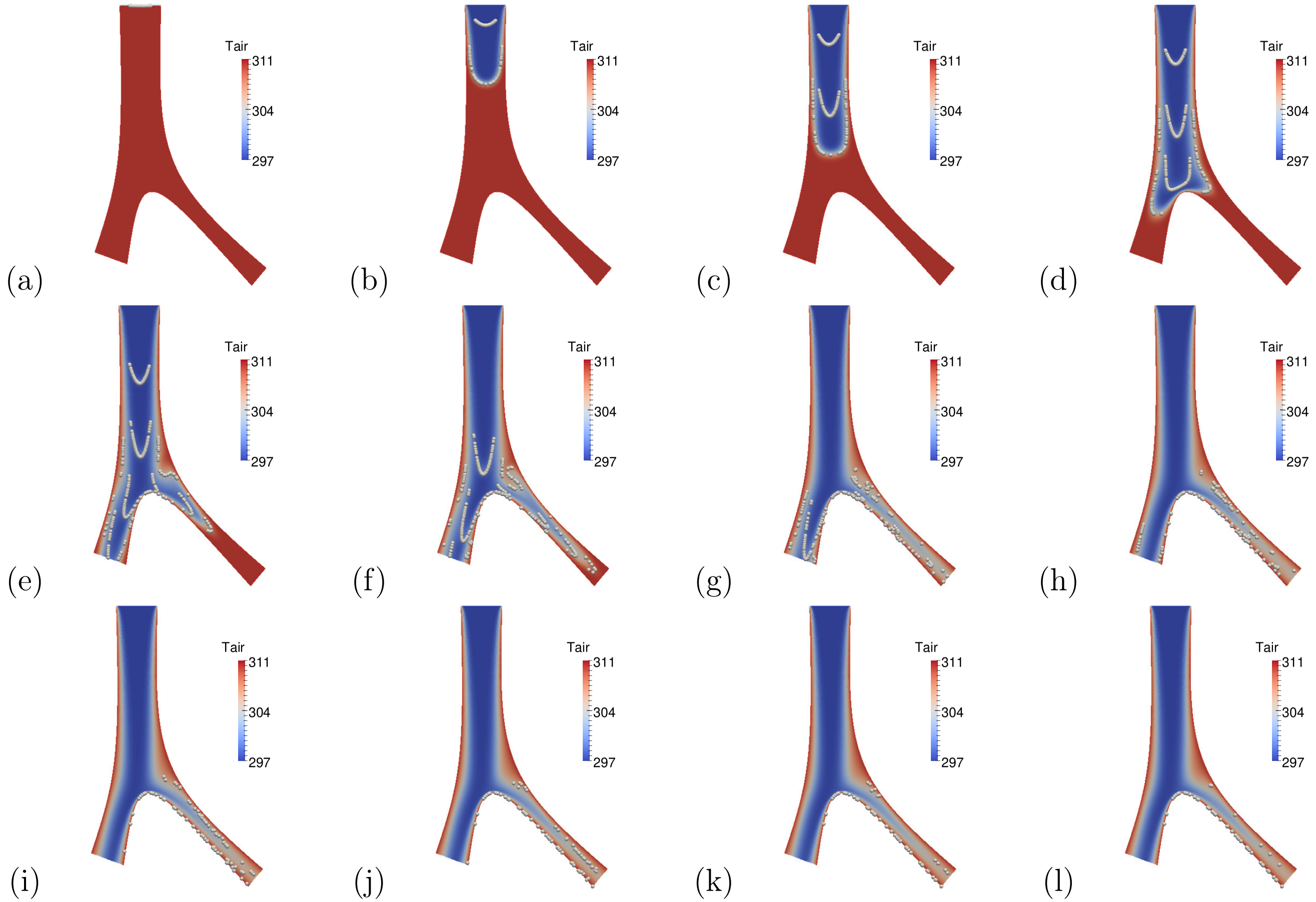
(a) (b) (c) (d)
(e) (f) (g) (h)
(i) (j) (k) (l)

Figure 6.5: Dynamics of the particles with the air temperature, at time $t = 0.00, 0.08, 0.16, ..., 0.80$ s and at final time $\tau = 1$ s. The colors represent the range of air temperature and the grey dots represent the particles.

It is difficult to observe interesting details about the air temperature after each aerosol releases on Figure 6.5. Figure 6.6 allows to have a better understanding of the evolution of the air temperature T_{air}. We can observe an air temperature increase at the location of the particles for all aerosol releases except for the first one. This effect comes from the water vapor mass exchange between the humidified air and the droplets.

Figure 6.6: Local effects of the aerosol on the air temperature at time $0.25 + \Delta t$ (in seconds), with the plot of the particles (left) and without (right).

Let us now focus on the aerosol particles. The droplets trajectories obtained with our model are shown on Figure 6.7. In this particular case, the majority of the droplets (348 over 500) has left the domain by the left branch as expected because of its diameter. It is the most natural way out for the aerosol. The remaining particles are distributed as follow: 98 go out through the right branch, 47 deposit on the wall and the last remaining 7 are still in the domain at the final time.

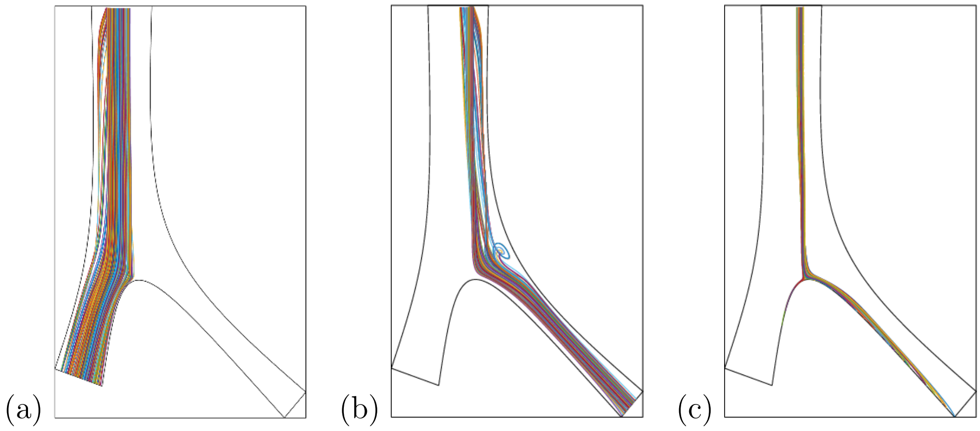

Figure 6.7: Particle trajectories (a) towards the left branch, (b) towards the right branch, (c) deposition.

Finally, we observe the evolution of the radius and of the temperature of the aerosol particles. In one of our initial distribution (Figure 6.8), the droplets from the first release do not behave in the same way as throse from the following releases. Indeed, the particles radius grows slowler than in most of the other releases. This behavior is confirmed with the evolution of the temperature. Indeed, even if the temperature of the injected particles is initially 297 K, they almost instantaneously reach 310 K due to the temperature of the surrounding air. The other releases spread in a cooler air (Figure 6.5) and hence are not submitted to the same thermal shock.

Interestingly, on Figure 6.8, we can observe that for all releases, except for the first one, there is a temperature jump. For the second release, this jump happens around 0.25 s, which is approximatively the time when the particles go into the branches with diameters significantly smaller than the one of the trachea (see Figure 6.4). There, the influence of the walls is stronger and increase the particles temperature.

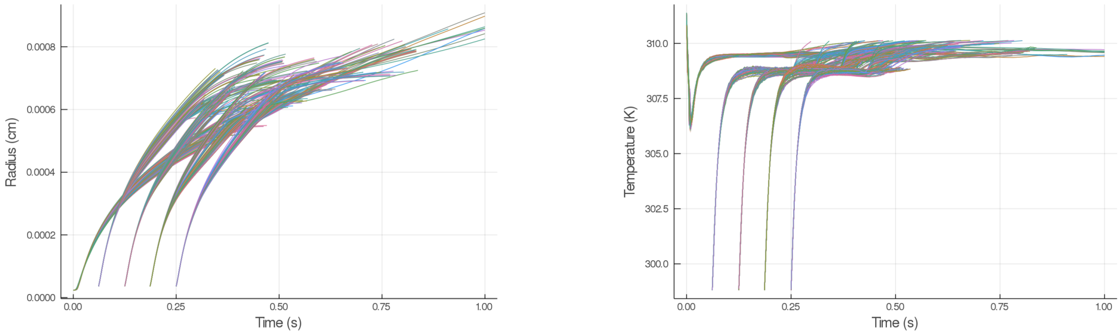

Figure 6.8: Radius (left) and temperature (right) sevolution of all the particles with respect to time.

6.3.3 Comparison of three models

Three different models are defined to study the role of the evolution of the radius and of the temperature of the aerosol particles on the deposit of the droplets. The first model includes all the effects related to aerosol size and temperature variation. It is the complete model previously defined and will be referred to as the (A) model:

$$\text{(A)}\begin{cases} \partial_t f + v \cdot \nabla_x f + \mathrm{div}_v[(\alpha(u-v)+g)f] + \partial_r(af) + \partial_T(bf) = 0, \\ \varrho_{\mathrm{air}}[\partial_t u + (u \cdot \nabla_x u)] - \eta \Delta_x u + \nabla_x p = 0, \quad \mathrm{div}_x\, u = 0, \\ \varrho_{\mathrm{air}}[\partial_t Y_{\mathrm{v,air}} + (u \cdot \nabla_x) Y_{\mathrm{v,air}}] - \mathrm{div}_x(D_{\mathrm{v}}(T_{\mathrm{air}}) \nabla_x Y_{\mathrm{v,air}}) = S_Y, \\ \varrho_{\mathrm{air}} c_{P_{\mathrm{air}}}[\partial_t T_{\mathrm{air}} + (u \cdot \nabla_x) T_{\mathrm{air}}] - \kappa_{\mathrm{air}} \Delta_x T_{\mathrm{air}} = S_T. \end{cases}$$

The second model, referred to as the (B) model does not include temperature evolution ($b = 0$):

$$\text{(B)}\begin{cases} \partial_t f + v \cdot \nabla_x f + \mathrm{div}_v[(\alpha(u-v)+g)f] + \partial_r(af) = 0, \\ \varrho_{\mathrm{air}}[\partial_t u + (u \cdot \nabla_x u)] - \eta \Delta_x u + \nabla_x p = 0, \quad \mathrm{div}_x\, u = 0, \\ \varrho_{\mathrm{air}}[\partial_t Y_{\mathrm{v,air}} + (u \cdot \nabla_x) Y_{\mathrm{v,air}}] - \mathrm{div}_x(D_{\mathrm{v}}(T_{\mathrm{air}}) \nabla_x Y_{\mathrm{v,air}}) = S_Y. \end{cases}$$

Finally, the last model, referred to as the (C) model does not include size and temperature variation ($a = 0$ and $b = 0$):

$$\text{(C)} \left\{ \begin{array}{l} \partial_t f + v \cdot \nabla_x f + \mathrm{div}_v[(\alpha(u-v) + g)f] = 0, \\ \varrho_{\mathrm{air}}[\partial_t u + (u \cdot \nabla_x u)] - \eta \Delta_x u + \nabla_x p = 0, \quad \mathrm{div}_x\, u = 0. \end{array} \right.$$

Let us now compare the radius and the temperature time evolutions of specific droplets of the second release in the three models. We chose to plot three particles with different outcomes in model (A), the first leaves the domain through the left branch (see Figure 6.9), the second leaves the domain through the right branch (see Figure 6.10) and finally the last one deposits (see Figure 6.11). These three particles have also different outcomes depending on the model used. Indeed the second particle, in models (A) and (C), exits the domain by the right branch but deposits in model (B). The third droplet chosen deposits in models (A) and (B) but exit the domain through the right branch in model (C). Finally, we obtain the same outcome for the three models with the first particle leaving the domain through the left branch.

We focus first on the behavior of the temperature. Since, by definition, there are no evolution of the temperature in the (B) and (C) model, it remains constant, whereas in the (A) model, the particle temperature grows until it (approximatively) reaches T_{wall}. This may seem peculiar since the second release of aerosols enters the domain at 297 K and evolves in a cooler air. These temperature variations cannot be explained by the ambiant air temperature. Consequently, it means that they are triggered by hygroscopic phenomena. This leads us to study more carefully the evolution of the droplet radius. We can observe that the model (B) induces a larger size growth than the model (A). This could explain the deposit of the second particle considered in model (B) instead of leaving through the right branch in model (B). The hygroscopic effects imply radius variations in the models (A) and (B), but a part of this variation existing in the model (B) also affects the temperature in the model (A). This justifies why the radius in the model (A) is smaller than in the model (B).

We provide some statistics about the evolution of the radius and of the temperature for the three models (see Table 6.2). From ten initial aerosol distributions, we can compute the mean radius and temperature of the droplets at the final time. When a particle is deposited or has left the domain, the radius and the temperature remain constant until the end of the simulation. We also compute the mean percentage of deposited particles and droplets reaching the boundaries Γ^{out} among the 500 droplets and the corresponding mean event times. As shown on Figures 6.9-6.11, the particles mean radius for the model (A) is between the ones from the model (B) and (C). The radius growth in model (A) is significant compared to model (C), it seems to be the main reason for the larger aerosol deposit in model (A). Moreover the models (A) and (C) have closer mean behaviors, which may imply that the model (B) is not relevant here.

Finally, we compute the mean radius for the models (A) and (B) depending on the position of the particles (deposit, left/right exit) at the final time (see Table 6.3). The variations of the radius can be linked to the mean event times in Table 6.2. In the model (A), the particles going out through the right branch stay longer in the

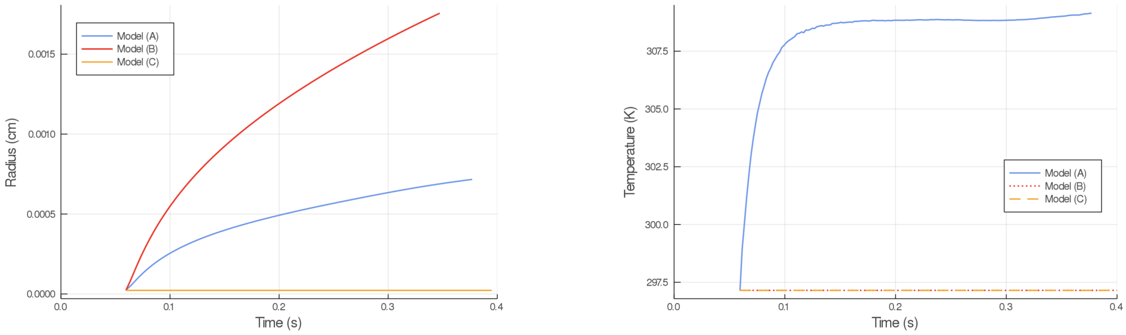

Figure 6.9: Radius (left) and temperature (right) evolution of a droplet which goes out through the left branch in models (A), (B) and (C).

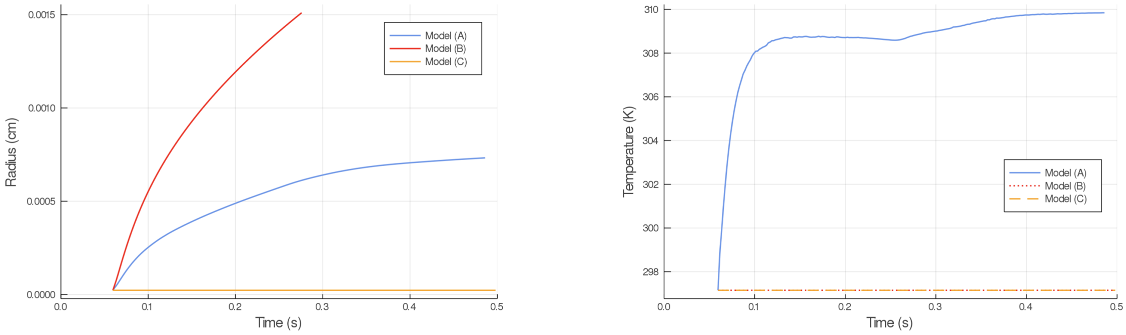

Figure 6.10: Radius (left) and temperature (right) evolution of a droplet which goes out through the right branch in models (A) and (C) and deposits in model (B).

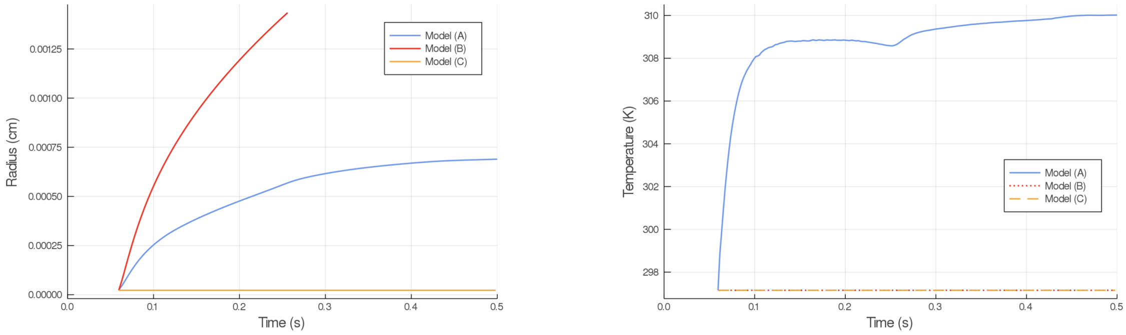

Figure 6.11: Radius (left) and temperature (right) evolution of a droplet which deposits in models (A) and (B) but goes out through the right branch in model (C).

Models	(A)	(B)	(C)
Mean radius (cm)	6.55×10^{-4}	1.67×10^{-3}	2.25×10^{-5}
Mean temperature (K)	309	297	297
Deposited particles	7.6 %	35.5 %	0.0 %
Left exiting particles	69.0 %	64.5 %	69.6 %
Right exiting particles	22.4 %	0.0 %	24.7 %
Mean depos. time (s)	0.409	0.270	–
Mean left exit time (s)	0.289	0.261	0.296
Mean right exit time (s)	0.509	–	0.461

Table 6.2: Statistics in the reference case. The temperature in this case are $T_{\mathrm{air,init}} = 310$ K, $T_{\mathrm{air}}^{\mathrm{in}} = 297$ K, $T_{\mathrm{wall}} = 310$ K. We assume that we have 5 injections of 100 particles each with a representativity $\omega = 10^4$ periodically released between the initial time and $t = 0.25$ s. The initial radius of particles is assumed to be $r = 2.25 \times 10^{-5}$ cm.

domain, thus undergoing a larger radius growth. In the model (B), deposit or exit happen more or less at the same time, leading to very similar radii for the particles.

	Mean radius (cm)		
	Model (A)	Model (B)	Model (C)
Deposited particles	6.43×10^{-4}	1.68×10^{-3}	–
Left exiting particles	6.25×10^{-4}	1.67×10^{-3}	2.25×10^{-5}
Right exiting particles	7.42×10^{-4}	–	2.25×10^{-5}

Table 6.3: Statistics for the particles depending on their future (depositing/exiting).

6.4 Conclusion

We described and studied a model that describes the trajectories of aerosol droplets in the first bifurcation of the lung. It models the evolution of the radius and temperature of the droplets and gives us an appreciation on the deposition of the particles on the bronchus walls.

Our results allowed to point out the relevance of the model (A) compared to the other two models (B) and (C) to properly take into account the hygroscopic effects on aerosols in the airways. However, there are still more situations to investigate. The first concerns the numerical subcycling. Indeed, let us observe the source term modelled by the function b equation (6.2). This function drives the evolution of the temperature of the droplets and is composed of two terms:

$$b_1(r, T, T_{\mathrm{air}}(t,x)) = -\frac{3}{\varrho_{\mathrm{d}}(r) c_{P_{\mathrm{d}}} r} Q_{\mathrm{d}}(r, T, T_{\mathrm{air}}(t,x)),$$

and

$$b_2(r, T, Y_{\mathrm{v,air}}(t,x), T_{\mathrm{air}}(t,x)) = -\frac{3}{\varrho_{\mathrm{d}}(r) c_{P_{\mathrm{d}}} r} L_{\mathrm{v}} N_{\mathrm{d}}(r, T, Y_{\mathrm{v,air}}(t,x)).$$

The two functions b_1 and b_2 have opposite signs but are of the same order of magnitude, around $2 \times 10^5\,\mathrm{K} \cdot \mathrm{s}^{-1}$ at the initial time (see Figure 6.12). The function b, which is the sum of the two previous functions has a value around $400\,\mathrm{K} \cdot \mathrm{s}^{-1}$ at the initial time (see Figure 6.12). The model behaves nicely with respect to the temperature (see Figure 6.13), because we used a very fine subcycling time step to guarantee numerical accuracy in the description of the thermal effects. However, from the computational viewpoint, this can probably be improved.

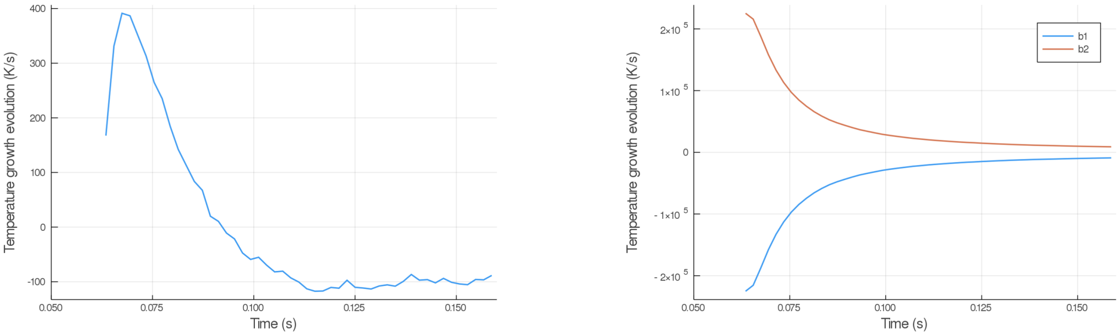

Figure 6.12: Order of magnitude of each thermal effect b (left) and b_1 and b_2 (right) for a given particle.

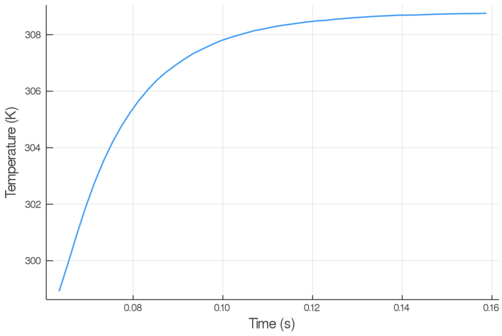

Figure 6.13: Temperature evolution of the chosen particle in Figure 6.12.

The second investigation could be the addition of the excipient. Our numerical computations were made with the assumption that no excipient were present in the droplets. However, since standard values of ϱ_{drug} and ϱ_{ex} are similar (see Table 6.1), the addition of the excipient might not imply major behavior changes on the aerosol.

The next investigation could be the extension of the domain. Our computational domain represents only the trachea and the first bifurcation in the lung. We could study our model behavior within other domains, not necessarily with a vertical main axis since deeper bronchi can have different orientation angles, to understand the effect of the geometrical variability. Furthermore, we only studied the airflow in this domain during inspiration. It could be interesting to add the expiration. However, it is a difficult task because of the unclear boundary conditions on the function f at Γ^{out}.

Finally, to study more faithfully the model, we should extend our two-dimensionnal model into a three-dimensional one. We know that two-dimensional simulations tend to increase the aerosol deposit [16] compared to three-dimensional models [15].

This chapter was the subject of a proceeding published in ESAIM: Proceedings and surveys. The references are:

Fluid-kinetic modelling for respiratory aerosols with variable size and temperature.

L. Boudin[1,*], C. Grandmont[2,*], B. Grec[3,*], S. Martin[3,*], A. Mecherbet[4,*], F. Noël[5,*].

CEMRACS 2018 – Numerical and mathematical modeling for biological and medical applications: deterministic, probabilistic and statistical descriptions, ESAIM: Proceedings and Surveys. 2020.

[1] Sorbonne Université, Université Paris-Diderot SPC, CNRS, Inria, Laboratoire Jacques-Louis Lions, équipe REO, F-75005 Paris, France.

[2] Inria, Sorbonne Université, Université Paris-Diderot SPC, CNRS, Laboratoire Jacques-Louis Lions, éuipe REO, F-75012 Paris, France.

[3] MAP5, CNRS UMR 8145, Sorbonne Paris Cité, Université Paris Descartes, F-75006 Paris, France.

[4] IMAG, University of Montpellier, CNRS, Montpellier, France.

[5] Laboratoire JA Dieudonné, UMR CNRS 7351, Université Côte d'Azur, Nice, France.

[*] Authors are in alphabetical order.

Chapter 7

Conclusion

The goal of this thesis is to reach a better understanding on how the lung's ventilation can affect the transport of the respiratory gases in the lung whether healthy or infected by a pulmonary infection. For that we have used relatively simple mathematical models to mimic the ventilation by modeling the core physical and morphological properties of the lung.

Our first step was to model the ventilation and the gaseous exchanges with the blood in a young healthy subject in order to have a benchmark close to the physiology. We modeled the respiratory gas transport based on the core physical properties of the human's lung: a tree-like structure of the lung, convective and diffusive transports of oxygen and carbon dioxide and physiology-based exchange surface properties. Then, we described a model that minimizes the power dissipated during the lung's ventilation while fulfilling the body needs in oxygen. Our results showed that the control of ventilation is due to the energy minimization spent during respiration and hence, highly depends on the morphological characteristics of the lung. Futhermore, this study showed that that it is not only accurate for the humans but also for all mammals, for different metabolisms.

In a second part, we extended this study to a non healthy subject. We ask ourselves how this ventilation could be modified by a pulmonary infection. That is why we described and studied a model of the propagation of the infection and of the inflammation bronchi per bronchi in the human's lung. This model was linked to the previous gas transport model which has been modified to take into account the asymmetry of the bifurcations induced by the inflammation of the bronchi. Our first results showed that the localization in the lung of the transition between the convection and the diffusion, the localization of the infection and its intensity play a major part in the amount of oxygen exchanged with the blood.

Finally, to cure this infection, the immune system can be helped with drugs delivered in the form of aerosol droplets. The study of the amount of deposited particles allows to have a better understanding in the efficacy of such a treatment. We modeled the trajectory of the aerosol particles in the first bifurcation of the lung by taking into account the evolution of their radius and their temperature. Our results showed that the hygroscopic properties of the droplets and the evolution of their temperature affect significantly the deposit of the particles.

In this work, we obtained a complete model that optimizes the ventilation in humans as well as in all mammals, whether they are healthy or with an infected lung. In future works, we could couple this model to the aerosol particles deposition model during the propagation of a pulmonary infection. This would therefore make it possible to observe the changes in the air distribution as well as their influence on the deposition of the particles. This approach could be a first step towards a better understanding of the animal models for aerosols [109, 39, 4]. Indeed, our model would allow to mimic and understand the change of size between the animal and the human. The numerical model then could replace the animal model in order to be more ethical.

This work is part of the projects of the ANR Virtual Chest and of the Vader Center in UCA which aims to promote the use of mathematics and numerical methods to better understand how physical and chemical laws allow breathing. Different projects are developed such as the study of the ventilation at exercise in master athletes, the modeling of the lung's geometry for biomedicals applications, the study of the lung's evolution, the study of the link between music and respiration and finally the development of a numerical lung for chest physiotherapy.

Finally, this work clearly shows the importance of interdisciplinarity and the usefulness of a mathematical approach to analyze and understand biophysical phenomena such as the influence of the ventilation on the transport properties in the lung.

Appendix A

Numerical Schemes

This appendix presents the numerical schemes used for the computation of the numerical solutions for the gas transport model presented in the chapter 3 for a healthy lung and in the chapter 5 for an inflamed lung. We also present the optimization algorithm to compute the optimal ventilation in the chapter 4.

A.1 Gas transport in a healthy lung

A.1.1 Gas transport numerical scheme

In chapter 3, we described a model for the gas transport in the lung. In this section, we will describe the numerical scheme used to compute the numerical approximations of our model. Let us first recall that we assumed that the partial pressures of the respiratory gases are described in each generation of the lung i by the equation,

$$\frac{\partial P_i}{\partial t} - \frac{D}{l_i^2}\frac{\partial^2 P_i}{\partial x^2} + \frac{u_i(t)}{l_i}\frac{\partial P_i}{\partial x} + \beta_i P_i = \beta_i P_{\text{blood}}, \ \ \forall x \in [0,1]. \tag{A.1}$$

Let us recall that D is the diffusion coefficient of the gas in the air, l_i is the length of the bronchus in generation i, $u_i(t)$ is the air flow velocity in generation i and β_i is an exchange coefficient defined in chapter 3 (equation (3.3))

We complete the equation with the following condition at the bifurcations,

$$\begin{cases} P_i(t,1) = P_{i+1}(t,0), \\ -DS_i \dfrac{\partial P_i(t,1)}{\partial x} = -2DS_{i+1}\dfrac{\partial P_{i+1}(t,0)}{\partial x}, \end{cases} \tag{A.2}$$

and the following boundaries conditions,

$$\begin{cases} P_0(t,0) = P_{\text{air}} \\ -D\dfrac{\partial P_N}{\partial x}(t,1) = \alpha k \varrho_s \left(P_N(t,1) - P_{\text{blood}}(t,1)\right). \end{cases} \tag{A.3}$$

We recall that S_i is the lumen area of the bronchus in generation i, P_{air} is the partial pressure of the gas in the air, α is an exchange coefficient (see equation (3.1)), k is the ratio relating partial pressure of the gas to its concentration in water and

ϱ_s is the amount of exchange surface per unit of alveolar duct surface, all previously defined in the chapter 3.

Let us now define the space domaine for each generation i $\Omega_i = [0,1]$. This domain is divided in M intervals each of length $\Delta x = \frac{1}{M}$. The time span $[0, T_{\text{final}}]$, where T_{final} is the final time, is divided into L intervals each of length $\Delta t = \frac{T_{\text{final}}}{L}$. Our approximated solution is computed on a mesh where each point of index (j,n) is marked on the space axis by the position $x_j = j\Delta x$ ($j \in [\![0, M]\!]$), and on the time axis by $t^n = n\Delta t$ ($n \in [\![0, L]\!]$). The approximated solution at each mesh nodes is denoted,

$$P^n_{i,j} = P_i(t^n, x_j).$$

To approximate our equation (A.1), we look for an approximation of the first and second derivative in space and of the first derivative in time. For that, we use the implicit finite differences scheme. The first derivative in time is then approximated by,

$$\frac{\partial P_i}{\partial t}(t^n, x_j) \approx \frac{P^{n+1}_{i,j} - P^n_{i,j}}{\Delta t}.$$

The second derivative in space is approximated by,

$$\frac{\partial^2 P_i}{\partial x^2}(t^n, x_j) \approx \frac{P^{n+1}_{i,j+1} - 2P^{n+1}_{i,j} + P^{n+1}_{i,j-1}}{\Delta x^2}.$$

The approximation of the first derivative in space depends on the sign of the parameters in front of this derivative, here $\frac{u_i(t)}{l_i}$. We use an upwind scheme and hence, if $u_i(t) > 0$, the first derivative is approximated by,

$$\frac{\partial P_i}{\partial x}(t^n, x_j) \approx \frac{P^{n+1}_{i,j} - P^{n+1}_{i,j-1}}{\Delta x},$$

and if $u_i(t) < 0$, the first derivative is approximated by,

$$\frac{\partial P_i}{\partial x}(t^n, x_j) \approx \frac{P^{n+1}_{i,j+1} - P^{n+1}_{i,j}}{\Delta x}.$$

Finally, we obtain the following finite different scheme,

$$\frac{P^{n+1}_{i,j} - P^n_{i,j}}{\Delta t} - \frac{D}{l_i^2}\frac{P^{n+1}_{i,j+1} - 2P^{n+1}_{i,j} + P^{n+1}_{i,j-1}}{\Delta x^2}$$
$$+\frac{u_i(t)}{l_i}\left(\frac{P^{n+1}_{i,j} - P^{n+1}_{i,j-1}}{\Delta x}\mathbf{1}_{u_i>0} + \frac{P^{n+1}_{i,j+1} - P^{n+1}_{i,j}}{\Delta x}\mathbf{1}_{u_i<0}\right) + \beta_i P^{n+1}_{i,j} = \beta_i P^n_{\text{blood},j}.$$

It can also be written as follow,

$$P^{n+1}_{i,j}\left(1 + \frac{2D\Delta t}{l_i^2\Delta x^2} + \frac{u_i(t)\Delta t}{l_i\Delta x}(\mathbf{1}_{u_i>0} - \mathbf{1}_{u_i<0}) + \beta_i\right)$$
$$+P^{n+1}_{i,j+1}\left(-\frac{D\Delta t}{l_i^2\Delta x^2} + \frac{u_i(t)\Delta t}{l_i\Delta x}\mathbf{1}_{u_i<0}\right) + P^{n+1}_{i,j-1}\left(-\frac{D\Delta t}{l_i^2\Delta x^2} - \frac{u_i(t)\Delta t}{l_i\Delta x}\mathbf{1}_{u_i>0}\right)$$

$$= P^n_{i,j} + \Delta t \beta_i P^n_{\text{blood},j}$$

The computation of the partial pressure of the oxygen in the blood is computed thanks to a Newton algorithm such that,

$$\begin{aligned} c_b(P^n_{\text{blood},O_2,j}) =& \alpha(P^n_{i,j} - P^n_{\text{blood},j}) \\ & - 4Z_0 \left(f(P^n_{\text{blood},O_2,j}) - f(P_{aO2}) \right) v_s + \sigma v_s (P^n_{\text{blood},j} - P_{aO_2}) \\ =& 0. \end{aligned}$$

The recurrence relation for the Newthon method writes,

$$x_{n+1} = x_n - \frac{c_b(x_n)}{c'_b(x_n)}.$$

This algorithm stops once $|c_b(x_n)| < \epsilon$, for $\epsilon > 0$ small enough.

The computation of the partial pressure of the carbon dioxide in the blood, is computed easily thanks to this expression,

$$\begin{aligned} \alpha(P^n_{i,j} - P^n_{\text{blood},CO_2,j}) = & \left(P^n_{\text{blood},CO_2,j} - P_{aCO_2} \right) \sigma \, v_s \, \left(1 + 10^{(pH - pK)} \right) \\ & \times \left(1 - \frac{0.0289 \, Z_0}{(3.352 - 0.456 \, SO_2) \times (8.142 - pH)} \right). \end{aligned}$$

Then, let us compute the approximation for the bifurcations conditions (A.2),

$$\begin{cases} P^n_{i,M} = P^n_{i+1,0}, \\ -DS_i \dfrac{P^n_{i,M} - P^n_{i,M-1}}{\Delta x} = -2DS_{i+1} \dfrac{P^n_{i+1,1} - P^n_{i+1,0}}{\Delta x}. \end{cases}$$

Finally, the boundary conditions (A.3) are approximated by,

$$\begin{cases} P^n_{0,0} = P_{\text{air}} \\ -D \dfrac{P^n_{N,M} - P^n_{N,M-1}}{\Delta x} = \alpha k \varrho_s \left(P^n_{N,M} - P^n_{\text{blood},M} \right). \end{cases}$$

We assumed that the human lung could be idealized by a symmetric dichotomic bifurcating tree. Thanks to this assumption, we only need to compute the partial pressure of the respiratory gases for one path from the trachea to an acinus in the lung. Consequently, we only have to resolve the equation for a single bronchus in each generation. At each time step, we resolve a linear system. The vectors of this linear system have a length of $K = (N+1) \times (M+1)$, where $N+1$ is the number of generations in the lung ($N+1 = 23$ for humans). Since we have to inverse a matrix of size $K \times K$ at each time step, we then have a total complexity of our numerical scheme of $O(K \times K \times (L+1))$.

A.1.2 Oxygen and carbon dioxide flow

In the previous section, we explained how to compute the partial pressure of the respiratory gases in the lung and in the blood at each mesh point. Now, we can compute the gases flows exchange with the blood during a respiratory cycle. Let us recall that the flow is computed as follow,

$$f(A,T) = \sum_{i=G}^{N} \frac{2^i}{T} \int_{t_C}^{t_C+T} \int_0^{l_i} \gamma \left(P_i(t,x) - P_{\text{blood}}\right) \mathrm{d}x \, \mathrm{d}t. \tag{A.4}$$

We recall that T is the period of the ventilation, γ is an exchange coefficient defined in chapter 3 (see equation 3.6) and G is the number of generation in the bronchial tree.

We approximate the integral with the rectangle rule where we divide our integral on each time step and each space step.

We then obtain,

$$f(A,T) \approx \sum_{i=G}^{N} \frac{2^i}{T} \sum_{n=0}^{L} \sum_{j=0}^{M} \Delta t \Delta x l_i \gamma \left(P_{i,j}^n - P_{\text{blood},j}^n\right).$$

A.2 Optimal ventilation

In chapter 4, our goal was to optimize the ventilation in order to minimize the power spent during breathing while fulfilling the body's needs in oxygen. In this section, we will describe our algorithm. First, let us recall the expression of the power spent during breathing,

$$\begin{aligned} \mathcal{P}(A,T) &= \mathcal{P}_e(A,T) + \mathcal{P}_v(A,T) \\ &= \mathcal{P}_e(A,T)\left(1 + \frac{\pi^2}{2T} RC\right) = \frac{A^2 S_0^2 T}{2\pi^2 C}\left(1 + \frac{\pi^2}{2T} RC\right). \end{aligned} \tag{A.5}$$

The function $(A,T) \to \mathcal{P}(A,T)$ is to be minimized relatively to the ventilation amplitude A and the period T with the constraint $f_{O_2}(A,T) = \dot{V}_{O_2}$, where $\dot{V}_{O_2}$ is the desired oxygen flow to the blood.

Practically, the ventilation period T and the amplitude A can be linked through the constraint on the flow of oxygen to the blood, in the form of a non linear function $T \to A(T)$. The non linear function is the result of the transport model of oxygen. For a given value of the period, only one value of the amplitude is possible in order to check the constraint (see Figure 4.2). For each period T, we look for the corresponding amplitude A by solving thanks to the secant method,

$$c(A) = f_{O_2}(A,T) - \dot{V}_{O_2} = 0.$$

The recurrence relation for the secant method writes,

$$x_{n+1} = x_n - \frac{x_n - x_{n-1}}{c(x_n) - c(x_{n-1})} c(x_n).$$

This algorithm stops once $|c(x_n)| < \epsilon$, for $\epsilon > 0$ small enough.

Consequently, with the oxygen flow constraint, the optimization problem is unidimensional and we search for the minimum of the function $\mathcal{P}$ or the zero of its derivative relatively to T,

$$\frac{\partial \mathcal{P}}{\partial T}\left(A(T), T\right) = \left(A'(T)\left(\frac{1}{2} + \frac{T}{\pi^2 RC}\right) + \frac{A(T)}{2\pi^2 RC}\right) A(T) R S_0^2 = 0.$$

Since we impose a positive oxygen flow, the value $A(T)$ must be different than zero. Consequently we only need to search the zero of the function,

$$\mathcal{D}(T) = A'(T)\left(\frac{1}{2} + \frac{T}{\pi^2 RC}\right) + \frac{A(T)}{2\pi^2 RC}.$$

Since the computation of the function A is numerical, we can approximate its derivative by,

$$A'(T) \approx \frac{A(T+m) - A(T)}{m},$$

where $m > 0$ tends to 0.

The optimal ventilation is then computed thanks to the secant method in order to obtain the zero of the function $\mathcal{D}(T)$.

The secant method converges if the initial points x_0 and x_1 are sufficiently close to the root of our function. The order of convergence of this method is the golden ratio which is approximated by 1.618. Finally, the resolution time will depends on the initial points, the time step and the space step used for the computation of the gases flow exchanged with the blood and on the desired precision ϵ. In pratice, the order of magnitude of the resolution time is around 15 to 30 minutes with initial points close to the optimal value and a relative precision of $\epsilon = 10^{-8}$ on a 3.1 GHz dual-core CPU.

A.3 Gas transport in an inflamed lung

In the chapter 5, we assumed that the lung was subjected to a pulmonary infection and to the propagation of the inflammation in the bronchi. This leads to the asymmetry of some of the bifurcations in the lung. In this section, we will present the numerical scheme used in order to compute the partial pressure of the respiratory gases in an inflamed lung.

Since the bifurcations are no longer symmetric, we can not anymore compute the partial pressure of the gases in only one path of the lung. Our first step is then to compute the number of the different paths required to compute the partial pressure of the gases in the whole lung. This step is important as we do not want to compute the partial pressure of the respiratory gases in each bronchus of the whole lung. We assume that the bronchi are ordered numerically (see Figure A.1). For example, we suppose that our tree has four generations and that five bronchi are inflamed. We can observe on Figure A.1 that in this case, five paths have to be computed to model the partial pressure in the whole lung. Indeed, three paths result from the three inflamed bronchi in the fourth generation, one path results from the bronchus $(3, 3)$ connected to an inflamed bronchus and finally the last path is an healthy one.

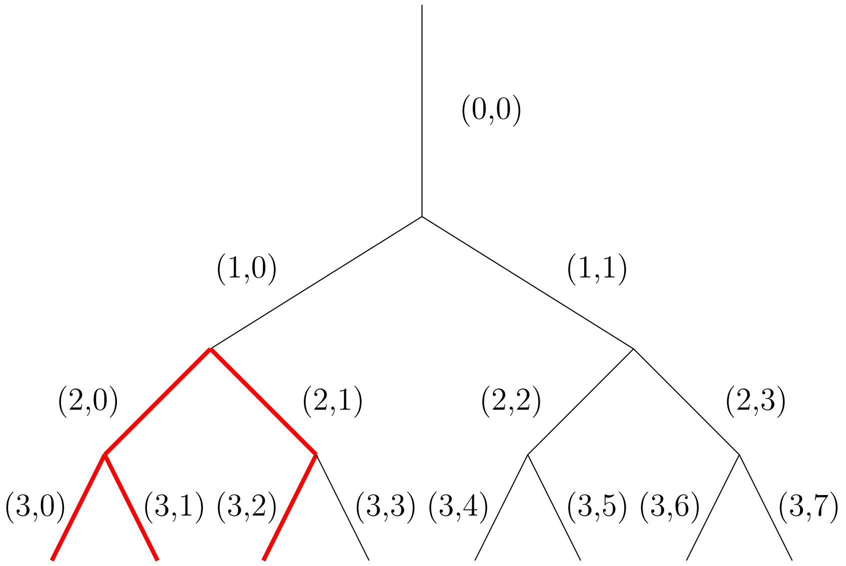

Figure A.1: Tree of 4 generations mimicking a small lung. The numbers represent the indices of the bronchi. The red bronchi are inflamed.

Now that we know the number of paths required to compute the partial pressure in the whole lung, we can use the finite differences scheme to compute numerically the approximated solution of the equation,

$$\frac{\partial P_{c,i}}{\partial t} - \frac{D}{l_i^2}\frac{\partial^2 P_{c,i}}{\partial x^2} + \frac{u_{c,i}(t)}{l_i}\frac{\partial P_{c,i}}{\partial x} + \beta_{c,i}P_{c,i} = \beta_{c,i}P_{\text{blood}}, \quad \forall x \in [0,1]. \tag{A.6}$$

The index c corresponds to the number of the paths and i represents the generation in the lung. As in section A.1, we use the following scheme,

$$\begin{aligned} &P_{c,i,j}^{n+1}\left(1 + \frac{2D\Delta t}{l_i^2\Delta x^2} + \frac{u_{c,i}(t)\Delta t}{l_i\Delta x}(\mathbf{1}_{u_{c,i}>0} - \mathbf{1}_{u_{c,i}<0}) + \beta_{c,i}\right) \\ &+P_{c,i,j+1}^{n+1}\left(-\frac{D\Delta t}{l_i^2\Delta x^2} + \frac{u_{c,i}(t)\Delta t}{l_i\Delta x}\mathbf{1}_{u_{c,i}<0}\right) + P_{c,i,j-1}^{n+1}\left(-\frac{D\Delta t}{l_i^2\Delta x^2} - \frac{u_{c,i}(t)\Delta t}{l_i\Delta x}\mathbf{1}_{u_{c,i}>0}\right) \\ &= P_{c,i,j}^n + \Delta t\beta_i P_{\text{blood},c,j}^n. \end{aligned}$$

The equation (A.6) is completed with the following boundary conditions,

$$\begin{cases} P_{c,0}(t,0) = P_{\text{air}} \\ -D\dfrac{\partial P_{c,N}}{\partial x}(t,1) = \alpha k\varrho_s\left(P_{c,N}(t,1) - P_{\text{blood}}(t,1)\right). \end{cases} \tag{A.7}$$

It is approximated as in section A.1 by,

$$\begin{cases} P_{c,0,0}^n = P_{\text{air}} \\ -D\dfrac{P_{c,N,M}^n - P_{c,N,M-1}^n}{\Delta x} = \alpha k\varrho_s\left(P_{c,N,M}^n - P_{\text{blood},c,M}^n\right). \end{cases}$$

Number of inflammed bronchi	Resolution time
0	9.5 s
1	13 s
6	25 s
12	37 s
62	149 s ($\sim$ 2 min 30)
128	313 s ($\sim$ 5 min)
256	697 s ($\sim$ 12 min)
511	1771 s ($\sim$ 30 min)

Table A.1: Resolution time of the computation of the oxygen partial pressure in an idealized human's lung during depending on the number of infected bronchi.

Finally, the equation (A.6) is also completed by the conditions at the bifurcations,

$$\begin{cases} P_{c,i}(t,1) = P_{c,i+1}(t,0), \\ S_{c,i}\dfrac{\partial P_{c,i}(l_i,t)}{\partial x} = S_{c,i+1}\dfrac{\partial P_{c,i+1}(0,t)}{\partial x} + S_{\tilde{c},i+1}\dfrac{\partial P_{\tilde{c},i+1}(0,t)}{\partial x}, \end{cases} \tag{A.8}$$

where $\tilde{c}$ is the path that takes into account the bronchus connected to the one in path c of generation $i+1$. Let us consider again our previous example, we assume that the path going from the bronchus $(0,0)$ to $(3,0)$ has for index 1 and that the path going from the bronchus $(0,0)$ to $(3,1)$ has for index 2. We focus on the bifurcation where the bronchus $(2,0)$ divides into bronchus $(3,0)$ and $(3,1)$. Here if $c=1$, then we have $\tilde{c}=2$ and vice versa.

Finally, this bifurcation conditions can be approximated by,

$$\begin{cases} P^n_{c,i,M} = P^n_{c,i+1,0}, \\ S_{c,i}\dfrac{P^n_{c,i,M} - P^n_{c,i,M-1}}{\Delta x} = S_{c,i+1}\dfrac{P^n_{c,i+1,1} - P^n_{c,i+1,0}}{\Delta x} + S_{\tilde{c},i+1}\dfrac{P^n_{\tilde{c},i+1,1} - P^n_{\tilde{c},i+1,0}}{\Delta x}. \end{cases}$$

We have to resolve for each path the equation for a single bronchus in each generation. As for the healthy lung in section A.1 we have to resolve a linear system at each time step. The vectors of this linear system have a length of $K = NbP \times (N+1) \times (M+1)$, where $N+1$ is the number of generations in the lung ($N+1 = 23$ for humans) and NbP is the number of paths. Since we have to inverse a matrix of size $K \times K$ at each time step, we then have a total complexity of our numerical scheme of $O(K \times K \times (L+1))$. It becomes more and more difficult to resolve this system as the number of inflamed bronchi increases. Indeed, if each bronchus of the human lung is inflamed then we have to compute the partial pressure in all the bronchi of the lung *i.e.* in 2^{23} bronchi which becomes complicated in terms of memory and of resolution time. For example, Table A.3 references the resolution time depending on the number of infected bronchi. This computations were made on a 3.1 GHz dual-core CPU, with a adimensionalized space step of $\Delta x = 0.01$ and a time step of $\Delta t = 0.1$ s where the final time is $T_{\text{final}} = 10$ s.

Appendix B

Infection model parameters

The equations and parameters detailed here are the ones needed for the infection model described in chapter 5. They come from [91]. We know that when the body detects a pathogen in the tissues (P) or in the blood (P_b), the first reaction of the immune system is to bring white blood cells (here macrophages and neutrophils) to the site of infection. When resting macrophages (M) already present in the tissue come in contact with some pathogens, they become activated (M^*). They can now eliminate pathogens and produce pro-inflammatory (TNF) and anti-inflammatory ($IL10$) cytokines. Pro-inflammatory cytokines migrate into the blood (TNF_b) and send a signal to resting neutrophils (N_b) already present in the blood. Once the signal is received by the neutrophils they become activated (N_b^*). These activated neutrophils have the ability to go in the tissue (N^*) and to fight the pathogens. Furthermore, during this infection, the tissue becomes inflammed (Z) and the presence of radicals (RAD and RAD_b), produced by activated macrophages and neutrophils, can damage the tissue that becomes less functional (TI). This immune response can be modeled by ordinary differential equations,

$$\begin{aligned}
\frac{dP}{dt} =& k_{pg}P\left(1-\frac{P}{P_\infty}\right)-\frac{s_b k_{pb} P}{\mu_b + k_{bp}P} - k_{pm} g_i(M^*) g(P, x_{m*p}, h_{m*p}) \\
& - k_{pn} g_{in}(N^*) g(P, x_{n*p}, h_{n*p}) + d_p(Z)\frac{d_{pb}(P_b) - d_{pt}(P)}{V_T} \\
\frac{dM}{dt} =& s_m - \mu_m M - k_{mtcell} g_i(M) g(TNF, x_t, h_t) \\
& - k_{mrcell} g_i(M) RAD - k_{mp} g_i(M) g(P, x_{mp}, h_{mp}), \\
\frac{dM^*}{dt} =& - \mu_{m*} M^* + k_{mtcell} g_i(M) g(TNF, x_t, h_t) \\
& + k_{mrcell} g_i(M) RAD + k_{mp} g_i(M) g(P, x_{mp}, h_{mp}), \\
\frac{dN^*}{dt} =& - \mu_{n*} N^* - (1-r) k_{pncell} g_i n(N^*) g(P, x_{n*p}, h_{n*p}) + \frac{d_n(Z) N_b^*}{V_T}, \\
\frac{dTNF}{dt} =& - \mu_t TNF - k_{mtmol} g_i(M) g(TNF, x_t, h_t) \\
& + k_{mat} g_{it}(g(M^*, x_{m*t}, h_{m*t})) + \frac{d_{mol}(Z)(TNF_b - TNF)}{V_T},
\end{aligned}$$

$$\begin{aligned}
\frac{dIL10}{dt} =& (-\mu_{imax} + (\mu_{imax} - \mu_{imin}) g(IL10, x_i, h_i)) IL10 \\
&+ \frac{d_{mol}(Z)(IL10_b - IL10)}{V_T} + k_{mai} g_i(g(M^*, x_{m*i}, h_{m*i})), \\
\frac{dRAD}{dt} =& - \mu_r RAD + k_{rtr} RAD\,TI + k_{nar} g_{in}(N^*) + k_{natr} N^*\,TI \\
&+ k_{rntp} N^*\,P\,TI + k_{rtmp} M^*\,P\,TI + \frac{d_{mol}(Z)(RAD_b - RAD)}{V_T}, \\
\frac{dTI}{dt} =& k_{tg} TI \left(1 - \frac{TI}{T_\infty}\right)(TI - a) - k_{rtt} RAD\,TI, \\
\frac{dZ}{dt} =& k_{tz}\left(g(TNF, x_{tz}, h_{tz}) + k_{zti}(1_T I)\right)(1 - Z) - \mu_z Z, \\
\frac{dP_b}{dt} =& k_{pbg} P_b \left(1 - \frac{P_b}{P_{b\infty}}\right) - \frac{s_{bb} k_{pbb} P_b}{\mu_{bb} + k_{bbp} P_b} - k_{pnb} g_{ib}(N_b^*) g(P_b, x_{n*pb}, h_{n*pb}) \\
&+ d_p(Z) \frac{d_{pt}(P) - d_{pb}(P_b)}{V_B}, \\
\frac{dN_b}{dt} =& - \mu_{nb} N_b - k_{ntcell} g_{ib}(N_b) g(TNF_b, x_{tb}, h_{tb}) \\
&- k_{npbcell} g_{ib}(N_b) g(P_b, x_{npb}, h_{npb}) \\
&- k_{nrb} g_{ib}(N_b) RAD_b + s_{nb} + k_{snb} g(cN_b^* + dN^*, x_{snb}, h_{snb}), \\
\frac{dN_b^*}{dt} =& - \mu_{nb*} N_b^* + k_{ntcell} g_{ib}(N_b) g(TNF_b, x_{tb}, h_{tb}) \\
& k_{npb} g_{ib}(N_b) g(P_b, x_{npb}, h_{npb}) + k_{nrb} g_{ib}(N_b) RAD_b \\
&- (1 - r_b) k_{pncell} g_{ib}(N_b^*) g(P_b, x_{n*pb}, h_{n*pb}) - \frac{d_n(Z) N_b^*}{V_B}, \\
\frac{dTNF_b}{dt} =& - \mu_{tb} TNF_b - k_{ntmol} g_{ib}(N_b) g(TNF_b, x_{tb}, h_{tb}) \\
&- \frac{d_{mol}(Z)(TNF - TNF_b)}{V_B}, \\
\frac{dIL10_b}{dt} =& (-\mu_{ibmax} + (\mu_{ibmax} - \mu_{ibmin}) g(IL10_b, x_i, h_i)) IL10_b \\
&+ \frac{d_{mol}(Z)(IL10 - IL10_b)}{V_B}, \\
\frac{dRAD_b}{dt} =& - \mu_{rb} RAD_b + k_{narb} g_{inb}(N_b^*) + \frac{d_{mol}(Z)(RAD - RAD_b)}{V_B}.
\end{aligned}$$

Let us now define the different functions used in these equations. First we have a Hill function that writes,

$$g(v, x, h) = \frac{v^h}{v^h + x^h}.$$

Next, some inhibitions functions are present in the equations, they write,

$$g_i(x) = x\left(\frac{1-c_i}{1+\left(\frac{IL10}{IL10_\infty}\right)^{h_i}} + c_i\right),$$

$$g_{it}(x) = x\left(\frac{1-c_{it}}{1+\left(\frac{IL10}{IL10_{t\infty}}\right)^{h_{it}}} + c_{it}\right),$$

$$g_{in}(x) = x\left(\frac{1-c_{in}}{1+\left(\frac{IL10}{IL10_{n\infty}}\right)^{h_{in}}} + c_{in}\right),$$

$$g_{inb}(x) = x\left(\frac{1-c_{inb}}{1+\left(\frac{IL10}{IL10_{nb\infty}}\right)^{h_{inb}}} + c_{inb}\right),$$

The diffusion functions write,

$$d_n(Z) = d_{bn}(1+d_{fn}Z), \qquad d_{pb}(P_b) = a_b P_b,$$

$$d_{mol}(Z) = d_{bmol}(1+d_{fmol}Z)\ qquad \quad d_{pt}(P) = \frac{a_t P^{2/3}}{1+b_t P^{1/3}}, d_p(Z) \quad = d_{bp}(1+d_{fp}Z).$$

The parameters used in these equations are detailed in the following tables.

PARAMETERS	VALUES
k_{pb}: Rate at which the local response in tissue B eliminate pathogen (P) in the tissue	$0.461\ B\,\text{units}^{-1}\cdot\text{hr}^{-1}$
k_{pbb}: Rate at which the local response in blood B_b eliminate pathogen (P_b) in the blood	$0.461\ B\,\text{units}^{-1}\cdot\text{hr}^{-1}$
k_{bp}: Rate at which B is exhausted by P	$0.0001\ P\,\text{units}^{-1}\cdot\text{hr}^{-1}$
k_{bbp}: Rate at which B_b is exhausted by P_b	$0.02\ P\,\text{units}^{-1}\cdot\text{hr}^{-1}$
s_b: Source of B	$0.0075\ B\,\text{units}\cdot\text{hr}^{-1}$
s_b: Source of B	$0.0075\ B\,\text{units}\cdot\text{hr}^{-1}$
s_{bb}: Source of B_b	$0.0075\ B\,\text{units}\cdot\text{hr}^{-1}$
μ_b: Decay rate for B	$0.0023\ \text{hr}^{-1}$
μ_{bb}: Decay rate for B_b	$0.0023\ \text{hr}^{-1}$
k_{pg}: Growth rate of P and P_b	$0.6\ \text{hr}^{-1}$

Table B.1: Parameters of the infection model 1/6

PARAMETERS	VALUES
P_∞: Maximum P population	20 000 P units
$P_{b\infty}$: Maximum P_b population	20 000 P units
k_{pm}: Rate at which activated macrophages (M^*) eliminate P	2.8 $P\,\text{units} \cdot \text{M}^*\,\text{units}^{-1} \cdot \text{hr}^{-1}$
k_{mp}: Rate at which pathogen activates resting macrophage (M)	40 hr^{-1}
x_{m*p}: Determines level of P needed to bring elimation of P by M^*	20 P units
x_{mp}: Determines level of P needed to bring activation of M to half their maximum	20 P units
h_{m*p}: Hill coefficient for the elimination and activation terms containing P	3
s_m: Source of M	10 $M\,\text{units} \cdot \text{hr}^{-1}$
$s_{n,b}$: Source of resting blood neutrophils (N_b)	10 $N_b\,\text{units} \cdot \text{hr}^{-1}$
μ_m: Decay rate of M	0.12 hr^{-1}
μ_{nb}: Decay rate of N_b	0.12 hr^{-1}
μ_{m*}: Decay rate of activated macrophages (M^*)	0.05 hr^{-1}
μ_{n*}: Decay rate of activated neutrophils in the tissue (N^*)	0.05 hr^{-1}
μ_{nb*}: Decay rate of activated neutrophils in the blood (N_b^*)	0.05 hr^{-1}
k_{mtcell}: Rate at which TNF activates M	20 hr^{-1}
k_{mtmol}: Rate at which TNF is consumed during the activation of M	5 $TNF\,\text{units} \cdot \text{M}\,\text{units}^{-1} \cdot \text{hr}^{-1}$
x_t: Determines level of TNF needed to bring activation of M by TNF to half its maximum	20 TNF units
h_t: Hill coefficient for the activation of M by TNF	2
k_{mrcell}: Rate at which radicals (RAD) activate M	0.01 $RAD\,\text{units}^{-1} \cdot \text{hr}^{-1}$
k_{pn}: Rate at which N^* eliminates P	5.8 $P\,\text{units} \cdot \text{N}^*\,\text{units}^{-1} \cdot \text{hr}^{-1}$

Table B.2: Parameters of the infection model 2/6

Parameters	Values
k_{pncell}: Rate at which N^* is destroyed when it eliminates P	5 hr^{-1}
r: Population of N^* that survives the elimination of P	0.98
x_{n*p}: Determines level of P needed to bring elimination of P by N^* to half its maximum	1500 P units
r: Population of N^* that survives the elimination of P	0.98
x_{n*p}: Determines level of P needed to bring elimination of P by N^* to half its maximum	1500 P units
h_{n*p}: Hill coefficient for the elimination term by N^* containing P	3
μ_t: Decay rate for TNF	1.8 hr^{-1}
μ_{tb}: Decay rate for TNF_b	1.8 hr^{-1}
k_{mat}: Rate of TNF production by M^*	3 000 TNF units·hr^{-1}
x_{m*t}: Determines level of M^* needed to bring TNF production to half its maximum	80 M^* units
h_{m*t}: Hill coefficient for the production term of TNF by M^*	2
μ_{imax}: Maximum decay rate for $IL10$	0.34 hr^{-1}
μ_{ibmax}: Maximum decay rate for $IL10_b$	0.34 hr^{-1}
μ_{imin}: Minimum decay rate for $IL10$	0.005 hr^{-1}
μ_{ibmin}: Minimum decay rate for $IL10_b$	0.005 hr^{-1}
k_{mai}: Rate of $IL10$ production by M^*	1 000 $IL10$ units·hr^{-1}
x_{m*i}: Determines level of M^* needed to bring $IL10$ production to half its maximum	140 M^* units
h_{m*i}: Hill coefficient for the production term of $IL10$ by M^*	2
x_i: Determines level of $IL10$ and $IL10_b$ needed to cause its decay rate to decrease to half its maximum	8 $IL10$ units
h_i: Hill coefficient for the production term of $IL10$	2
μ_r: Decay rate for RAD	4 hr^{-1}

Table B.3: Parameters of the infection model 3/6

PARAMETERS	VALUES
μ_{rb}: Decay rate for RAD_b	4 hr^{-1}
k_{rtr}: Rate at which RAD is produced when RAD is in the tissue	0.1hr^{-1}
k_{nar}: Rate at which RAD is released by N^*	0.01 $RAD\,\text{units}\cdot\text{hr}^{-1}\cdot\text{N}^*\,\text{units}^{-1}$
k_{narb}: Rate at which RAD_b is released by N_b^*	0.01 $RAD\,\text{units}\cdot\text{hr}^{-1}\cdot\text{N}^*\,\text{units}^{-1}$
k_{natr}: Rate at which RAD is produced when N^* is in the tissue causing damage	0.01 $RAD\,\text{units}\cdot\text{hr}^{-1}\cdot\text{N}^*\,\text{units}^{-1}$
k_{rtmp}: Rate at which RAD is produced when M^* eliminates P in the tissue	1×10^{-5} hr^{-1}
k_{tg}: Repair rate of the tissue integrity	2 hr^{-1}
T_∞: TI maximum	1
a: Below $TI = a$, tissue is inable to repair itself	0.1
k_{rtt}: Rate at which RAD deplete TI	0.01 $RAD\,\text{units}^{-1}\cdot\text{hr}^{-1}$
k_{tz}: Rate at which TNF and tissue damage cause inflammation (Z)	0.5 hr^{-1}
x_{tz}: Determines level of TNF needed to bring production of Z by TNF to half its maximum	20 TNF-units
h_{tz}: Hill coefficient for the production term of Z by TNF	2
k_{zti}: Relative effectiveness of TNF versus tissue damage in producing Z	0.1
μ_z: Decay rate of Z	0.01 hr^{-1}
k_{pnb}: Rate at which N_b^* eliminates P_b	0.04 $P\,\text{units}\cdot\text{N}^*\,\text{units}^{-1}\cdot\text{hr}^{-1}$
$k_{pnbcell}$: Rate at which N_b^* is destroyed when it eliminates P_b	5 hr^{-1}
r_b: Population of N_b^* that survives the elimination of P_b	0.98
x_{n*pb}: Determines level of P_b needed to bring activation of N_b and P elimination by N_b^* to half their maximum	0.1 P units

Table B.4: Parameters of the infection model 4/6

PARAMETERS	VALUES
h_{n*pb}: Hill coefficient for P_b elimination by N_b^*	1
k_{ntcell} : Rate at which TNF_b activates N_b	2 hr^{-1}
k_{ntmol}: Rate at which TNF_b is consumed during the activation of N_b	0.8 $TNF\,\mathrm{units}\cdot\mathrm{N\,units}^{-1}\cdot\mathrm{hr}^{-1}$
x_{tb}: Determines level of TNF_b needed to bring activation of N_b by TNF_b to half its maximum	2 TNF units
h_{tb}: Hill coefficient for the activation of N_b by TNF_b	2
k_{nrb}: Rate at which RAD activate N_b	0.1 $RAD\,\mathrm{units}^{-1}\cdot\mathrm{hr}^{-1}$
k_{snb}: Rate at which the source of N_b increases	3 $N\,\mathrm{units}\cdot\mathrm{hr}^{-1}$
c: Effectiveness of N^* at increasing the source of N_b (s_{nb})	1
d: Effectiveness of N_b^* at increasing the source of N_b	1
x_{snb}: Determines level of N^* and N_b^* needed to bring increase in s_{nb} to half their maximum	200 N^* units
h_{snb}: Hill coefficient for the increase of s_{nb}	2
c_i: Maximum inhibition level of g_i, inhibition of macrophage functions	0.05
c_{it}: Maximum inhibition level of g_{it}, inhibition of TNF production	1×10^{-6}
c_{in}: Maximum inhibition level of g_{in}, inhibition of neutrophils in the tissue	0.15
c_{inb}: Maximum inhibition level of g_{inb}, inhibition of blood neutrophils	0.15
h_i: Hill coefficient for g_i	3
h_{it}: Hill coefficient for g_{it}	5
h_{in}: Hill coefficient for g_{in}	1
h_{inb}: Hill coefficient for g_{inb}	1
$IL10_\infty$: Determines level of $IL10$ needed to bring macrophage inhibition to half its maximum	200 $IL10$ units
$IL10_{t\infty}$: Determines level of $IL10$ needed to bring the inhibition of TNF production	60 $IL10$ units

Table B.5: Parameters of the infection model 5/6

PARAMETERS	VALUES
$IL10_{n\infty}$: Determines level of $IL10$ needed to bring tissue neutrophils inhibition to half its maximum	80 $IL10$ units
$IL10_{nb\infty}$: Determines level of $IL10_b$ needed to bring blood neutrophils inhibition to half its maximum	80 $IL10_b$ units
d_{bn}: Baseline diffusion of neutrophils	0.005 $\mathrm{L}\cdot\mathrm{hr}^{-1}$
d_{fn}: Effectiveness of Z in increasing neutrophil diffusion	50
d_{bp}: Baseline diffusion of pathogen	1
d_{fp}: Effectiveness of Z in increasing pathogen diffusion	1
d_{bmol}: Baseline diffusion of molecules	10 $\mathrm{L}\cdot\mathrm{hr}^{-1}$
d_{fmol}: Effectiveness of Z in increasing molecule diffusion	1
a_t: Constant in the numerator of d_{pt}	50
b_t: Constant in the denominator of d_{pt}	0.8 $(P \text{ units})^{-1/3}$
a_b: Rate of pathogen diffusion in d_{pb}	2000 hr^{-1}
k_{rntp}: Rate at which RAD is produced when N^* eliminates P in the tissue	0.2 $RAD\,\text{units} \cdot \mathrm{M}^*\,\text{units}^{-1} \cdot$ $P\,\text{units}^{-1} \cdot \mathrm{hr}^{-1}$

Table B.6: Parameters of the infection model 6/6

Bibliography

[1] Robert A. Adams and John J.F. Fournier. *Sobolev Spaces.* Academic Press Second Edition, 2003.

[2] Valentina Agostini, Emma Chiaramello, Carla Bredariol, Chanda Cavallini, and Marco Knaflitz. Postural control after traumatic brain injury in patients with neuro-ophthalmic deficits. *Gait & Posture*, 34(2):248–253, June 2011.

[3] Emilio Agostoni. Mechanics of the pleural space. *Comprehensive Physiology*, 1972.

[4] Eric W. F. W. Alton, Alison Baker, Eilidh Baker, et al. The safety profile of a cationic lipid-mediated cystic fibrosis gene transfer agent following repeated monthly aerosol administration to sheep. *Biomaterials*, 34(38):10267–10277, December 2013.

[5] J. D. Altringham and I. S. Young. Power output and the frequency of oscillatory work in mammalian diaphragm muscle: the effects of animal size. *Journal of Experimental Biology*, 157:381–389, May 1991.

[6] B. Asgharian, W. Hofmann, and R. Bergmann. Particle deposition in a multiple-path model of the human lung. *Aerosol Sci. Tech.*, 34(4):332–339, 2001.

[7] C. Baranger, L. Boudin, P.-E. Jabin, and S. Mancini. A modeling of biospray for the upper airways. In *CEMRACS 2004—mathematics and applications to biology and medicine*, volume 14 of *ESAIM Proc.*, pages 41–47. EDP Sci., Les Ulis, 2005.

[8] Cynthia M. Beall. Andean, Tibetan, and Ethiopian patterns of adaptation to high-altitude hypoxia. *Integr Comp Biol*, 46(1):18–24, February 2006.

[9] Alona Ben-Tal and Merryn H. Tawhai. Integrative approaches for modeling regulation and function of the respiratory system. *WIREs Syst Biol Med*, 5(6):687–699, November 2013.

[10] Lorenz Berger, Rafel Bordas, Kelly Burrowes, Vicente Grau, Simon Tavener, and David Kay. A poroelastic model coupled to a fluid network with applications in lung modelling. *Int. J. Numer. Meth. Biomed. Engng.*, 32(1):n/a–n/a, January 2016.

[11] Jeff Bezanson, Alan Edelman, Viral Shah, and Stefan Karpinski. The Julia Program Language. `https://julialang.org`, 2012.

[12] Charles M. Bishop. The maximum oxygen consumption and aerobic scope of birds and mammals: getting to the heart of the matter. *Proceedings of the Royal Society of London B: Biological Sciences*, 266(1435):2275–2281, November 1999.

[13] Stephen P Blackie, Mary Sue Fairbarn, Noel G. McElvaney, Pearce G. Wilcox, Nancy J Morrison, and Richard L. Pardy. Normal Values and Ranges for Ventilation and Breathing Pattern at Maximal Exercise. *Chest*, 100(1):136–142, July 1991.

[14] Michela Botta et al. Ventilation management and clinical outcomes in invasively ventilated patients with COVID-19 (PRoVENT-COVID): a national, multicentre, observational cohort study. *The Lancet Respiratory Medicine*, 0(0), October 2020. Publisher: Elsevier.

[15] Laurent Boudin, Céline Grandmont, Alexander Lorz, and Ayman Moussa. Modelling and numerics for respiratory aerosols. *Commun. Comput. Phys.*, 18(3):723–756, 2015.

[16] Laurent Boudin, Céline Grandmont, Bérénice Grec, and Driss Yakoubi. Influence of the spray retroaction on the airflow. In *CEMRACS 2009 – Mathematical Modelling in Medicine*, volume 30 of *ESAIM Proc.*, pages 153–165. EDP Sci., Les Ulis, 2010.

[17] Alexandra Buess, Alain Van Muylem, Antoine Nonclercq, and Benoit Haut. Modeling of the transport and exchange of a gas species in lungs with an asymmetric branching pattern. application to nitric oxide. *Frontiers in Physiology*, 11:1473, 2020.

[18] Lester Caudill and Fiona Lynch. A Mathematical Model of the Inflammatory Response to Pathogen Challenge. *Bulletin of Mathematical Biology*, 80(8):2242–2271, 2018.

[19] Limei Cheng, Olga Ivanova, Hsing-Hua Fan, and Michael C. K. Khoo. An integrative model of respiratory and cardiovascular control in sleep-disordered breathing. *Respiratory Physiology & Neurobiology*, 174(1):4–28, November 2010.

[20] Fabrizio Clarelli and Roberto Natalini. A pressure model of immune response to mycobacterium tuberculosis infection in several space dimensions. *Mathematical biosciences and engineering: MBE*, 7(2):277–300, April 2010.

[21] Raphaël Clément and Benjamin Mauroy. An archetypal mechanism for branching organogenesis. *Phys. Biol.*, 11(1):016003, February 2014.

[22] A. Comerford, G. Bauer, and W. A. Wall. Nanoparticle transport in a realistic model of the tracheobronchial region. *Int. J. Numer. Method Biomed. Eng.*, 26(7):904–914, 2010.

[23] M. L. Crosfill and J. G. Widdicombe. Physical characteristics of the chest and lungs and the work of breathing in different mammalian species. *The Journal of Physiology*, 158(1):1–14, September 1961.

[24] Charles P. Davis. *Hemoglobin Ranges: Normal, Symptoms of High and Low Levels*. 2017.

[25] Judy Day, Avner Friedman, and Larry S. Schlesinger. Modeling the immune rheostat of macrophages in the lung in response to infection. *Proceedings of the National Academy of Sciences*, 106(27):11246–11251, July 2009. Publisher: National Academy of Sciences Section: Biological Sciences.

[26] Jerome A. Dempsey and Anthony J. Jacques. Respiratory System Response to Exercise in Health. In Michael A. Grippi, Jack A. Elias, Jay A. Fishman, Robert M. Kotloff, Allan I. Pack, Robert M. Senior, and Mark D. Siegel, editors, *Fishman's Pulmonary Diseases and Disorders*. McGraw-Hill Education, New York, NY, 5 edition, 2015.

[27] D. S. Dhindsa, A. S. Hoversland, and J. Metcalfe. Comparative studies of the respiratory functions of mammalian blood. VII. Armadillo (Dasypus novemcinctus). *Respiration Physiology*, 13(2):198–208, November 1971.

[28] Jérôme Droniou. Solving convection-diffusion equations with mixed, Neumann and Fourier boundary conditions and measures as data, by a duality method. *Advances in Differential Equations*, 5(10-12):1341–1396, 2000. Publisher: Khayyam Publishing, Inc.

[29] Xavier Dubois de La Sablonière, Benjamin Mauroy, and Yannick Privat. Shape minimization of the dissipated energy in dyadic trees. *Discrete and Continuous Dynamical Systems - Series B*, 16(3):767–799, June 2011.

[30] David Elad, Roger D. Kamm, and Ascher H. Shapiro. Steady compressible flow in collapsible tubes: application to forced expiration. *Journal of Fluid Mechanics*, 203:401–418, June 1989.

[31] A. M. Elaiw, A. Alhejelan, and M. A. Alghamdi. Global Dynamics of Virus Infection Model with Antibody Immune Response and Distributed Delays. *Discrete Dynamics in Nature and Society*, 2013:1–9, 2013. Publisher: Hindawi.

[32] John V. Fahy and Burton F. Dickey. Airway mucus function and dysfunction. *The New England Journal of Medicine*, 363:2233–2247, December 2010.

[33] Joseph Feher. *Quantitative Human Physiology*. Elsevier, second edition edition, 2016.

[34] Maddalena Felici. *Physics of the oxygen diffusion in the human lung*. PhD thesis, Ecole Polytechnique X, June 2003.

[35] F. Filbet and E. Sonnendrücker. Numerical methods for the Vlasov equation. In *Numerical mathematics and advanced applications*, pages 459–468. Springer Italia, Milan, 2003.

[36] M. Florens, B. Sapoval, and M. Filoche. An anatomical and functional model of the human tracheobronchial tree. *Journal of Applied Physiology*, 110(3):756–763, March 2011.

[37] Magali Florens, Bernard Sapoval, and Marcel Filoche. Optimal Branching Asymmetry of Hydrodynamic Pulsatile Trees. *Phys. Rev. Lett.*, 106(17):178104, April 2011.

[38] D. Gammack, C. R. Doering, and D. E. Kirschner. Macrophage response to Mycobacterium tuberculosis infection. *Journal of Mathematical Biology*, 48(2):218–242, February 2004.

[39] Ajay Gautam, Charles L. Densmore, Eva Golunski, Bo Xu, and J. Clifford Waldrep. Transgene Expression in Mouse Airway Epithelium by Aerosol Gene Therapy with PEI–DNA Complexes. *Molecular Therapy*, 3(4):551–556, April 2001.

[40] T. Gemci, T. E. Corcoran, and N. Chigier. A numerical and experimental study of spray dynamics in a simple throat model. *Aerosol Sci. Technol.*, 36:18–38, 2002.

[41] Julia H. Goedecke, Alan St Clair Gibson, Liesl Grobler, Malcolm Collins, Timothy D. Noakes, and Estelle V. Lambert. Determinants of the variability in respiratory exchange ratio at rest and during exercise in trained athletes. *American Journal of Physiology-Endocrinology and Metabolism*, 279(6):E1325–E1334, December 2000.

[42] F S Grodins, J Buell, and A J Bart. Mathematical analysis and digital simulation of the respiratory control system. *Journal of Applied Physiology*, 22(2):260–276, February 1967.

[43] B. Gunther. Dimensional analysis and theory of biological similarity. *Physiological Reviews*, 55(4):659–699, October 1975.

[44] B. Günther and B. L. De la Barra. Physiometry of the mammalian circulatory system. *Acta Physiologica Latino Americana*, 16(1):32–42, 1966.

[45] Beatrice Haefeli-Bleuer and Ewald R. Weibel. Morphometry of the human pulmonary acinus. *Anat. Rec.*, 220(4):401–414, April 1988.

[46] Wenrui Hao, Elliott D. Crouser, and Avner Friedman. Mathematical model of sarcoidosis. *Proceedings of the National Academy of Sciences of the United States of America*, 111(45):16065–16070, November 2014.

[47] Hans C Haverkamp, Jerome A Dempsey, Jordan D Miller, Lee M Romer, and Marlowe W Eldridge. Physiologic responses to exercise. In *Physiologic basis of respiratory disease*, page 17. BC Decker, Inc, Hamilton, 2005.

[48] F. Hecht. New development in FreeFem++. *J. Numer. Math.*, 20(3-4):251–265, 2012.

[49] Chris Higgins. *Parameters that reflect the carbon dioxide content of blood.* 2008.

[50] Robert Hill, H. P. Wolvekamp, and Frederick Gowland Hopkins. The oxygen dissociation curve of haemoglobin in dilute solution. *Proc. R. Soc. Lond. B*, 120(819):484–495, 1936.

[51] Connie C.W. Hsia, Dallas M. Hyde, and Ewald R. Weibel. Lung Structure and the Intrinsic Challenges of Gas Exchange. In Ronald Terjung, editor, *Comprehensive Physiology*, pages 827–895. John Wiley & Sons, Inc., Hoboken, NJ, USA, March 2016.

[52] Lawrence N. Hudson, Nick J. B. Isaac, and Daniel C. Reuman. The relationship between body mass and field metabolic rate among individual birds and mammals. *Journal of Animal Ecology*, 82(5):1009–1020, 2013. _eprint: https://besjournals.onlinelibrary.wiley.com/doi/pdf/10.1111/1365-2656.12086.

[53] J. S. Huxley and G. Teissier. Terminology of Relative Growth. *Nature*, 137(3471):780–781, May 1936.

[54] M. Jetté, K. Sidney, and G. Blümchen. Metabolic equivalents (METS) in exercise testing, exercise prescription, and evaluation of functional capacity. *Clinical Cardiology*, 13(8):555–565, August 1990.

[55] Arthur T. Johnson. *Biomechanics and Exercise Physiology: Quantitative Modeling.* CRC Press, March 2007. Google-Books-ID: oIvMBQAAQBAJ.

[56] Cyril Karamaoun, Benjamin Sobac, Benjamin Mauroy, Alain Van Muylem, and Benoît Haut. New insights into the mechanisms controlling the bronchial mucus balance. *PLOS ONE*, 13(6):e0199319, 2018.

[57] Hiroko Kitaoka, Ryuji Takaki, and Béla Suki. A three-dimensional model of the human airway tree. *Journal of Applied Physiology*, 87(6):2207–2217, December 1999.

[58] M. Kleiber. Body size and metabolism. *Hilgardia*, 6(11):315–353, January 1932.

[59] Vladimir Koulich, Jose' L. Lage, Connie C. W. Hsia, and Jr Robert L. Johnson. A Porous Medium Model of Alveolar Gas Diffusion. *JPM*, 2(3), 1999.

[60] Fujio Kuwahara, Yoshihiko Sano, Jianjun Liu, and Akira Nakayama. A porous media approach for bifurcating flow and mass transfer in a human lung. *Journal of Heat Transfer*, 131(10):101013, 2009.

[61] Liyang Li, Qihong Huang, Diane C. Wang, David H. Ingbar, and Xiangdong Wang. Acute lung injury in patients with COVID-19 infection. *Clinical and Translational Medicine*, 10(1):20–27, January 2020.

[62] Tom Linder and Anna E. Melby. *Amount of Oxygen in the Blood.*

[63] J.L. Lions and E. Magenes. *Problèmes aux limites non homogènes et applications.* Dunod Paris, 1968.

[64] P. W. Longest and M. Hindle. CFD simulations of enhanced condensational growth (ECG) applied to respiratory drug delivery with comparisons to in vitro data. *J. Aerosol Sci.*, 41(8):805–820, 2010.

[65] P. W. Longest and M. Hindle. Numerical model to characterize the size increase of combination drug and hygroscopic excipient nanoparticle aerosols. *Aerosol Sci. Technol.*, 45(7):884–899, 2011.

[66] P. W. Longest and C. Kleinstreuer. Computational models for simulating multicomponent aerosol evaporation in the upper respiratory airways. *Aerosol Sci. Tech.*, 39(2):124–138, 2005.

[67] Wanjun Lu, Huirong Guo, I. M. Chou, R. C. Burruss, and Lanlan Li. Determination of diffusion coefficients of carbon dioxide in water between 268 and 473k in a high-pressure capillary optical cell with in situ Raman spectroscopic measurements. *Geochimica et Cosmochimica Acta*, 115:183–204, August 2013.

[68] E. N. Marieb and K. N. Hoehn. *Human anatomy and physiology.* Pearson, 11 edition, 2018.

[69] Sébastien Martin and Bertrand Maury. Modeling of the oxygen transfer in the respiratory process. *ESAIM: Mathematical Modelling and Numerical Analysis*, 47(4):935–960, July 2013.

[70] B. Mauroy, M. Filoche, E. R. Weibel, and B. Sapoval. An optimal bronchial tree may be dangerous. *Nature*, 427(6975):633–636, February 2004.

[71] Benjamin Mauroy. *Hydrodynamique dans le poumon, relations entre flux et géométries.* PhD thesis, ENS de Cachan, ENS de Cachan, July 2004.

[72] Benjamin Mauroy. *Viscosity : an architect for the respiratory system?* Habilitation à diriger des recherches, Université de Nice-Sophia Antipolis, December 2014.

[73] Benjamin Mauroy and Plamen Bokov. The influence of variability on the optimal shape of an airway tree branching asymmetrically. *Phys Biol*, 7(1):16007, 2010.

[74] H. Mayer, K. S. Zaenker, and U. An Der Heiden. A basic mathematical model of the immune response. *Chaos (Woodbury, N.Y.)*, 5(1):155–161, March 1995.

[75] Jere Mead. Control of respiratory frequency. *Journal of Applied Physiology*, 15(3):325–336, May 1960.

[76] D. Michel. *Analyse mathématique de couplages fluide-cinétique.* PhD thesis, Sorbonne Université, work in progress since 2018.

[77] Akiko Murase, Toru Sasaki, and Tsuyoshi Kajiwara. Stability analysis of pathogen-immune interaction dynamics. *Journal of Mathematical Biology*, 51(3):247–267, September 2005.

[78] J. F. Murray and J. A. Nadel. *Textbook of respiratory medecine.* Elsevier, 6 edition, 2016.

[79] K. A. Nagy. Field metabolic rate and body size. *Journal of Experimental Biology*, 208(9):1621–1625, May 2005.

[80] Jessica M. Oakes, Alison L. Marsden, Céline Grandmont, Shawn C. Shadden, Chantal Darquenne, and Irène E. Vignon-Clémentel. Airflow and particle deposition simulations in health and emphysema: From in vivo to in silico animal experiments. *Ann. Biomed. Eng.*, 42(4):899–914, 2014.

[81] Matthias Ochs, Jens R. Nyengaard, Anja Jung, Lars Knudsen, Marion Voigt, Thorsten Wahlers, Joachim Richter, and Hans Jørgen G. Gundersen. The Number of Alveoli in the Human Lung. *Am J Respir Crit Care Med*, 169(1):120–124, January 2004.

[82] Arthur B. Otis, Wallace O. Fenn, and Hermann Rahn. Mechanics of Breathing in Man. *Journal of Applied Physiology*, 2(11):592–607, May 1950.

[83] A. L. Patra. Comparative anatomy of mammalian respiratory tracts: the nasopharyngeal region and the tracheobronchial region. *Journal of Toxicology and Environmental Health*, 17(2-3):163–174, 1986.

[84] Andrew J Peacock. Oxygen at high altitude. *BMJ*, 317(7165):1063–1066, October 1998.

[85] Alan S. Perelson. Modelling viral and immune system dynamics. *Nature Reviews. Immunology*, 2(1):28–36, January 2002.

[86] Robert H. Peters. *The ecological implications of body size*, volume 2. Cambridge University Press, 1986.

[87] C. Rabec, J. Gonzalez-Bermejo, Respiratory Support Chronic Care Group AVO2 of the French Society of Respiratory Diseases SPLF, and GAVO2 collaborators. Respiratory support in patients with COVID-19 (outside intensive care unit). A position paper of the Respiratory Support and Chronic Care Group of the French Society of Respiratory Diseases. *Respiratory Medicine and Research*, 78:100768, November 2020.

[88] Bastian E. Rapp. *Microfluidics: Modelling, Mechanics and Mathematics.* Elsevier, 2017.

[89] Angela Reynolds, G. Bard Ermentrout, and Gilles Clermont. A mathematical model of pulmonary gas exchange under inflammatory stress. *Journal of Theoretical Biology*, 264(2):161–173, May 2010.

[90] Angela Reynolds, Jonathan Rubin, Gilles Clermont, Judy Day, Yoram Vodovotz, and G. Bard Ermentrout. A reduced mathematical model of the acute inflammatory response: I. Derivation of model and analysis of anti-inflammation. *Journal of Theoretical Biology*, 242(1):220–236, September 2006.

[91] Angela Marie Reynolds. *Mathematical Models of Acute Inflammation and a Full Lung Model of Gas Exchange Under Inflammatory Stress.* phdthesis, University of Pittsburg, 2008.

[92] Hannah Ritchie, Esteban Ortiz-Ospina, Diana Beltekian, Edouard Mathieu, Joe Hasell, Bobbie Macdonald, Charlie Giattino, and Max Roser. Coronavirus (COVID-19) cases. `https://ourworldindata.org/covid-cases`, 2020.

[93] M. Rodriguez, S. Bur, A. Favre, and E. R. Weibel. Pulmonary acinus: Geometry and morphometry of the peripheral airway system in rat and rabbit. *American Journal of Anatomy*, 180(2):143–155, 1987.

[94] R. Sander. Compilation of Henry's law constants (version 4.0) for water as solvent. *Atmospheric Chemistry and Physics*, 15(8):4399–4981, April 2015.

[95] Bernard Sapoval, M. Filoche, and E. R. Weibel. Smaller is better—but not too small: A physical scale for the design of the mammalian pulmonary acinus. *PNAS*, 99(16):10411–10416, August 2002.

[96] Bernard Sapoval and Marcel Filoche. Role of diffusion screening in pulmonary diseases. *Adv. Exp. Med. Biol.*, 605:173–178, 2008.

[97] Kenneth B. Saunders, Hari N. Bali, and Ewert R. Carson. A breathing model of the respiratory system: The controlled system. *Journal of Theoretical Biology*, 84(1):135–161, May 1980.

[98] Knut Schmidt-Nielsen. *Scaling: Why is Animal Size so Important?* Cambridge University Press, 1984.

[99] Michael W. Sims. Aerosol Therapy for Obstructive Lung Diseases. *Chest*, 140(3):781–788, September 2011.

[100] T.T. Soong, P. Nicolaides, C. P. Yu, and S. C. Soong. A statistical description of the human tracheobronchial tree geometry. *Resp. Physiol.*, 37:161–172, 1979.

[101] Walter R. Stahl. Scaling of respiratory variables in mammals. *J. appl. Physiol*, 22(3):453–460, 1967.

[102] Susan Standring. *Gray's Anatomy. The Anatomical Basis of Clinical Practice.* Elsevier Churchill Livingston, 2005.

[103] J. F. Storz, G. R. Scott, and Z. A. Cheviron. Phenotypic plasticity and genetic adaptation to high-altitude hypoxia in vertebrates. *Journal of Experimental Biology*, 213(24):4125–4136, December 2010.

[104] X. G. Sun, J. E. Hansen, W. W. Stringer, H. Ting, and K. Wasserman. Carbon dioxide pressure-concentration relationship in arterial and mixed venous blood during exercise. *Journal of Applied Physiology (Bethesda, Md.: 1985)*, 90(5):1798–1810, May 2001.

[105] Merryn H. Tawhai, Peter Hunter, Juerg Tschirren, Joseph Reinhardt, Geoffrey McLennan, and Eric A. Hoffman. CT-based geometry analysis and finite element models of the human and ovine bronchial tree. *J. Appl. Physiol.*, 97(6):2310–2321, December 2004.

[106] S. M. Tenney and D. Bartlett. Comparative quantitative morphology of the mammalian lung: Trachea. *Respiration Physiology*, 3(2):130–135, October 1967.

[107] S. M. Tenney and J. B. Tenney. Quantitative morphology of cold-blooded lungs: Amphibia and reptilia. *Respiration Physiology*, 9(2):197–215, May 1970.

[108] Luc J. Teppema and Albert Dahan. The Ventilatory Response to Hypoxia in Mammals: Mechanisms, Measurement, and Analysis. *Physiological Reviews*, 90(2):675–754, April 2010.

[109] Ching-Li Tseng, Steven Yueh-Hsiu Wu, Wen-Hsi Wang, Cheng-Liang Peng, et al. Targeting efficiency and biodistribution of biotinylated-EGF-conjugated gelatin nanoparticles administered via aerosol delivery in nude mice with lung cancer. *Biomaterials*, 29(20):3014–3022, July 2008.

[110] Thirumalaisamy P. Velavan and Christian G. Meyer. The COVID-19 epidemic. *Tropical Medicine & International Health*, 25(3):278–280, March 2020.

[111] J. B. Warren, S. J. Jennings, and T. J. Clark. Effect of adrenergic and vagal blockade on the normal human airway response to exercise. *Clinical Science (London, England: 1979)*, 66(1):79–85, January 1984.

[112] E. R. Weibel. *Morphometry of the human lung.* Springer Verlag and Academic Press, New York, 1963.

[113] Ewald R. Weibel. *The Pathway for Oxygen: Structure and Function in the Mammalian Respiratory System.* Harvard University Press, 1984.

[114] Ewald R. Weibel, Leonardo D. Bacigalupe, Beat Schmitt, and Hans Hoppeler. Allometric scaling of maximal metabolic rate in mammals: muscle aerobic capacity as determinant factor. *Respiratory Physiology & Neurobiology*, 140(2):115–132, May 2004.

[115] Ewald R. Weibel, Andre F. Cournand, and Dickinson W. Richards. *Morphometry of the Human Lung.* Springer, 1 edition edition, January 1963.

[116] Ewald R. Weibel and Hans Hoppeler. Exercise-induced maximal metabolic rate scales with muscle aerobic capacity. *Journal of Experimental Biology*, 208(9):1635–1644, May 2005.

[117] Geoffrey B. West, James H. Brown, and Brian J. Enquist. A general model for the origin of allometric scaling laws in biology. *Science*, 276(5309):122–126, 1997.

[118] John B. West. The Physiologic Basis of High-Altitude Diseases. *Annals of Internal Medicine*, 141(10):789, November 2004.

[119] John B. West. *Respiratory Physiology: The Essentials.* Lippincott Williams and Wilkins, Philadelphia, 9th revised edition edition, August 2011.

[120] Dominik Wodarz. Mathematical models of immune effector responses to viral infections: Virus control versus the development of pathology. *Journal of Computational and Applied Mathematics*, 184(1):301–319, December 2005.

[121] J. Worthington, I. S. Young, and J. D. Altringham. The relationship between body mass and ventilation rate in mammals. *The Journal of Experimental Biology*, 161:533–536, November 1991.

[122] I. S. Young, R. D. Warren, and J. D. Altringham. Some properties of the mammalian locomotory and respiratory systems in relation to body mass. *Journal of Experimental Biology*, 164(1):283–294, March 1992.

[123] Zhe Zhang, Clement Kleinstreuer, and Chong S. Kim. Airflow and nanoparticle deposition in a 16-generation tracheobronchial airway model. *Ann. Biomed. Eng.*, 36(12):2095–2110, 2008.